Methods for Melting Temperature Calculation

Thesis by

Qi-Jun Hong

In Partial Fulfillment of the Requirements

for the Degree of

Doctor of Philosophy

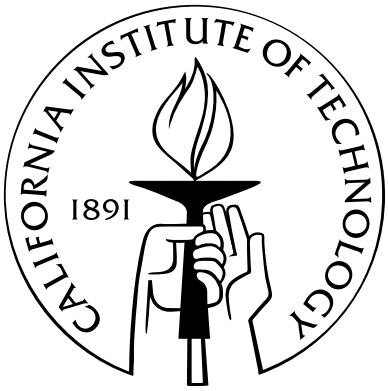

California Institute of Technology

Pasadena, California

2015

(Defended October 28, 2014)

To my parents

Acknowledgments

None of this work would have been possible without the help of many people. I would like to thank:

- my advisor, Axel van de Walle, who helped me throughout the last five years and gave me the freedom to choose research topics, and taught me how to write good papers.

- my committee members, Bill Goddard, Tom Miller, and Nate Lewis, for your constructive comments and discussions on my research, proposals, and thesis.

- my labmates, Ljuba Miljacic, Pratyush Tiwary, Ligen Wang, Sara Kadkhodaei, Steve Demers, Greg Pomrehn, Balaji Gopal Chirranjeevi, Ruoshi Sun, and Joe Yasi. It has been a pleasure knowing you, working with you, and learning things from you.

- computer resources: Eniac, Lonestar, Ranger, Trestles, Stampede, and the Center for Computation and Visualization at Brown University.

- my parents, for your full support for me studying abroad, and your unconditional love. I know you will always be on my side.

- my close friends at Caltech, Bin Zhang, Na Hu, Haoxuan Wang, and Fan Liu, for the joyful time we spent together.

- my girlfriend, Jingwen Qu, for your support, encouragement, and love.

Abstract

Melting temperature calculation has important applications in the theoretical study of phase diagrams and computational materials screenings. In this thesis, we present two new methods, i.e., the improved Widom's particle insertion method and the small-cell coexistence method, which we developed in order to capture melting temperatures both accurately and quickly.

We propose a scheme that drastically improves the efficiency of Widom's particle insertion method by efficiently sampling cavities while calculating the integrals providing the chemical potentials of a physical system. This idea enables us to calculate chemical potentials of liquids directly from first-principles without the help of any reference system, which is necessary in the commonly used thermodynamic integration method. As an example, we apply our scheme, combined with the density functional formalism, to the calculation of the chemical potential of liquid copper. The calculated chemical potential is further used to locate the melting temperature. The calculated results closely agree with experiments.

We propose the small-cell coexistence method based on the statistical analysis of small-size coexistence MD simulations. It eliminates the risk of a metastable superheated solid in the fast-heating method, while also significantly reducing the computer cost relative to the traditional large-scale coexistence method. Using empirical potentials, we validate the method and systematically study the finite-size effect on the calculated melting points. The method converges to the exact result in the limit of a large system size. An accuracy within 100 K in melting temperature is usually achieved when the simulation contains more than 100 atoms. DFT examples of Tantalum, high-pressure Sodium, and ionic material NaCl are shown to demonstrate

the accuracy and flexibility of the method in its practical applications. The method serves as a promising approach for large-scale automated material screening in which the melting temperature is a design criterion.

We present in detail two examples of refractory materials. First, we demonstrate how key material properties that provide guidance in the design of refractory materials can be accurately determined via *ab initio* thermodynamic calculations in conjunction with experimental techniques based on synchrotron X-ray diffraction and thermal analysis under laser-heated aerodynamic levitation. The properties considered include melting point, heat of fusion, heat capacity, thermal expansion coefficients, thermal stability, and sublattice disordering, as illustrated in a motivating example of lanthanum zirconate ($La_2Zr_2O_7$). The close agreement with experiment in the known but structurally complex compound $La_2Zr_2O_7$ provides good indication that the computation methods described can be used within a computational screening framework to identify novel refractory materials. Second, we report an extensive investigation into the melting temperatures of the Hf-C and Hf-Ta-C systems using *ab initio* calculations. With melting points above 4000 K, hafnium carbide (HfC) and tantalum carbide (TaC) are among the most refractory binary compounds known to date. Their mixture, with a general formula $Ta_xHf_{1-x}C_y$, is known to have a melting point of 4215 K at the composition Ta_4HfC_5, which has long been considered as the highest melting temperature for any solid. Very few measurements of melting point in tantalum and hafnium carbides have been documented, because of the obvious experimental difficulties at extreme temperatures. The investigation lets us identify three major chemical factors that contribute to the high melting temperatures. Based on these three factors, we propose and explore a new class of materials, which, according to our *ab initio* calculations, may possess even higher melting temperatures than Ta-Hf-C. This example also demonstrates the feasibility of materials screening and discovery via *ab initio* calculations for the optimization of "higher-level" properties whose determination requires extensive sampling of atomic configuration space.

Contents

List of Figures

List of Tables

Chapter 1

Introduction

Theoretical predictions of melting temperature have a long history [1], and have been based on a wide variety of computational approaches, as well as different levels of accuracy in the descriptions of interatomic interactions. In the last two decades, thanks to the increased availability of computing power, density functional theory (DFT) [2, 3, 4] has established itself as a useful simulation tool for accurate and general modeling of materials. However, melting point predictions based on DFT are still considered challenging because of the requirement for large simulation cells, long simulation trajectories, and/or the dependence on auxiliary empirical potentials. In this chapter, we first review a number of commonly used methods. Through comparison, we summarize several key favorable features that an ideal method should contain. These discussions lead us to develop two methods, i.e., the Widom's test-particle insertion method and the small-cell coexistence method, which are extensively studied in this thesis.

1.1 A review of current methods

Over the past decades, numerous ingenious methods have been devised to capture melting temperatures from DFT. Some of them are inspired by the natural process of melting: the melting temperature is approached by the evolution of the solid and/or the liquid involved in the phase transition. The atomic movements are simulated through techniques such as molecular dynamics (MD) and Monte Carlo (MC). Some

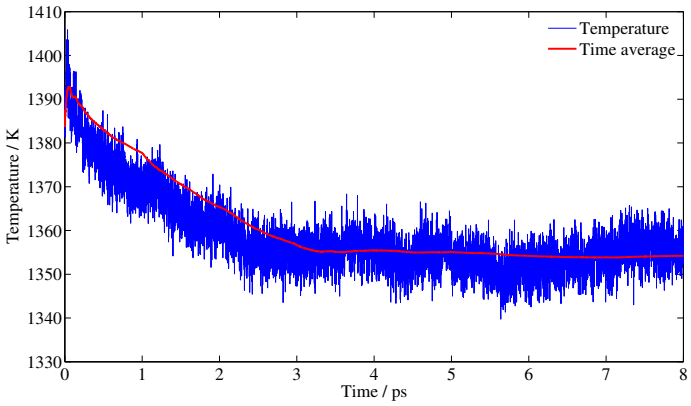

Figure 1.1: Traditional large-size coexistence method. This figure shows the temperature evolution over time. After 3 picoseconds, the system reaches equilibrium, and thus the stabilized temperature is the melting point. Here a Cu embedded atom model (EAM) potential (Mendelev, 2008) [5] is employed on a $40 \times 20 \times 20$ face-center cubic (fcc) supercell, with 64,000 atoms.

locate melting temperatures based on thermodynamic properties, e.g., the free energies of the solid and the liquid. Here we review some of the most commonly used methods to date.

Large-size coexistence method

In the traditional large-size coexistence method [6, 7, 8, 9, 10], people search for stabilized solid-liquid coexistence, whose temperature is naturally the melting point. The simulations are usually carried out in a NVE (or NPH) ensemble, i.e., constant number of atoms N, constant volume V, and constant internal energy E. To understand how this technique helps the system evolve toward equilibrium, consider a coexisting system with a phase boundary. If the system as a whole is at a temperature slightly *below* the melting point, then some portion of the liquid phase will *solidify*, *generating* the appropriate latent heat. Because the system is closed (NVE), this *heats up* the system towards the melting point. Similarly, if the system is above the melting temperature, the latent heat required to melt the solid will cool the system down. There is no difficulty in nucleating either the liquid or solid phases, as the interface assists the nucleation for the melting or solidification process. In the NVE ensemble, for each chosen volume V there is a whole range of energies E for which solid

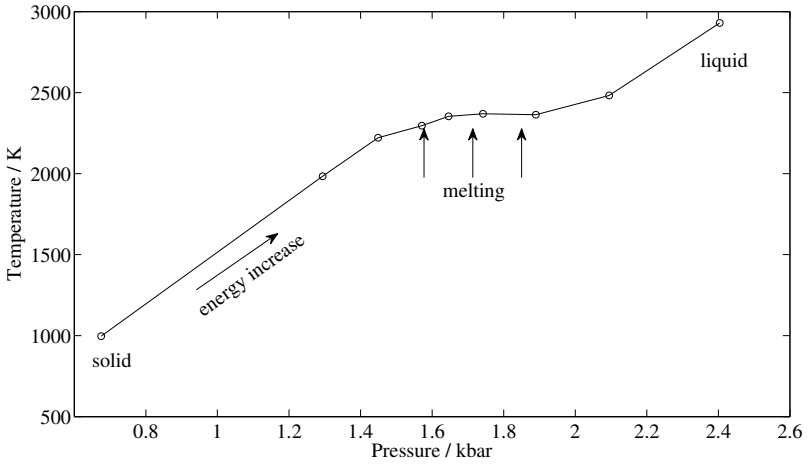

Figure 1.2: Fast-heating method (Z-method). This figure shows the temperature-pressure relation during the heating process. A Cu EAM potential (Mendelev, 2008) [5] is employed with 32 atoms in the system. Here NVE ensembles are simulated at different values of E. The melting temperature is located in the region where the temperature drops abnormally as more energy is put in. This figure also presents another problem of the method: Z-method melting occurs in a wide temperature range and hence the melting temperature is indefinite.

and liquid can coexist; the average temperature and pressure along the simulation then provide a point on the melting curve. If the energy E is above/below the range where coexistence can be maintained, the system will completely melt/solidify, and the simulation does not provide useful melting properties information.

The large-size coexistence is an accurate method, provided that the system size is sufficiently large. However, DFT calculations on such large systems are prohibitively expensive. To stabilize solid-liquid coexistence, it typically requires a cell with at least 1,000 atoms. Moreover, it usually takes at least thousands of MD steps to equilibrate the coexistence, which renders the cost skyrocket.

Fast-heating method (Z-method)

The fast heating method [11, 12, 13, 14] attempts to resemble how melting points are measured in common experiments. The procedure starts with a small cell of the solid at a low temperature. Then the temperature is gradually increased, with the atoms moving more vigorously. When the temperature becomes high enough, the

crystal melts. It is straightforward to determine the melting temperature because the latent heat during melting causes a temperature drop.

While the method is both simple and fast, it suffers from serious drawbacks [13, 15, 16]. Real melting in nature is usually initiated at surfaces and crystal defects. By comparison, melting in a defect-free periodic bulk solid is by no means the same. This so-called "homogeneous melting" has a widely acknowledged feature: superheating and hysteresis. The solid will remain in a metastable solid phase until the temperature is far above the true melting point. The reason for superheating is apparent. In order to initiate the nucleation of a liquid, the defect-free crystal needs extra energy (or temperature, correspondingly) to form a defect, the nucleation center. The amount of extra energy determines the extent of superheating, and hence the calculation error. Another related problem is about timescales, i.e., the kinetics of homogeneous melting. The chance to form a nucleation center depends not only on the activation energy, but also the amount of time elapsed. This relation leads to an annoying requirement of the method: very long MD trajectories are needed and they are never guaranteed long enough.

Free energy method

The free energy method [17, 18, 19, 20, 21] relies on separate calculations of the free energies of the solid and the liquid, and determines the melting temperature by locating the intersection of the two free energy curves. Among them, the liquid-state free energy calculation is the most difficult component [22]. Here we describe two typical methods.

- Thermodynamic integration method

  This method first calculates the free energy based on empirical potentials (e.g., by Widom's test-particle insertion method). Then in order to bridge the gap between the empirical potentials and DFT, a general technique called "thermodynamic integration" is carried out to determine the free energy correction. The basic idea is that the free energy difference represents the reversible work done

by isothermally switching the atomic interactions from the empirical potentials (H_α) to DFT (H_β).

$$\mu^\beta = \mu^\alpha + \frac{1}{N}\int_0^1 \left\langle H_\beta - H_\alpha \right\rangle_\lambda \mathrm{d}\lambda. \tag{1.1}$$

Here α and β are the empirical potentials and DFT, respectively. μ is free energy (chemical potential), and N is the number of particles. $\langle\cdots\rangle_\lambda$ denotes the ensemble average of the Hamiltonian $H_\lambda = (1-\lambda)H_\alpha + \lambda H_\beta$.

The success or failure of the scheme depends heavily on the quality of the empirical potentials, because it determines the effort needed to compute the free energy correction $\mu^\beta - \mu^\alpha$ [23]. A bad empirical potential would render the thermodynamic integration expensive. This problem becomes even worse in a complex multi-component system, when a huge number of high-quality potentials are required (e.g., at least C_N^2 pairwise empirical potentials for a N-element system). This requirement limits the application of the method. Furthermore, the thermodynamic integration method is inherently complicated and difficult to automate, since it requires a considerable amount of user-computer interactions.

- Two-phase thermodynamics method

This method [24, 25, 26] proposes a two-phase model, which decomposes the liquid-state phonon density of states (DoS) into a gas phase component and a solid phase. The gas component mostly contributes in the low frequency regime and contains all the fluidic effects, whereas the solid component, located at higher frequencies, has no fluidicity but can possess strong quantum effects. The liquid-state phonon DoS is easy to compute, and the free energy of a solid/gas phase is well studied. The choice of the gas phase model is flexible, e.g., hard spheres. However, a drawback of this method is its low accuracy, especially at high temperatures. This method decomposes the liquid-state phonon DoS to

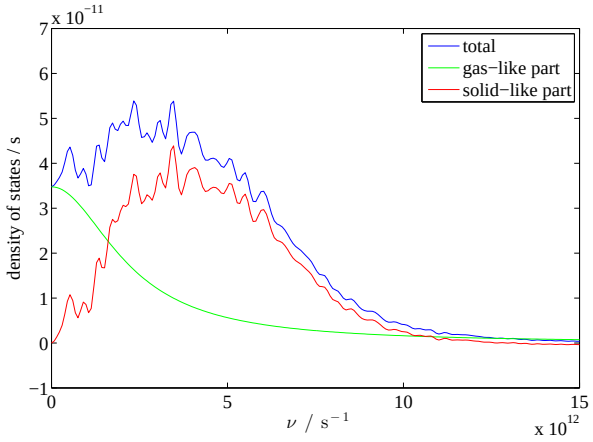

Figure 1.3: Two-phase thermodynamics method. This figure shows the partitioning of the liquid-state phonon density of states (blue, copper at 2000 K, PBE) into solid-like (red) and gas-like (green) parts whose free energies are straightforward to compute.

fictitious solid and gas components, which is an assumption not always valid. The liquid is not a combination of a solid and a gas in reality. In addition, the harmonic approximation employed in free energy calculations becomes poor at high temperatures, as anharmonic effects start to dominate.

1.2 Our goals

Although these popular methods are successful in a wide range of applications, they are far from perfect. Our primary goal is to devise methods that deliver a melting point estimate simply, quickly, and accurately. We summarize as follows a list of favorable features.

- *direct* DFT

  DFT has clear advantages over its competitors. It is robust and reliable in a very general range of systems (though under some circumstances its performance is limited). It is well balanced between accuracy and computational cost, providing relatively high accuracy with a modest computer demand. We believe an ideal method should stand on *direct* DFT calculations. A *direct* DFT approach circumvents the requirement for empirical potentials, a serious drawback of the

thermodynamic integration method. A direct DFT method is also simpler and easier to implement and automate.

- highly automated

  A highly automated approach reduces human effort and makes possible multi-tasking, i.e., to calculate melting points on several materials concurrently. With the increasing availability of computer power, this feature becomes more and more attractive when a task involves a large number of melting point calculations, such as solid-liquid phase diagram calculations and material screenings. Direct DFT is a key element to achieve automation: it takes considerable human effort to develop or search for empirical potentials. The difficulty varies to automate a method. For example, while the fast-heating method is straightforward to implement and automate, the thermodynamic integration method is inherently complicated and it requires heavy human input.

- fast and accurate

  These are essential features.

- robust and flexible

  A robust method is likely to remain effective when the environment changes. For example, the direct connection to DFT suggests general robustness in terms of atomic interactions. Another favorable feature is the ability to achieve high accuracy in several stages: low accuracy can be achieved at a low cost, and the accuracy can be improved systematically when more calculations are performed. This flexibility is ideal for material screening efforts.

In the next two chapters, we introduce two new methods: (1) an improved version of the Widom's particle insertion method based on high selectivity in carrying out DFT calculations on insertion energy, and (2) the small-cell coexistence method, which captures melting temperature from statistical analysis of duplicated small-cell solid-liquid coexistence simulations. Both methods operate through direct DFT calculations. The examples presented alongside demonstrates that they are efficient

and accurate. In particular, the small-cell coexistence approach is robust and easy to automate.

Chapter 2

Widom's particle insertion

Widom's test-particle insertion scheme [27] is a popular method to *directly* calculate the chemical potential of a liquid. Chemical potential is calculated as additional free energy, specifically, a change of free energy after inserting one more particle. Consequently, the chemical potential is related to the ensemble average and integration of Boltzmann's factors $\exp(-\beta\Delta U)$, where ΔU is insertion energy, the energy change during particle insertion. In practice, the average is evaluated by occasionally inserting the test particle into the simulation volume, measuring ΔU, and then removing it before continuing the simulation. This approach has been applied to some simple empirical potentials [28, 29, 30, 31, 32], mostly Lennard-Jones potentials. The major problem of the Widom method is that it is usually considered computationally too expensive, because most insertion attempts lead to a vanishingly small value of $\exp(-\beta\Delta U)$ (due to the high energy cost of inserting the test-particle in a small cavity in the dense system) and the corresponding computational efforts are thus wasted. Probably because of the prohibitive computational cost, there have apparently been no attempts so far to compute first-principles chemical potential directly with Widom's method.

Nevertheless, compared to the thermodynamic integration approach, the Widom method holds a great advantage, since it does not require any reference system. This property makes it possible to find a universal solution to first-principles calculations of liquid-state chemical potentials. This is especially useful in the automated materials screening effort, in which melting point is a design parameter, since one does not

need to develop empirical potentials for each of the chemical system explored. In this chapter, we revisit Widom's particle insertion method and modify it with an efficient cavity-sampling scheme, which achieves a drastic reduction in computational cost.

2.1 Methodology

2.1.1 Particle insertion method

We briefly reiterate the Widom particle insertion method here. By definition, chemical potential μ is the partial derivative of free energy F with respect to number of particles N, $\mu_i = \left(\frac{\partial F}{\partial N_i}\right)_{V,T,N_{j\neq i}}$, where V is volume and T is temperature. Thus it can be calculated by evaluating the additional free energy, namely the free energy change after inserting one more particle.

$$\mu_i = F(V,T,N_i+1,N_{j\neq i}) - F(V,T,N_i,N_{j\neq i}) + O\left(\frac{\partial^2 F}{\partial N_i^2}\right). \tag{2.1}$$

The higher-order derivative, which leads to finite-size correction, will be discussed later in Section 2.2.1. Assume the system of interest contains N homogeneous atoms. The Helmholtz free energy of such a system is (using a classical partition function)

$$F(V,T,N) = -kT\ln\left(\frac{1}{\Lambda^{3N}N!}\int \exp\left[-\frac{U(\mathbf{r}^N)}{kT}\right]\mathrm{d}\mathbf{r}^N\right), \tag{2.2}$$

where k is the Boltzmann constant, Λ is de Broglie wavelength, $\Lambda = \sqrt{h^2/(2\pi mkT)}$, and U is potential energy. Combining Eq. (2.1) and (2.2), the expression for chemical potential can be written as

$$\mu \simeq \Delta F_{N\to N+1} = \mu_{\mathrm{id}} + \mu_{\mathrm{ex}}, \tag{2.3}$$

$$\mu_{\mathrm{id}} = -kT\ln\left(\frac{V}{\Lambda^3(N+1)}\right), \tag{2.4}$$

$$\mu_{\mathrm{ex}} = -kT\ln\left(\frac{1}{V}\frac{\int \exp\left[-U(\mathbf{r}^{N+1})/kT\right]\mathrm{d}\mathbf{r}^{N+1}}{\int \exp\left[-U(\mathbf{r}^{N})/kT\right]\mathrm{d}\mathbf{r}^{N}}\right). \tag{2.5}$$

Notice that the approximation sign in Eq. (2.3) is due to the omission of the higher-order derivative in Eq. (2.1), which we will discuss and correct later.

In Eq. (2.3), we separate the chemical potential into two parts, the ideal gas term μ_{id} and the excess term μ_{ex}. The chemical potential of ideal gas is trivial to calculate. To compute the excess part μ_{ex}, we further write it as an ensemble average:

$$\mu_{\text{ex}} = -kT \ln \left(\frac{1}{V} \left\langle \int \exp\left(-\frac{\Delta U}{kT}\right) \mathrm{d}\mathbf{r}_{N+1} \right\rangle_N \right), \tag{2.6}$$

where ΔU is the potential energy change during insertion, $\Delta U(\mathbf{r}^N, \mathbf{r}_{N+1}) = U(\mathbf{r}^{N+1} = \{\mathbf{r}^N, \mathbf{r}_{N+1}\}) - U(\mathbf{r}^N)$. Notice the difference between $\mathbf{r}_i$ and $\mathbf{r}^N$. $\mathbf{r}_i$ denotes the position of the ith atom, while $\mathbf{r}^N$ contains the coordinates of all atoms in the configuration, which has a dimension of $3N$. The notation $\langle \cdots \rangle_N$ means the canonical ensemble average of a N-particle system

$$\langle A \rangle_N = \frac{\int A \exp\left[-U(\mathbf{r}^N)/kT\right] \mathrm{d}\mathbf{r}^N}{\int \exp\left[-U(\mathbf{r}^N)/kT\right] \mathrm{d}\mathbf{r}^N}. \tag{2.7}$$

In practice, the evaluation of Eq. (2.6) involves the calculation of two averages, namely the ensemble average $\langle \cdots \rangle_N$ and the spatial average $\frac{1}{V} \int \exp\left(-\Delta U/kT\right) \mathrm{d}\mathbf{r}_{N+1}$. The ensemble average can be achieved by picking snapshots of configurations $\mathbf{r}^N$ randomly from MD or MC trajectories, while the spatial average is calculated by thoroughly scanning over $\mathbf{r}_{N+1}$, the position of the additional particle, in each snapshot.

2.1.2 Selective sampling

An obvious way to calculate the spatial average would be to carry out a uniform random sampling of the additional particle in the $\mathbf{r}_{N+1}$ space. However, this is not a very practical approach. In practice, one can sample only a limited number of positions, and few of them would actually fall in the low energy region of interest. In the end, such a random sampling could turn out to be extremely expensive and

wasteful. Therefore an efficient sampling scheme is essential to avoid the random-sampling catastrophe.

It is more useful to regard the average in Eq. (2.6) as a one-dimensional integral over the insertion energy ΔU, i.e.,

$$\mu_{\text{ex}} = -kT \ln \left(\int_{-\infty}^{+\infty} \rho(\Delta U) \exp\left(-\frac{\Delta U}{kT}\right) \mathrm{d}(\Delta U) \right), \tag{2.8}$$

where $\rho(\Delta U)$ is the probability density defined as

$$\frac{1}{V} \left\langle \int \delta(U(\{\mathbf{r}^N, \mathbf{r}_{N+1}\}) - U(\mathbf{r}^N) - \Delta U) \, \mathrm{d}\mathbf{r}_{N+1} \right\rangle_N . \tag{2.9}$$

Notice again that $\langle \cdots \rangle_N$ is the canonical ensemble average of a N-particle system, according to Eq. (2.7).

In order to determine accurately the right-hand side of Eq. (2.8), one has to produce good estimates of the values of $\rho(\Delta U)$ for the range of ΔU over which the product $\rho(\Delta U) \exp\left(-\Delta U/kT\right)$ takes on its large values. In other words, the sampling should be exclusively focused on the region near the cavities that can accommodate the additional particle at a small energy cost.

Here we give an example of liquid copper at 2000 K. (see Fig. 2.1) Since chemical potential is determined by the area below the curve $\rho(\Delta U) \exp\left(-\Delta U/kT\right)$, which decays exponentially in high-ΔU region, we introduce here an energy ceiling (e.g., $\Delta U = 0.6$ eV in the figure) to focus on the study of low-ΔU region, ignoring the rest. The energy ceiling is simply determined as a value where the product $\rho(\Delta U) \exp\left(-\Delta U/kT\right)$ becomes negligible, thus the converged excess chemical potential μ_{ex} is captured at the lowest computational cost, which is proportional to the area below the probability density curve. (Throughout the text, we choose as reference state (zero level in energy) the enthalpy of Cu(s) at 298 K and zero pressure, which closely agrees with the definition employed in experiments.)

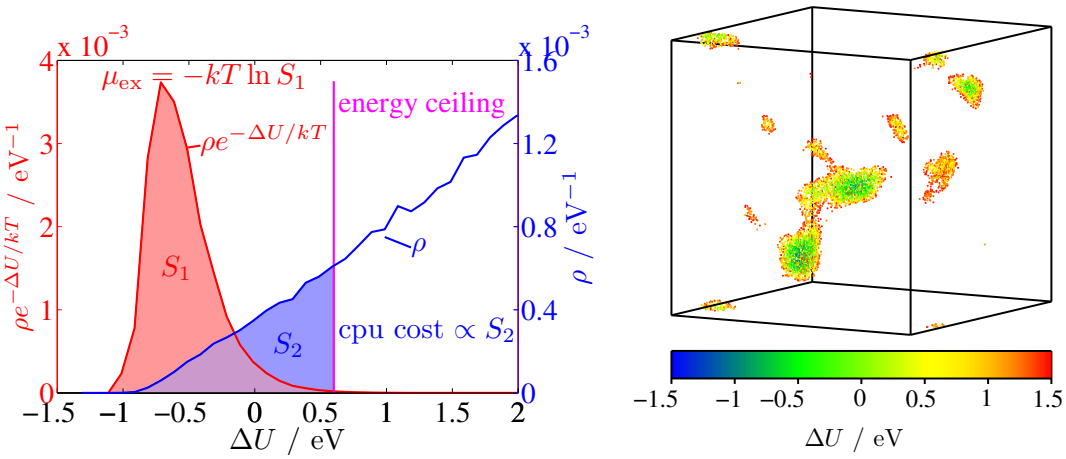

Figure 2.1: (a) Probability density $\rho(\Delta U)$ and the product $\rho(\Delta U)\exp\left(-\Delta U/kT\right)$ of liquid copper at 2000 K. (b) Volumetric display of the insertion energy ΔU for a single snapshot in configuration $\mathbf{r}^N$. The colored region with low ΔU contribute most to the chemical potential, despite of its small size and correspondingly modest computational cost, compared to the whole cube.

2.1.3 Algorithm

We propose here an algorithm to efficiently find the cavities and calculate the spatial average. For a N-particle configuration $\mathbf{r}_0^N$ in a parallelepiped, the integral can, in principle, be evaluated numerically on a uniform grid:

$$\begin{aligned} & \frac{1}{V}\int \exp\left(-\frac{\Delta U(\mathbf{r}_0^N,\mathbf{r}_{N+1})}{kT}\right)\mathrm{d}\mathbf{r}_{N+1} \qquad (2.10)\\ = \; & \frac{1}{N_aN_bN_c}\sum_{i,j,k=1}^{N_{a,b,c}}\exp\left(-\frac{\Delta U(\mathbf{r}_0^N,\mathbf{r}_{N+1}=\mathbf{r}_{ijk})}{kT}\right), \end{aligned}$$

where

$$\mathbf{r}_{ijk}=\frac{i}{N_a}\mathbf{a}+\frac{j}{N_b}\mathbf{b}+\frac{k}{N_c}\mathbf{c}. \qquad (2.11)$$

$\mathbf{a}$, $\mathbf{b}$, $\mathbf{c}$ are the vectors defining the parallelepiped. Instead of running *ab initio* calculations on all grid points, we employ the following algorithm to search for cavities and to study the potential energy surfaces near them.

Let Fig. 2.2 be the potential energy (ΔU) surface near the cavity of interest. We

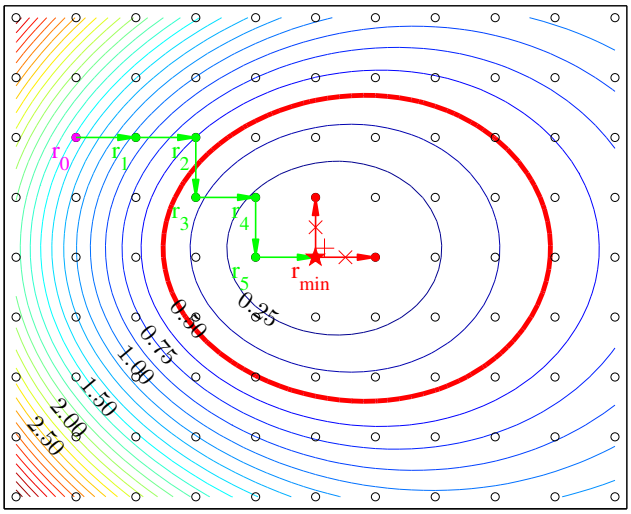

(a)

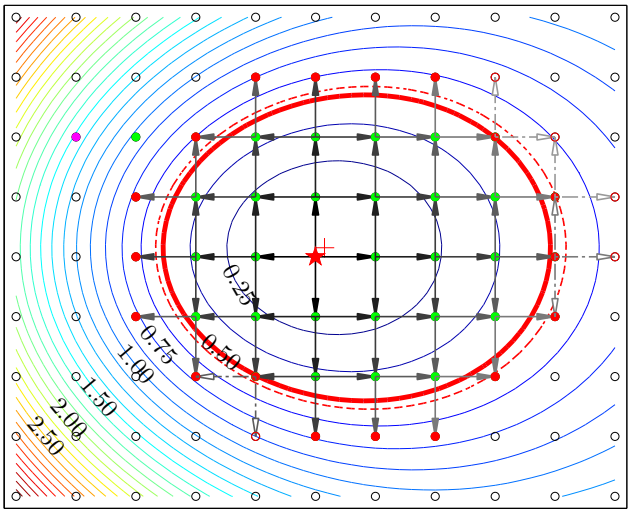

(b)

Figure 2.2: Diagrammatic illustration of the algorithm in two dimensions. Assume the contour lines above represent the energy surface near the cavity we are interested in. (a) Step 1: We first estimate the position of the cavity (purple, $\mathbf{r}_{N+1,0}$) based on an approximate energy function. Step 2: Then DFT calculations are carried out and, based on the force calculated, the position of the $(N+1)$th particle (green, $\mathbf{r}_{N+1,i}$) is optimized until the minimum grid point (red star, $\mathbf{r}_{N+1,\min}$) is found. The optimization proceeds as move attempts are accepted if $U(\{\mathbf{r}_0^N, \mathbf{r}_{N+1,i+1}\}) < U(\{\mathbf{r}_0^N, \mathbf{r}_{N+1,i}\})$. The green arrows are accepted move attempts, while the red ones are denied. (b) Step 3: All grid points below the energy ceiling (red circle) are studied with DFT, by gradually climbing up the energy surface from the bottom, until all frontier points (red solid dots) are above the energy ceiling. As a result, we need to calculate ΔU for the colored points only. Step 4: In case the dynamic energy ceiling needs to be increased (red dash circle), the "exploration" step restarts and demands additional calculations on new frontier points (red open dots).

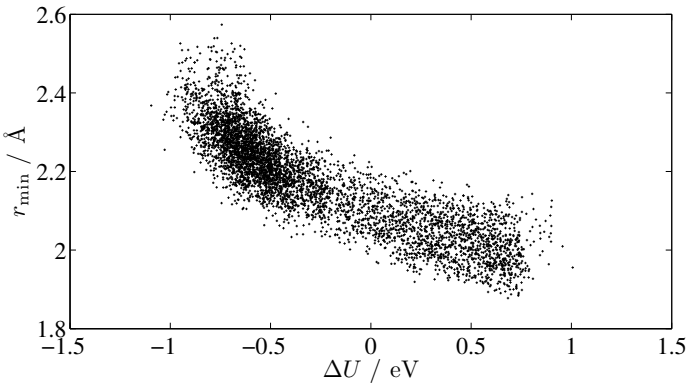

Figure 2.3: Nearest neighbor distance analysis on 256 configurations $\mathbf{r}^N$ of liquid copper at 2000 K. The nearest neighbor distance $r_{\min}$ is calculated as the shortest distance from the grid point $\mathbf{r}_{ijk}$ to the N atoms and their periodic images. Large $r_{\min}$ corresponds to the center of a large cavity, which is optimal for particle insertion at a low energy cost.

find this cavity and map out the nearby potential energy surface in four steps.

1. Locate: We first estimate the position $\mathbf{r}_{N+1,0}$ of the cavity based on an approximate energy function. This function should tell us roughly where the cavity is, but does not need to be accurate, because it is never used to calculate the chemical potential. There are plenty of choices available to take this task. For example, an appropriate empirical potential is definitely sufficient to predict the position of the cavity. In practice, we find that even a function as simple as nearest neighbor distance can help locate the cavity, as shown in Fig. 2.3. This idea of prescreening has been successfully used before [33, 34].

2. Minimize: DFT calculation is performed at the predicted position $\mathbf{r}_{N+1,0}$. Based on the force calculated on the $(N+1)$th particle, the position is optimized as $\mathbf{r}_{N+1,1}$. This move attempt is checked by DFT, and will be accepted if $U(\{\mathbf{r}_0^N, \mathbf{r}_{N+1,1}\}) < U(\{\mathbf{r}_0^N, \mathbf{r}_{N+1,0}\})$. The optimization continues and generates a series of positions $\{\mathbf{r}_{N+1,i}, i = 1, 2, \cdots\}$ until the minimum is found. This procedure is equivalent to structure optimization under the constraint that all atoms are fixed except the last one, which is allowed to move only on grid points.

3. Explore: We explore the cavity by gradually climbing up the potential energy

surface. If the bottom is lower than the energy ceiling, all its neighboring grid points will be studied. And if some of them are also below the ceiling, their neighbors will also be further calculated. This procedure spreads the "seeds" out, until all "seeds" hit the energy ceiling, which tells us that we have reached the inaccessible space region and there is no need to explore any more. The exploration will end only if all points on the frontier of the cavity are above the energy ceiling.

4. Converge: An appropriate value for the energy ceiling is required in Step 3. However, unlike what has been discussed in Fig. 2.1, the probability density $\rho(\Delta U)$ is never known before we calculate it, rendering the energy ceiling *a priori* unknown. We circumvent this problem by introducing a dynamic, rather than static, energy ceiling. Starting from a relatively low trial value (e.g., -0.5 eV in Fig. 2.1), we first calculate the probability density below it (by Step 3), and then decide whether or not we should raise the energy ceiling, depending on the up-to-date $\rho(\Delta U)\exp\left(-\Delta U/kT\right)$. The new energy ceiling, if it happens, may enclose some of the frontier points, thus restarting the exploration of the cavity (returning to Step 3). After the additional calculation is finished, the same question is asked again about whether to further increase the energy ceiling. Step 3 and Step 4 are performed repeatedly, increasing the energy ceiling gradually and mapping out Fig. 2.1 from left to right, until the energy ceiling is high enough to give an excess chemical potential converged within some prespecified tolerance.

2.2 An application: chemical potential and melting temperature of copper

2.2.1 Chemical potential of liquid copper at 2000 K

We employ the scheme described above to calculate the chemical potential of liquid copper from first-principles. Before we describe the detailed methodology, we would like to first estimate the precision required in our calculation, because we want to further apply the results to theoretical prediction of material properties, e.g., locating a melting point. We notice that the calculation of melting properties demands very high precision for chemical potentials. The melting temperature is determined by the intersection of chemical potential curves of a solid and a liquid. However, in practice these two curves usually cross at a shallow angle. Consequently, a small error in chemical potential may translate into a relatively large error in melting temperature. Typically, an error of 10 meV in chemical potential will result in an error of 100 K in melting point. Therefore, we need to make sure numerical and statistical errors are under control.

In the process of isochoric particle insertion, we use a periodic cube of edge length 11.66 Å with 108 copper atoms in it. All DFT calculations are performed using the VASP package [35, 36], with the projector-augmented-wave (PAW) implementation [37, 38] and the generalized gradient approximation (GGA) for exchange-correlation energy, in the form known as Perdew-Burke-Ernzerhof (PBE) [39]. Electronic temperature and its contribution to entropy are counted by imposing Fermi distribution of the electrons on the energy level density of states. The size of the plane-wave basis is carefully checked to reach the required accuracy. The energy cutoff (E_{cutoff}) is set to 273 eV in MD runs and particle insertion attempts. When we make corrections for pressure and energy, E_{cutoff} is increased to 500 eV in order to remove Pulay stress (error in pressure within 1 kbar) and achieve convergence (error in energy within 1 meV) with respect to the basis size.

The sampling in k-space is also studied very carefully, compromising between ac-

Table 2.1: Comparison of different k-space sampling in terms of computational cost and error (in unit of meV/atom).

k-space sampling	number	error in MD	error in ΔU
Γ point	1	46	106
MP $2 \times 2 \times 2$	4	2	6
MP $4 \times 4 \times 4$	32	< 0.1	1
8 special k-points[a]	8	< 0.1	3
4 special k-points[b]	4	0.5	19

a. The coordinates of the k-points are:
(1/8 1/8 1/8), (-3/8 1/8 1/8), (1/8 -3/8 1/8), (-1/8 -1/8 3/8),
(-1/8 3/8 3/8), (3/8 -1/8 3/8), (-3/8 -3/8 1/8), (3/8 3/8 3/8).
b. The coordinates and weights of the k-points are:
(1/8 1/8 1/8), 1/8; (3/8 1/8 1/8), 3/8; (3/8 3/8 1/8), 3/8; (3/8 3/8 3/8), 1/8

curacy and computation cost. A dense k-point gird is necessary to meet the accuracy requirement. Indeed, we would like to use a $4 \times 4 \times 4$ Monkhorst-Pack(MP) mesh in the first Brillouin zone (FBZ). However, since the point-group symmetry of our cubic supercell is broken by disorder, this would require all the 32 k-points included in the calculation, which is computationally too demanding. Kresse *et al.* [18] have addressed this problem by replacing the original 32 k-points with four special k-points in the irreducible FBZ, as if full cubic symmetry were still applied. This reduction can be well justified by the following argument. In the case of weak potential and nearly free electron gas, the dominant part in electronic Hamiltonian is the kinetic energy, which is approximately $\hbar^2/(2m_{\mathrm{e}})(\mathbf{G}+\mathbf{k})^2$ ($\mathbf{G}$ is a reciprocal lattice vector and $\mathbf{k}$ a k-point in FBZ), a term invarient under point-group operation with respect to the choice of $\mathbf{k}$. As simple metals are close to the free electron gas model, the same property should hold true, thus rationalizing the reduction of k-points by symmetry. Inspired by this idea and making a further improvement in which we seek a relatively even distribution of k-points in FBZ (while in Kresse *et al.*'s calculation, the k-space sampling focuses exclusively in the first octant), we represent the $4 \times 4 \times 4$ MP grid by eight special k-points, whose coordinates are listed in Table 2.1. To evaluate the accuracy, different k-space sampling methods are tested on ten randomly chosen MD configurations (calculated as $U(\mathbf{r}^N)/N$) and insertion attempts

Table 2.2: Calculation of Helmholtz free energy change $\Delta F_{N\to N+1}$ by particle insertion.(Cu, 2000 K, $N = 108$, $a = 11.66$Å, in eV)

$\overline{\mu}_{\text{ex}}$	0.748 ± 0.011
μ_{id}	-2.021
$\Delta F_{N\to N+1}$	-1.273 ± 0.011

(calculated as $\Delta U = U(\mathbf{r}^{N+1}) - U(\mathbf{r}^N)$). As Table 2.1 shows, sampling with the eight special k-points is comparable to the $4 \times 4 \times 4$ MP grid, while the computational cost is significantly reduced by a factor of four.

The ensemble average is computed numerically by running *ab initio* MD simulations within a canonical (NVT) ensemble with the Nosé-Hoover chain thermostat [40, 41, 42, 43]. The MD simulation proceeds with a time step of 3 femtoseconds and lasts for 1280 steps. Forces acting on atoms are accurately calculated, as the convergency threshold for electronic structure optimization is set to 1×10^{-8} eV/atom. We capture snapshots every 5 ionic steps from the MD trajectory, thus generating 256 snapshots in total, from which the ensemble average is evaluated. The configuration $\mathbf{r}^N$ in each snapshot is then studied by making particle insertion attempts in order to compute the spatial average over $\mathbf{r}_{N+1}$. The spatial average is calculated numerically on a uniform $40 \times 40 \times 40$ grid, according to Eq. (10). Only on selected grid points are *ab initio* insertion energies ΔU calculated, following the efficient scheme we proposed in Section 2.1.3. Finally, we compute the chemical potential by combining the ensemble and spatial averages.

As shown in Table 2.2, we "measured" the chemical potential of liquid copper at 2000K five times, based on five independent MD trajectories. The Helmholtz free energy change during particle insertion $\Delta F_{N\to N+1}$ is -1.273 ± 0.011 eV.

The selective calculation scheme helps us reduce the computational cost drastically. Instead of running *ab initio* calculations on all 1.6×10^7 grid points, the scheme demands calculations on only 5×10^3 grid points, reducing the computational cost by a factor of 3×10^3 and thus making the computation possible.

Now we make correction for the finite-size effect, which was alluded to earlier in Eq. (2.1) and (2.3). Several analytical expressions have been proposed [44, 45] for

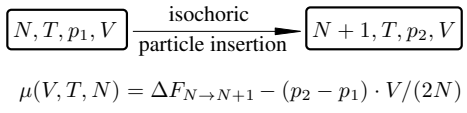

Figure 2.4: Finite-size correction to the calculation of chemical potential by isochoric particle insertion method.

this type of correction. Despite the differences, they all share the same leading term, $-\frac{1}{2N}\left(\frac{\partial p}{\partial \rho}\right)$, where ρ is the density of particles. Here we would like to account for the finite-size effect in the following way. The flaw of isochoric particle insertion lies in the fact that the next higher-order derivative may be significant and has to be included, which can be seen from the following Taylor expansion:

$$\begin{aligned} \Delta F_{N\to N+1} &= F(V,T,N+1) - F(V,T,N) \\ &\doteq \mu(V,T,N) + \frac{1}{2}\left.\frac{\partial \mu(V,T,n)}{\partial n}\right|_{n=N}, \end{aligned} \tag{2.12}$$

where $\Delta F_{N\to N+1}$ is the free energy change computed from particle insertion, $\mu(V,T,N)$ is the exact chemical potential, and $(\partial\mu/\partial n)$ is the leading correction term. Notice that this term is large for condensed phase materials, i.e., when n increases, μ will change significantly, as a result of the large increase in pressure. Simplifying the expression, we have the finite-size correction

$$\frac{\partial \mu(V,T,n)}{\partial n} = \frac{\partial \mu(p,T)}{\partial p}\cdot\frac{\partial p(V,T,n)}{\partial n} = \frac{V}{N}(p_2 - p_1), \tag{2.13}$$

$$\mu(V,T,N) = \Delta F_{N\to N+1} - \frac{V}{2N}(p_2 - p_1), \tag{2.14}$$

where p_1 and p_2 are the pressure before and after particle insertion, as shown in Fig. 2.4.

It is straightforward to show that this correction is equivalent to $-\frac{1}{2N}\left(\frac{\partial p}{\partial \rho}\right)$, the leading term in the corrections proposed by Smit [44] and Siepmann [45].

$$-\frac{V}{2N}(p_2 - p_1) = -\frac{V}{2N}\frac{\partial p(V,T,n)}{\partial n} = -\frac{1}{2N}\frac{\partial p(V,T,n)}{\partial \rho}. \tag{2.15}$$

Table 2.3: Theoretical chemical potential of liquid copper at 2000 K.(in eV, $N = 108, a = 11.66\text{Å}, p_1 = 5.5$ kbar, $p_2 = 10.6$ kbar)

$\Delta F_{N\to N+1}$	-1.273 ± 0.011
$-(p_2 - p_1)V/(2N)$	-0.023
$-p_1 V/N$	-0.050
$\mu(p^\circ, 2000\text{K})$	-1.347 ± 0.011
$\mu(p^\circ, 2000\text{K}, \text{exp.})$	-1.342

Another type of finite-size effect can be understood as the following. Compared to an infinite system, the test particle inserted in a small box will interact with its periodic images. In the case of charged atoms, the image charge interaction can be very large due to the long-range Coulomb interaction. In our small periodic model, image interactions must be examined to make sure that they are small enough to be neglected. To estimate this effect, we perform particle insertion tests on a 864-atom system (eight times larger than our original model) and make comparisons with the original results. The calculated insertion energies ΔU differ only by less than 3 meV. Thus it is safe to neglect the weak image interactions in our model.

We have now calculated $\mu(p_1, 2000\text{K})$. We further convert $\mu(p_1, T)$ to $\mu(p^\circ = 1 \text{ bar} \simeq 0 \text{ kbar}, T)$, the chemical potential at standard atmospheric pressure, to simplify the comparison of our theoretical results with experiments.

$$\mu_{p_1 \to p^\circ} = \mu(p^\circ, T) - \mu(p_1, T) \simeq -\frac{p_1 V}{N}. \tag{2.16}$$

The chemical potential is finally computed by combining Widom's particle insertion method and the corrections for finite-size effect and non-zero pressure.

$$\mu(p^\circ, T) = \Delta F_{N\to N+1} - \frac{V}{2N}(p_2 - p_1) - \frac{p_1 V}{N}. \tag{2.17}$$

As shown in Table 2.3, the theoretical chemical potential is predicted to be -1.347 ± 0.011 eV, which agrees very well with the experimental value -1.342 eV.

Table 2.4: Enthalpies and chemical potentials of liquid copper. (in eV/atom)

T	H	H_{exp}	μ	μ_{exp}
2000	-	-	-1.347 ± 0.011	-1.342
1950	0.642	0.645	-1.297 ± 0.011	-1.292
1850	0.609	0.611	-1.198 ± 0.010	-1.194
1750	0.575	0.577	-1.102 ± 0.010	-1.097
1650	0.540	0.543	-1.007 ± 0.009	-1.002
1550	0.505	0.509	-0.914 ± 0.009	-0.910
1450	0.470	0.475	-0.824 ± 0.008	-0.819
1350	0.434	0.441	-0.736 ± 0.008	-0.731

2.2.2 Chemical potential at various temperatures

The Gibbs free energies G at different temperatures and pressures are connected by the following thermodynamic relations:

$$\left[\frac{\partial(G/T)}{\partial(1/T)}\right]_p = H, \ \left[\frac{\partial G}{\partial p}\right]_T = V. \tag{2.18}$$

Since enthalpy H and volume V can be obtained directly from MD simulation, free energy changes among different (p, T) conditions can be readily computed by the thermodynamic integration method.

We start from the calculated $\mu(p^\circ, 2000\ \text{K})$ and map out the chemical potential curve in region $T \in [1300, 2000]$ K and zero pressure. To compute enthalpy H in Eq. (2.18), *ab initio* canonical (NVT) MD simulation is performed at various temperatures in the region. Detailed settings in DFT calculations and MD thermostat have been described in Section 2.2.1. Enthalpy is calculated as the average of energies over MD trajectory at each temperature. Volume search is conducted to make sure $p \simeq 0$ kbar. As shown in Table 2.4, the calculated enthalpy and chemical potential agree very well with experiments.

2.2.3 Calculation of melting temperature

The chemical potential of liquid copper is further used to calculate the theoretical melting temperature, which is determined by the intersection of chemical potential

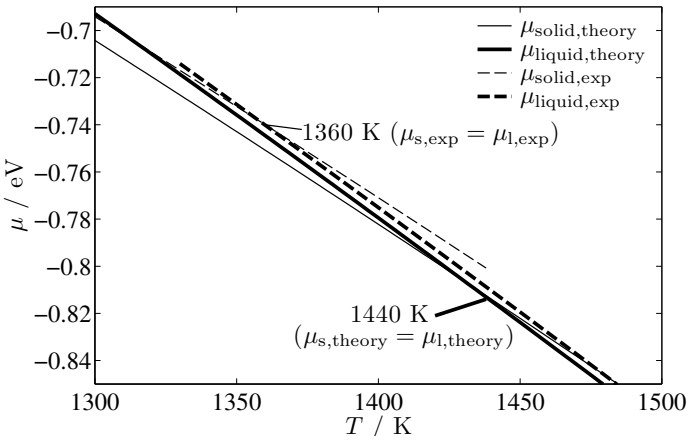

Figure 2.5: Determine melting temperature from where solid and liquid chemical potential curves intersect on a μ-T plot. T_{m} from experiments is 1360 K. According to the liquid chemical potential we calculated by Widom's method, the theoretical T_{m} is 1320 or 1460 K, depending on whether we use experimental or theoretical results for the chemical potential of solid.

curves of the solid and of the liquid. The chemical potential of solid is computed within the quasiharmonic approximation [46] and is further corrected by thermodynamic integration (to account for anharmonicity at high temperatures). Phonon density of states, vibrational free energies, and thermal expansion are calculated using the "supercell" method as implemented in the Alloy Theoretic Automated Toolkit (ATAT). [47, 48] Anharmonicity effect is included as further correction through the thermodynamic integration method, in which MD simulation is carried out with an effective Hamiltonian

$$H_\lambda = (1-\lambda)H_\alpha + \lambda H_\beta \tag{2.19}$$

that gradually switches from the Hamiltonian H_α of a harmonic potential surface to the real Hamiltonian H_β. The chemical potential difference is calculated as

$$\mu^\beta = \mu^\alpha + \frac{1}{N}\int_0^1 \left\langle H_\beta - H_\alpha \right\rangle_\lambda \mathrm{d}\lambda, \tag{2.20}$$

where $\langle A \rangle_\lambda$ is the average of observable A in MD simulation with Hamiltonian H_λ.

The chemical potentials of solid and liquid copper, from both theory and experiment, are shown in Fig. 2.5. Compared with experiments, the errors of liquid and

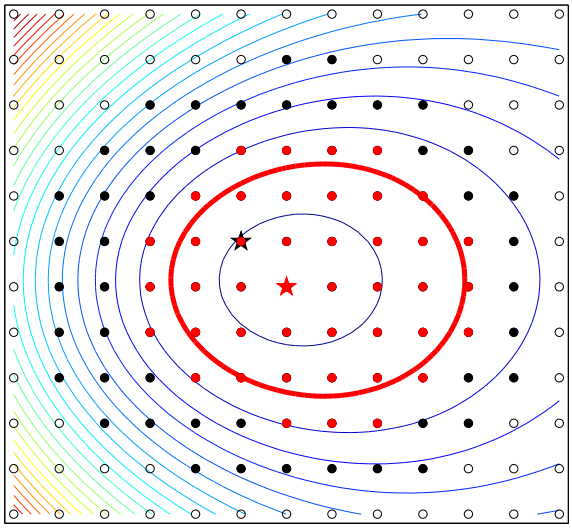

Figure 2.6: This two-dimensional energy surface illustrates why our four-step algorithm works more efficiently than pre-screening. While traditional pre-screening labels all colored (both red and black) points as "important" based on the approximate energy model, the "locate" step in our algorithm outputs only the approximate minimum (a single grid point at the black star). Then the cavity is studied by the "minimize" and "explore" steps relying on *ab initio* calculations. As a result, our scheme calculates only the red points, and significantly cuts the unnecessary cost (all the surrounding black points).

solid are -5 and -11 meV, respectively, in the melting region. The calculated melting temperature is 1440 K, about 80 K higher than the experimental value. This error is translated from both solid and liquid chemical potentials, as a combined effect. Since we focus mostly on the calculation of liquid chemical potentials in this article, we are more concerned about the impact purely from the liquid part, which is more accurate than the solid part and thus should lead to a smaller error. Indeed, the errors in melting point caused by solid and by liquid are 120 and -40 K, respectively, as shown in Fig. 2.5.

2.3 Discussions

2.3.1 Difference with pre-screening

Although the "locate" step in our algorithm appears to be similar to pre-screening, it is different in many aspects. Working in *ab initio* context, which is computationally much more expensive than empirical potentials, we need to design an algorithm highly selective about what should be calculated by DFT. In traditional pre-screening, the approximate energy model is used to find an approximate cavity that must completely enclose the true cavity, so the pre-screening criterion must necessarily be conservative and the more accurate/expensive energy model is invoked too often. The key distinction in our scheme is that the approximate energy model is only used to find a trial point at or near a cavity. The shape of the cavity is instead determined in the "explore" step, relying on *ab initio* calculations, and the only "wasted" calculations are those immediately at the boundary of the cavity. In traditional pre-screening the set of "wasted" calculation points is three-dimensional, while in our scheme it is two-dimensional. An example is shown in Fig. 2.6. We save costs on several layers of black points that are labeled as "important" by pre-screening but proven to be unnecessary by our algorithm.

One may argue that near the boundary of the cavity there could exist multiple minima, which could be ignored by mistake in our algorithm. Although it is true theoretically, this is very unlikely to happen in reality. First of all, if the multiple minima are connected by a path lying below the energy ceiling, we will not miss them in the "explore" step. In the case of multiple minima not connecting, we will miss them only if the "locate" step provides a single starting point when there should have been more than two. This is not only very rare but also insignificant, because only small-size shallow cavities can escape from the examination of the "locate" step. Furthermore, the multiple minima issue is more a numerical convergence aspect than a fundamental limitation. As the ceiling is dynamically increased up to convergence, all minima that were previously missed will eventually be connected to existing cavities by a path below the energy ceiling.

2.3.2 DFT error

Although the absolute error in DFT energies is likely larger than our target accuracy of 10 meV/atom, we benefit from the fact that our results (the melting point and chemical potentials relative to a reference state) are actually functions of energy differences between states of similar atomic densities and average coordination number, so that considerable error cancellation is to be expected.

Potential DFT errors aside, we are very careful about controlling the errors both from numerical and statistical origins. The errors in the *ab initio* calculations are mainly due to electronic structure calculations implementation details, e.g., the use of PAW method, the size of basis set and k-space sampling. These problems have been carefully handled and discussed either in the above paragraph or in Section 2.2.1. The errors in statistical methods are caused by detailed physical approaches to calculate the chemical potentials of the solid and of the liquid, i.e., quasi-harmonic approximation, thermodynamic integration, and Widom's particle insertion method. Because the chemical potentials of the two phases are calculated with different statistical mechanics methods, we have to make sure that the calculations achieve absolute convergence with respect to the methods, since there is no chance that errors of the two phases will cancel.

2.3.3 Finite-size error

Due to computational cost issues of DFT calculations, our chemical potential calculations can be performed only on a small system with around 100 atoms. The error caused by the small system size is studied systematically, as we gradually increase the system size and check the convergence. We first note that this error is inherent in the physical method of particle insertion itself and is irrelevant to the DFT formalism. Therefore, it is better to work with empirical potentials, as it is a practical way to test our method on large system size without losing the accurate description of interatomic interactions. We implement the particle insertion method into the large-scale atomic/molecular massively parallel simulator package (LAMMPS) [49]

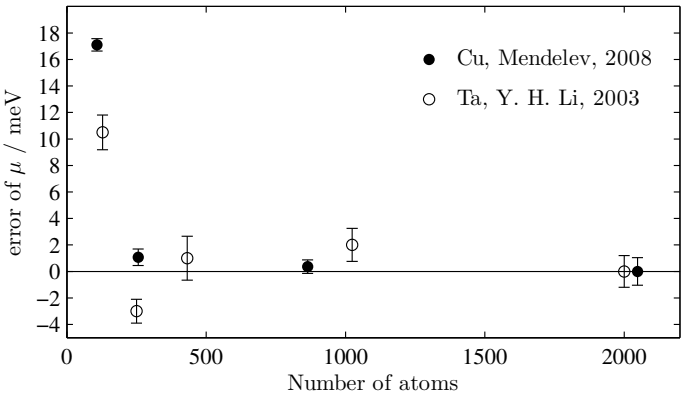

Figure 2.7: Finite size error of chemical potential calculations, tested on two empirical potentials. The errors are 17 and 11 meV for Cu (108 atoms) and Ta (128 atoms), respectively.

to automate and accelerate the calculations. Two embedded atom model (EAM) potentials, namely copper (Mendelev, 2008) [5] and tantalum (Y.-H. Li, 2003) [50], are tested on system size up to 2,000 atoms. The results are shown in Fig. 2.7. We find the chemical potential finally converges after we increase the system size beyond 1,000 atoms. With system size of approximately 100 atoms, the finite size error is 10-20 meV. Considering the huge computation cost we have to pay to work on larger systems from first principles, this amount of error is still acceptable.

2.3.4 Dependence on numerical grid

The convergence with respect to grid resolution is studied with the same empirical potentials. We have tested different grid resolutions up to eight times denser than the grid in our reported DFT calculations. We analyze the results in two levels, namely the integral I (or spatial average mentioned before in Eq. (10)) in each individual snapshot and the chemical potential μ according to Eq. (6), which is related to the ensemble average of the above-mentioned integrals I, $\mu = -kT \ln \langle I \rangle_N$. Errors of spatial average in individual snapshots are plotted in Fig. 2.8 (blue cross). Although for a single snapshot it requires a very fine grid to achieve convergence, the error mostly cancels out in the ensemble average, therefore the chemical potential calculated from them converges quickly with respect to the grid resolution, as shown

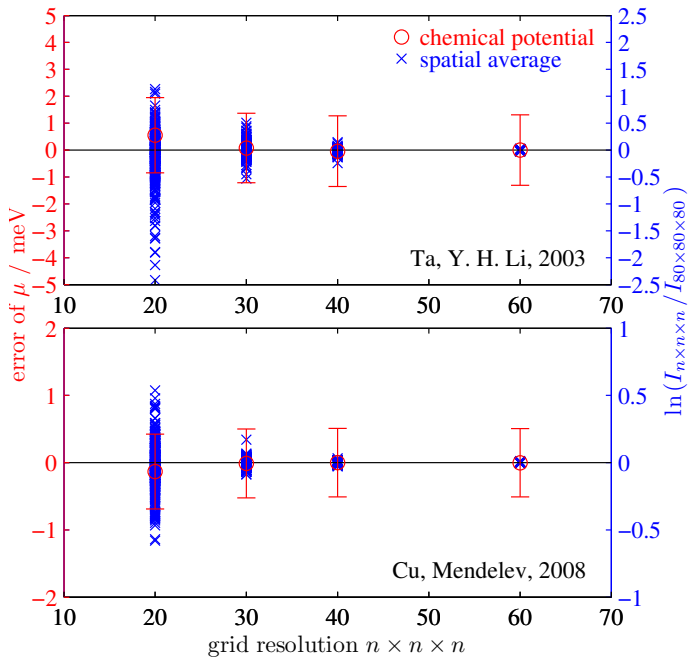

Figure 2.8: Convergence tests carried out on different grids. Results from the densest grid ($80 \times 80 \times 80$) are chosen as benchmarks. The error of each single snapshot integral $I_{n\times n\times n}$ is calculated as $\ln\left(I_{n\times n\times n}/I_{80\times 80\times 80}\right)$. Chemical potentials converge quickly with respect to grid resolution.

in Fig. 2.8 (red circle). We find that the results have already converged with a $40 \times 40 \times 40$ grid, which is employed in our DFT calculations.

2.3.5 Multi-component system

The method is easily generalizable to multi-component system, since one can compute the chemical potential of each species separately and exploit their partial molar property to obtain the Gibbs free energy of the phase from $\sum_i n_i\mu_i$. The only exception to this simple approach occurs when there are large electrostatic interactions that give rise to sharply varying free energies as a function of deviations from perfect stoichiometry, so that finite size effects are highly non-negligible. In this case, one way to avoid this issue is to insert multiple particles simultaneously to preserve stoichiometry, in which case the method would directly provide the Gibbs free energy of the phase at the expense of higher computational requirements, because the integrals become $3 \times \sum_{i=1}^{m} n_i$ dimensional (for $A_{n_1}B_{n_2}\cdots M_{n_m}$).

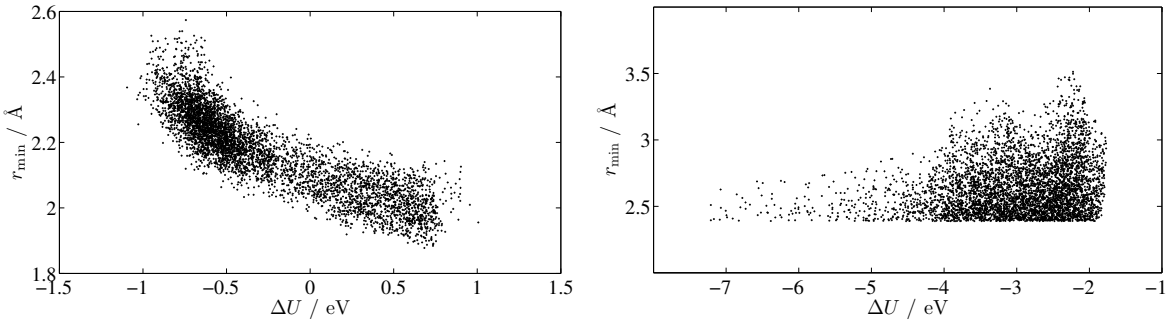

(a) Cu (b) $La_2Zr_2O_7$

Figure 2.9: Correlation between insertion energy and size of cavity. While the study of liquid copper shows a clear correlation, it is absent in $La_2Zr_2O_7$, leading to the failure of the algorithm.

2.3.6 Disadvantage: locating the right cavities

The success or failure of the particle insertion scheme depends heavily on whether sufficiently many large cavities are sampled and explored. Therefore higher temperatures are preferable, since rare events occur more frequently (configurations with large cavities usually locate in high-energy region of phase space and are rarely visited). We find that it is much easier to measure the chemical potential at 2000 K than at 1500 K. At the latter temperature, the chemical potential is significantly overestimated by a few tens of meV due to the lack of large cavities explored during the limited time of MD simulation.

2.3.7 Failure: the larger the cavity, the better?

The locate-minimize-explore-converge algorithm relies on (1) the energy function (in the "locate" step) to roughly tell the location of the cavity and (2) the general principle that a larger cavity is more likely to accommodate an inserted atom. While these assumptions work well in a dense liquid such as copper (Fig. 2.9(a)), its validity is undermined in certain circumstances. For instance, lanthanum zirconate ($La_2Zr_2O_7$) is a spacious liquid, meaning there are many large holes in it. The insertion energy does not correlate with the size of the cavity (Fig. 2.9(b)). This phenomenon is understandable: rather than hanging at the center of the cavity (which is too far

from the other atoms), the additional atom prefers staying at the edge in order to form effective bonds. This scenario is very hard for the algorithm to handle. Because of the large number of cavities, the large volume of cavity space, and the lack of correlation between insertion energy and cavity size, the algorithm fails to maintain high selectivity when DFT calculations are carried out, and indeed a large portion of calculations are wasted. As a result, the computational cost starts to skyrocket.

2.4 Conclusions

We demonstrate that it is computationally practical to calculate the chemical potential of a liquid directly from first principles using a modification of Widom's particle insertion method. This, to the authors' knowledge, is the first attempt to evaluate the chemical potential of a liquid without the help of any high-quality empirical potentials, which are available only for a limited number and type of materials. This distinct advantage is crucial when such empirical potentials are difficult to obtain, e.g., for multi-component materials. An algorithm is proposed to efficiently find and study cavities. It reduces the computational cost drastically, e.g., by more than three orders of magnitude for the example we study, relative to Widom's original method. After finite-size correction, the calculated chemical potential of liquid copper at 2000 K is -1.347 eV, only 5 meV lower than the corresponding experimental value. This result is used to further map out the chemical potential curve of liquid-state copper as a function of temperature at zero pressure by the thermodynamic integration method. Finally, a melting point is predicted by locating the intersection of the calculated chemical potential curves of the solid and of the liquid. The error in calculated melting temperature is 80 K.

Chapter 3

Small-cell solid-liquid coexistence

We develop the small-cell solid-liquid coexistence method as a simple and quick approach to deliver a melting point estimate whose accuracy can be systematically improved if more calculations are performed. This capability is ideal for material screening efforts and solid-liquid phase diagram calculations.

The idea derives from both the traditional coexistence and fast-heating methods (see Chapter 1.1). Despite their disadvantages, we find that these two methods are complementary to each other, and they shed light on the search for an automated melting temperature predictor. For example, while the coexistence method demands a large system size that skyrockets the computer cost, the fast-heating method requires only a small size. Also, while the fast-heating method suffers from hysteresis due to the high energy barrier between the solid and liquid phases, the solid-liquid interface in the coexistence method creates a channel between the two phases so they are free to exchange, and the hysteresis is removed. These observations naturally suggest the possibility of combining these two methods.

Let us imagine the case of small-cell solid-liquid coexistence and compare it with the traditional large-size approach. We expect to gain a significant speed boost as the system size is significantly reduced. At the same time, we will certainly face another problem: the interface is not stable in small systems. In isothermal-isobaric (constant NPT) simulations, the system will quickly turn into a pure state, either solid or liquid, and never go back again to the coexisting state during the short MD time scale (~ 10 ps) we can reach.

We resolve this problem by employing statistical analysis on the MD trajectories. We find that the small-size coexistence simulation contains plenty of thermodynamic information, though it fails to maintain two stable phases. When two phases coexist at the beginning, the system evolves following thermodynamic rules which govern the transition between the two phases and affect the probability distribution of the final pure states. By running many parallel small-size coexistence simulations and analyzing this probability distribution, we can obtain the relative stability of the two competing phases.

3.1 Methodology

3.1.1 Computational techniques

A schematic illustration of the idea is shown in Fig. 3.1. Solid-liquid coexisting systems are prepared by heating and melting half of the solid, while the other half is fixed frozen. Starting from a set of different coexistence configurations, isothermo-isobaric (NPT) MD simulations are carried out to trace the evolution. After several picoseconds, the two interfaces annihilate with each other and all simulations end with homogeneous phases, either solid or liquid. For instance, Fig. 3.2(a) shows the evolution of the 50 MD trajectories of bcc Tantalum and its liquid at 3325 K. A distribution of finally states, either solid or liquid, is evident. We can sample MD duplicates over a number of temperatures and fit a melting temperature based on the statistical distribution, as shown in Fig. 3.2(b).

3.1.2 Theory: probability distribution

We attempt to extract information regarding the melting temperature from the ratio $N_{\text{liquid}}/N_{\text{solid}}$, where N_{liquid} and N_{solid} are, respectively, the number of simulations that terminate in a completely liquid or completely solid state starting from an initial half-half solid-liquid coexistence. To calculate this ratio, we view the interface position x (defined by the atomic fraction of liquid phase) as obeying a random walk with a

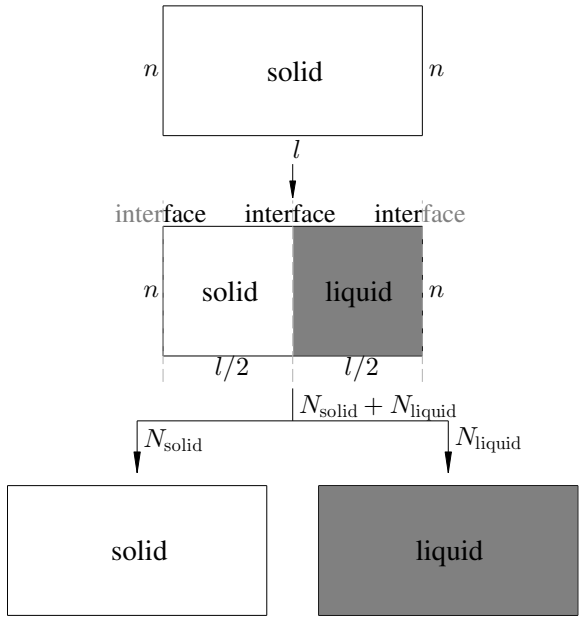

Figure 3.1: Schematic illustration of how the small-size coexistence method is executed in practice. Starting from the $n \times n \times l$ supercell with atoms in their ideal solid positions, we heat and melt the right half to obtain solid-liquid coexistence configurations. Then many parallel NPT MD simulations (here a total of $N = N_{\text{solid}} + N_{\text{liquid}}$) are performed in order to measure the probability distribution.

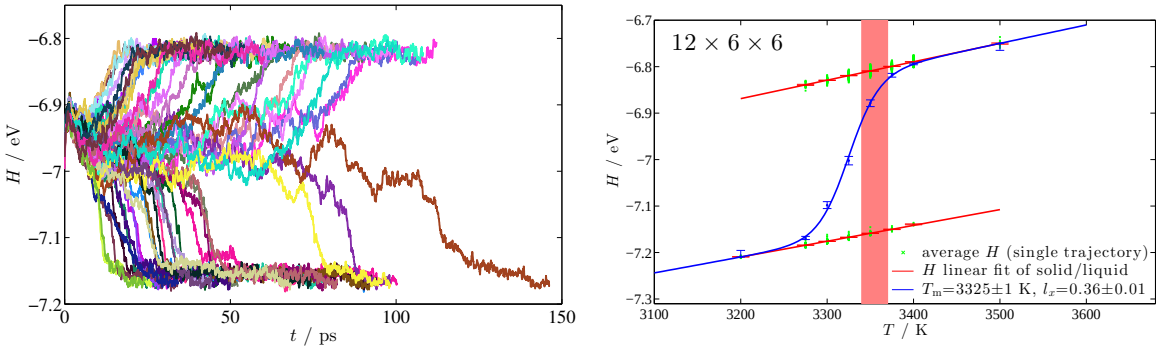

(a) (b)

Figure 3.2: (a) Enthalpy H versus time t shows the evolution of 50 independent MD systems ($6 \times 6 \times 12$ supercell, 864 atoms) at 3325 K. In terms of enthalpy, lower enthalpy corresponds to a solid, while higher enthalpy a liquid. It is clear that each trajectory finally ends in a pure phase, either solid or liquid, after a certain amount of time. (b) The melting properties fitted according to Eqs. (3.7) to (3.10). The average enthalpies are shown in green dots. The solid and liquid parts (two red lines) are first fitted separately to obtain enthalpies and heat capacities, according to Eqs. (3.8) and (3.9). Then we combine the two phases and fit to Eq. (3.10) to compute melting temperature. The predicted melting temperature agrees with the benchmarks (the pink vertical bin).

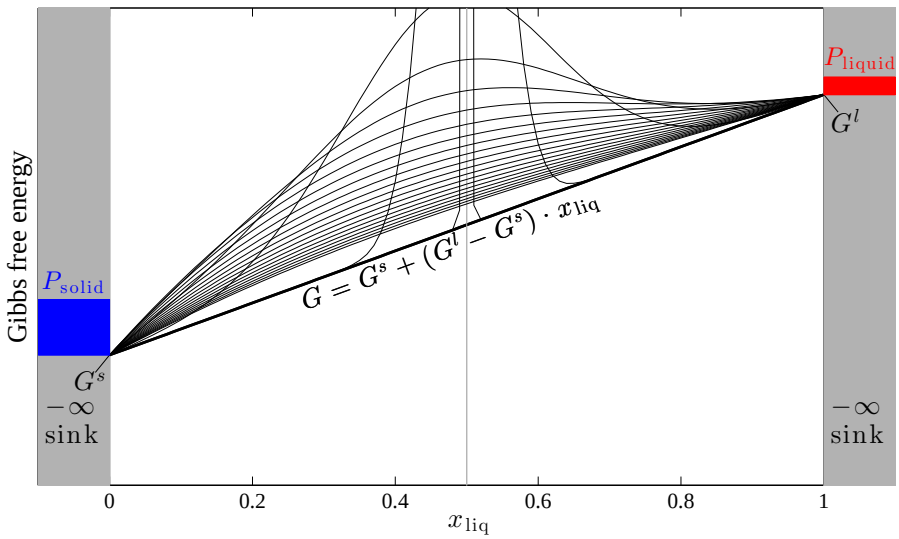

Figure 3.3: Free energy profile and probability distribution of the final states. The free energy of solid-liquid coexisting system is a linear combination of the two single phases. The system starts as a δ function at the center and undergoes a tilted random walk, during which it spreads out due to diffusion and slides towards the state with a lower free energy (here the solid phase). The probability distribution ratio of the solid (blue) and liquid (red) is equivalent to $N_{\text{solid}}/N_{\text{liquid}}$.

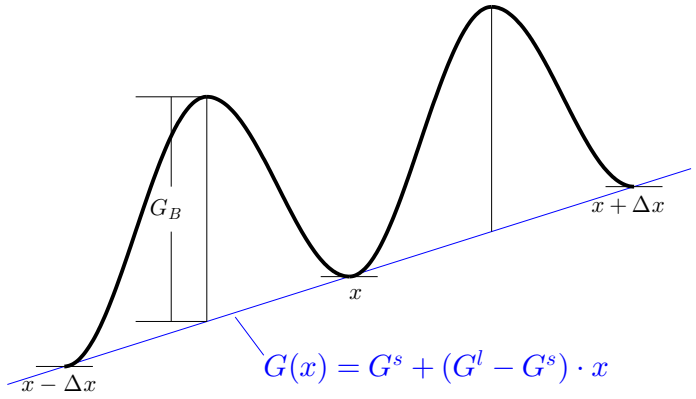

Figure 3.4: We derive the evolution of coexisting system and probability distribution based on transition state theory.

drift related to the free energy difference between the liquid and the solid phases, as shown in Fig. 3.3. The initial state is $x = 0.5$ and we track the system until it reaches either $x = 0$ or $x = 1$, which are considered completely "absorbing" states because the formation free energy of the interface is so large that, once it has disappeared, it would not reappear in a time frame reachable by our simulations. In between those two absorbing states, the free energy of the system is given by $G(x) = G^s + G^{l-s}x$, with $G^{l-s} \equiv G^l - G^s$ and where G^l and G^s respectively denote the free energies of the whole system if it were entirely liquid or entirely solid.

In a time step Δt, the system can jump from x to $x + \Delta x$ or to $x - \Delta x$ or stay in place at x, as in Fig. 3.4. The system jump with an attempt frequency ν (which can be assumed constant, without loss of generality, since the activation entropy can absorb any change in ν). When jumping from x to $x + \Delta x$, the system faces a free energy barrier $G_B + G^{l-s}\Delta x/2$, where G_B is a barrier measured relative to the average free energy of the initial and final states. The probability of jumping from x to $x+\Delta x$ in a time interval Δt is thus:

$$p_{x\to x+\Delta x} = \nu \exp\left(-\beta\left(G_B + G^{l-s}\Delta x/2\right)\right)\Delta t, \tag{3.1}$$

where $\beta = (k_B T)^{-1}$ and k_B is Boltzmann's constant. Similarly, the probability of jumping from x to $x - \Delta x$ is:

$$p_{x\to x-\Delta x} = \nu \exp\left(-\beta\left(G_B - G^{l-s}\Delta x/2\right)\right)\Delta t. \tag{3.2}$$

To avoid carrying through unnecessary quantities, it is convenient to work with jump probabilities conditional on a jump (by either $+\Delta x$ or $-\Delta x$) taking place, given by,

$$\tilde{p}_{x\to x+\Delta x} \equiv \frac{p_{x\to x+\Delta x}}{p_{x\to x+\Delta x} + p_{x\to x-\Delta x}}, \tag{3.3}$$

$$\tilde{p}_{x\to x-\Delta x} \equiv \frac{p_{x\to x-\Delta x}}{p_{x\to x+\Delta x} + p_{x\to x-\Delta x}}. \tag{3.4}$$

As the system undergoes a random walk, the interface position, goes through a se-

quence of values x_i. A useful observation is that, for any sequence x_i converging to 1 there exists a corresponding sequence $\bar{x}_i \equiv 1 - x_i$ converging to 0. In general, the two sequences don't necessarily have the same probability. Indeed, the ratio of their probabilities can be derived as follows: let r and l be the number of times x_i jumps towards $+\Delta x$ and towards $-\Delta x$, respectively. Note that

$$\begin{aligned}
&\frac{\prod_{i=1}^{l+r} \tilde{p}_{x_i \to x_{i+1}}}{\prod_{i=1}^{l+r} \tilde{p}_{\bar{x}_i \to \bar{x}_{i+1}}} \\
= &\prod_{i=1}^{l+r} \frac{\tilde{p}_{x_i \to x_{i+1}}}{\tilde{p}_{(1-x_i)\to\left(1-x_{i+1}\right)}} = \prod_{i=1}^{l+r} \frac{p_{x_i \to x_{i+1}}}{p_{(1-x_i)\to\left(1-x_{i+1}\right)}} \\
= &\frac{\left(\exp\left(-\beta G^{l-s}\Delta x/2\right)\right)^r \left(\exp\left(\beta G^{l-s}\Delta x/2\right)\right)^l}{\left(\exp\left(\beta G^{l-s}\Delta x/2\right)\right)^r \left(\exp\left(-\beta G^{l-s}\Delta x/2\right)\right)^l} \\
= &\exp\left(-\beta G^{l-s}\Delta x\,(r-l)\right) \\
= &\exp\left(-\beta G^{l-s}/2\right), \qquad (3.5)
\end{aligned}$$

since if x_i goes from 1/2 to 1, then $\Delta x\,(r-l) = 1/2$. Now, if we consider every possible path x_i (of any length) going to 1, the ratio of the total probabilities is:

$$\begin{aligned}
\frac{N_{\text{liquid}}}{N_{\text{solid}}} &= \frac{\sum_{\{x_i\}} \prod_i \tilde{p}_{x_i \to x_{i+1}}}{\sum_{\{x_i\}} \prod_i \tilde{p}_{(1-x_i)\to\left(1-x_{i+1}\right)}} \\
&= \frac{\sum_{\{x_i\}} \exp\left(-\beta G^{l-s}/2\right) \prod_i \tilde{p}_{(1-x_i)\to\left(1-x_{i+1}\right)}}{\sum_{\{x_i\}} \prod_i \tilde{p}_{(1-x_i)\to\left(1-x_{i+1}\right)}} \\
&= \exp\left(-\beta G^{l-s}/2\right) \frac{\sum_{\{x_i\}} \prod_i \tilde{p}_{(1-x_i)\to\left(1-x_{i+1}\right)}}{\sum_{\{x_i\}} \prod_i \tilde{p}_{(1-x_i)\to\left(1-x_{i+1}\right)}} \\
&= \exp\left(-\beta G^{l-s}/2\right). \qquad (3.6)
\end{aligned}$$

The factor 1/2 in this Boltzmann-like expression arises because our probabilities are conditional on the system starting in specific state (half liquid, half solid) and ending in one of the two specific states (entirely liquid or solid). If the system were started in a randomly chosen state and were left to evolve indefinitely (repeatedly melting and solidifying at random), then the ratio of the probabilities of the simulation cell being

all liquid and all solid would yield, asymptotically, the usual Boltzmann expression $\exp\left(-\beta G^{l-s}\right)$, without the 1/2 factor.

Since G^{l-s} equals zero at melting temperature, one could locate melting temperature at where N_{liquid} equals N_{solid}. However, it is not an efficient way to proceed because it usually takes several iterations to approach melting temperature while all the trial calculations (away from the melting temperature) are wasted. To avoid this, we propose the following fitting method which not only takes advantages of all available calculations, but also yields more melting properties in addition to the melting temperature.

We compute the ratios $f(T) = N_{\text{liquid}}/(N_{\text{solid}}+N_{\text{liquid}})$ on a set of different temperatures. As T increases, G^{l-s} turns gradually from positive to negative, so f changes smoothly from 0 to 1. Thus we can obtain melting temperature throught fitting the expression. In practice, in order to calculate more melting properties, we combine this relation with enthalpy, since it can be easily calculated as an average over an MD trajectory:

$$H(T) = H^s(T) + H^{l-s}(T)\frac{\exp\left[-\beta G^{l-s}(T)/2\right]}{1+\exp\left[-\beta G^{l-s}(T)/2\right]}, \tag{3.7}$$

where

$$H^s(T) = H^s(T_m) + C_p^s(T - T_m), \tag{3.8}$$

$$H^{l-s}(T) = H^{l-s}(T_m) + C_p^{l-s}(T - T_m), \tag{3.9}$$

$$G^{l-s}(T) = \frac{T_m - T}{T_m}H^{l-s}(T_m) - C_p^{l-s}\frac{(T-T_m)^2}{T_m}. \tag{3.10}$$

By fitting $H(T)$ to T, we obtain melting properties, e.g., melting temperature T_m, solid and liquid enthalpies $H^{s/l}(T_m)$ at T_m, and heat capacities $C_p^{s/l}$. We derive Eq. (3.10) as follows:

$$S^{s/l}(T) = S^{s/l}(T_m) + C_p^{s/l}\ln\frac{T}{T_m}, \tag{3.11}$$

$$
\begin{aligned}
& G^{l-s}(T) = G^{l}(T) - G^{s}(T) \\
= \;& H^{l-s}(T) - TS^{l-s}(T) \\
= \;& H^{l-s}(T_m) + C_p^{l-s}(T - T_m) - TS^{l-s}(T_m) - TC_p^{l-s} \ln \frac{T}{T_m} \\
= \;& (T_m - T)S^{l-s}(T_m) + C_p^{l-s}\left[T - T_m - T \ln \frac{T}{T_m}\right] \\
= \;& (T_m - T)S^{l-s}(T_m) - C_p^{l-s}\frac{(T - T_m)^2}{T_m} \\
= \;& \frac{(T_m - T)}{T_m} H^{l-s}(T_m) - C_p^{l-s}\frac{(T - T_m)^2}{T_m}. \qquad (3.12)
\end{aligned}
$$

3.2 Validation and finite-size effect

In this section, we extensively study the method on empirical potentials. Although our method is primarily intended to be used with DFT calculations, empirical potentials enable us to extensively test and study our method using an accurate benchmark (a large cell coexistence simulation). The validation of the method is first demonstrated. Then size effect is studied by gradually reducing the system size to around 100 atoms, which is suitable for DFT calculations.

3.2.1 Validation

We test our method on a relatively large system ($6 \times 6 \times 12$ supercell containing 864 atoms) and a Tantalum embedded atom method (EAM) potential [50]. The melting temperature predicted is compared with the benchmarks, which we obtain by both large-size solid-liquid coexistence method and the free energy method. The excellent agreement demonstrates that our method is valid and that it is capable of computing melting temperature accurately.

To generate starting configurations ($x_{\text{liq}} = 0.5$) for MD simulations, we melt the right half of the bcc Ta lattice by heating it to a very high temperature (about four times the estimated melting temperature), while the left half is fixed at its ideal bcc position. After the right half melts completely, we continue the MD simulation for several thousand steps, and capture different coexisting configurations uniformly from

Table 3.1: Melting properties and comparison with benchmarks.

	this method	free energy method	coexistence method
T_m / K	3325	3370	3340
$\Delta_{s-l}H(T_m)$ / eV	0.348	0.353	
$C_{p,s}$ / $\times 10^{-4}$ eV $\cdot$ K^{-1}	3.49	3.24	
$C_{p,l}$ / $\times 10^{-4}$ eV $\cdot$ K^{-1}	3.88	3.98	

the MD trajectory. Each snapshot, a half-and-half combination of frozen solid and superhot fluid, serves as a starting point for one MD simulation.

NPT MD simulations are carried out to trace the evolution of coexisting systems, as is commonly done (see, e.g., Ref. [6]). Here the thermostat is conducted under the Nosé-Hoover chain formalism [40, 41, 42, 43]. The barostat is realized by adjusting volume every 200 steps according to average pressure. (Although this does not formally generates an isobaric ensemble, we find it effective to change volume smoothly and to avoid the unphysical large oscillation caused by commonly used barostats.) During the first hundred femto-seconds, the temperature difference between the solid and the liquid is eliminated through fast heat transfer. The thermostat quickly turns the whole system to the designed temperatures, while the solid and liquid compositions are still approximately 0.5, as the time scale is too short for any phase transition to occur.

Each MD simulation undergoes either freezing or melting to a pure state. Methods including bond order parameter [51, 52] and atomic displacements are used to distinguish between solid and liquid, and to determine whether a system has completely frozen or melted. We show in Fig. 3.2(a) the evolution of 50 independent MD trajectories at 3325 K, from which we can clearly see phase transitions, as they all end at either a higher (liquid) or lower (solid) enthalpy. The final enthalpy is collected from each trajectory, shown as green dots in Fig. 3.2(b). Enthalpies and heat capacities are fitted for the solid and the liquid state separately, according to Eqs. (3.8) and (3.9). At each temperature, the combined enthalpy of solid and liquid together and its standard error is computed based on binomial distribution, shown as blue bars. Finally, melting temperature is obtained through fitting the relation

between enthalpy and temperature according to Eq. (3.10). As shown in both Table 3.1 and Fig. 3.2(b), the close agreement between the results and the benchmarks strongly suggests that our method is valid.

There is another interesting phenomenon we should note in Fig. 3.2(a). Although we have assumed that a simulation will never go back to coexistence only after it reaches a pure phase, this condition is too strong. Even when the fraction of a certain phase is nonzero but small enough, the two interfaces on its boundaries interact so strongly that they intend to annihilate with each other. According to Fig. 3.2(a), the ultimate fate of an MD simulation (fully liquid or fully solid) is only "undetermined" if its composition is within a certain region, e.g., between -7.0 to -6.9 in Fig. 3.2(a). As soon as it steps outside the region, i.e., the composition of one phase is large enough, this advantage is so large that it will never be overruled. This implies that the range $[x_{\min}, x_{\max}]$ of liquid fraction x where the system truly evolves as a random walk is smaller than $[0, 1]$. To account for this, we introduce one more parameter into Eq. (3.6) when fitting to reflect the *a priori* unknown length $l_x = x_{\max} - x_{\min}$. It is straightforward that we can rewrite Eq. (3.6) as follows, provided that $[x_{\min}, x_{\max}]$ is symmetric, i.e., $x_{\min} + x_{\max} = 1$.

$$\frac{N_{\text{liquid}}}{N_{\text{solid}}} = \exp\left(-\beta G^{l-s} l_x/2\right). \tag{3.13}$$

Observing that the interaction of two interfaces is determined dominantly by the distance d between them, we expect l_x to approach 1 asymptotically as we elongate the cell along the direction perpendicular to the interface, which renders d negligible compared the total length of the cell. We calculate the value of l_x for different length l in cell size $n \times n \times l$. When the length l increases, we find l_x approaches 1 as we expected, shown in Fig. 3.5. This predicted property serves as further proof of the validity of our theory.

We note that although our theory is perfect (i.e., T_m is exact and $l_x = 1$) only when the system size is large enough, the accurate calculation of melting temperature does not necessarily require such large size. Take the study in Fig. 3.5 as an example.

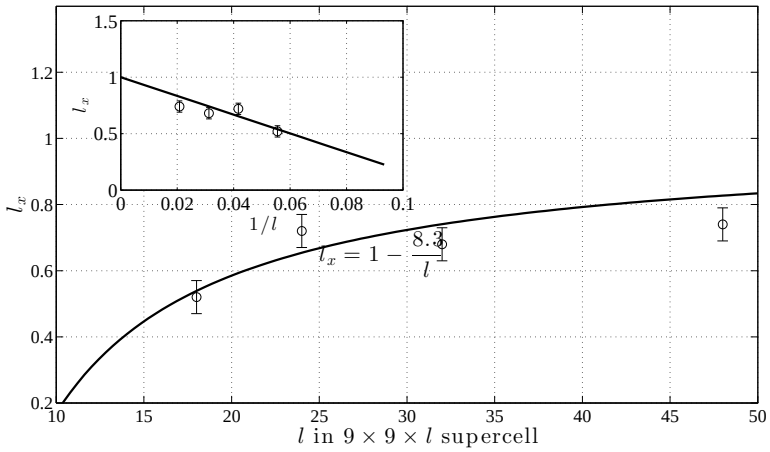

Figure 3.5: l_x as a function of cell length l in supercell size $9 \times 9 \times l$. We calculate l_x on $l = 18, 24, 32,$ and 48. The value of l_x approaches 1 asymptotically as l increases. The curve, which is a function of l^{-1}, is fitted to show the asymptote. In the inserted small plot, the data points are fitted to a line $l_x = 1 - d/l$.

T_m is calculated as 3306 K for both $l = 18$ and 48, though l_x is as different as 0.52 and 0.73, respectively. Melting temperature calculations are accurate even on small system sizes, as we will show in the next section.

3.2.2 Finite-size effect

After we demonstrate that our method is valid in the large system limit, we gradually reduce the system size down to around 100 atoms, a size suitable for DFT calculations. The size effect is studied systematically in this section. The three dimensional space is catalogued into two groups, i.e., the two dimensions in parallel to the interface and the last dimension perpendicular to the interface. The contribution of these two factors are treated separately. We find that the error of melting temperature is still within 100 K even if the supercell size is reduced to $3 \times 3 \times 6$ (108 atoms), which is appropriate for DFT MD calculations.

We first study the directions parallel to the interface plane. As the box size becomes smaller in these two directions, the periodic constraints exert more impact on both phases, especially on the liquid, since the correlation length is truncated by the box vectors. Therefore the calculated melting temperature starts to deviate from

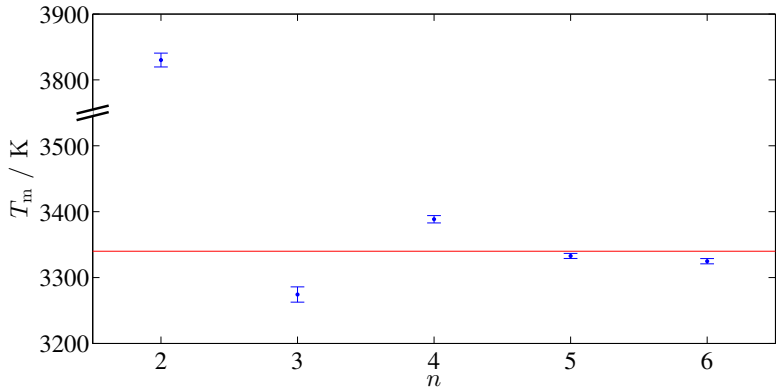

Figure 3.6: Finite-size effect caused by system size n in $n \times n \times l$. Melting temperatures are calculated on $n \times n \times 12$ supercells with n ranging from 2 to 6, following the same scheme described in Sec. 3.2.1. We find that melting temperature calculations are still correct for n down to 3.

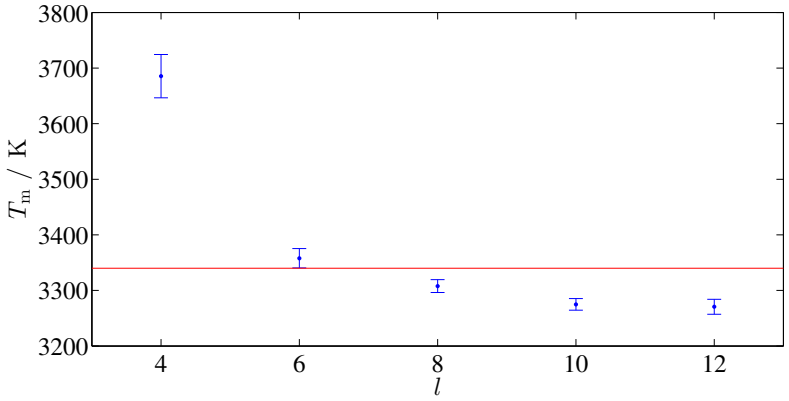

Figure 3.7: Finite-size effect caused by system size l in $n \times n \times l$. Melting temperatures are calculated on $3 \times 3 \times l$ supercells with l from 12 down to 4, We find that melting temperature is still accurate even for a system size as small as $3 \times 3 \times 6$.

the true value. We decrease supercell sizes ($n \times n \times 12$) from $n = 6$ down to 2, and calculate melting temperature for each size, following the same recipe. The size dependence of melting temperature is shown and compared in Fig. 3.6. We find that even for a system size as small as $n = 3$, the finite size effect is still negligible.

We then study the size effect along the direction perpendicular to the interface. As we reduce the vector along this direction, the interaction among interfaces becomes stronger, either attracting or repelling each other and thus biasing the result. We gradually decrease l from 12 to 4. n is set to 3, because it is small enough and it still leads to the correct melting temperature, according to the analysis in the previous

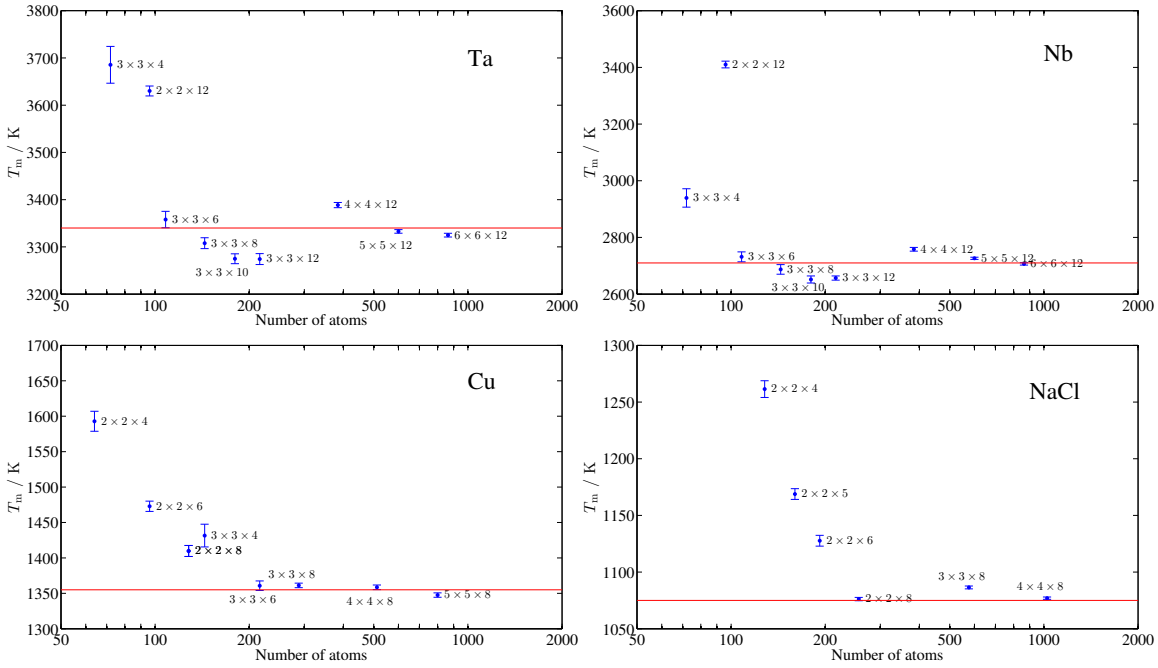

Figure 3.8: Various tests on different materials to study the finite-size effect on melting temperature calculations. Tests are conducted on bcc tantalum, niobium, fcc copper, and ionic sodium chloride. These tests suggests that if we perform calculations with around 100-200 atoms, we are likely to achieve an accuracy of 100 K in melting temperature.

paragraph. We find that the error is still small even for $3 \times 3 \times 6$, as shown in Fig. 3.7.

3.2.3 More tests

Employing empirical potentials, we test the method on different materials, including bcc Niobium[53], fcc copper [5], and ionic material sodium chloride [32]. For each material, we study the finite-size effect caused by system size $n \times n \times l$. The melting temperatures calculated are presented in Fig. 3.8. For super-cells with $n : n : l = 1 : 1 : 2$ (so the box size is approximately $a \times a \times 2a$), we summarize the finite-size error in Fig. 3.9. When the system size is large, the excellent agreement with the benchmarks serves as strong evidence of the reliability of our method. In order to achieve the accuracy within 100 K in melting temperature calculation, we find that it is usually sufficient if the system size is larger than 10 Å and if it contains

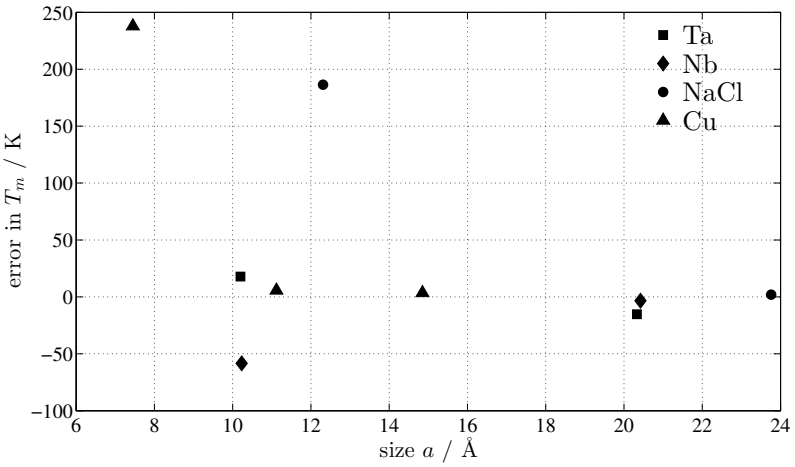

Figure 3.9: The impact from box size $a \times a \times 2a$ on the error of melting temperature calculation. When the size is larger than 10 Å, an accuracy of 100 K in T_m is usually guaranteed, though for ionic materials it is relatively less accurate due probably to the long-distance Coulomb interaction.

more than 100 atoms. This property strongly supports our claim that this method can be applied to DFT calculations.

3.3 Applications

3.3.1 Tantalum at ambient pressure

As a simple example, we first apply our method to the melting temperature calculation of Ta at ambient pressure.

The simulations are performed on a $3 \times 3 \times 6$ bcc supercell containing 108 atoms. All electronic structures are calculated by the Vienna *Ab-initio* Simulation Package (VASP) [35, 36, 54], with the projector-augmented-wave (PAW) [37] implementation and the generalized gradient approximation (GGA) for exchange-correlation energy, in the form known as Perdew-Burke-Ernzerhof (PBE) [39]. Both the valence $6s$, $5d$ and inner core $5p$ electrons (denoted as PBE-core) are included. The electronic temperature is accounted for by imposing Fermi distribution of the electrons on the energy level density of states so it is consistent with the ionic temperature. The plane wave energy cutoff is set to 224 eV and further increased to 500 eV for pressure

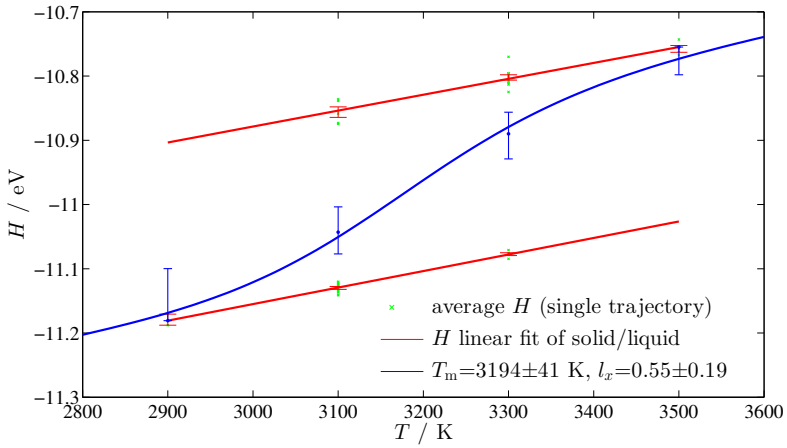

Figure 3.10: The melting properties fitted according to Eqs. (3.7) to (3.10). All calculations are based on PBE-core pseudo-potential.

Table 3.2: Melting properties and comparison with benchmarks.

	this method	experiment
T_m / K	3200	3258
$\Delta_{s-l}H(T_m)$ / eV	0.274	0.379
$C_{p,s}$ / $\times 10^{-4}$ eV $\cdot$ K^{-1}	2.57	4.34
$C_{p,l}$ / $\times 10^{-4}$ eV $\cdot$ K^{-1}	2.52	4.57

correction. A special k-point (0.00 0.25 0.25) is used throughout the calculations. To estimate the error of using this single k-point, we compute its difference to fully converged value on randomly chosen configurations including both solid and liquid. The root mean square error is less than 1 meV/atom.

As shown in Fig. 3.10 and Table 3.2, the melting temperature calculated is 3200 K, only ∼60 K lower than the experiment. This magnitude of error is consistent with our previous size-effect study in Sec. 3.2.2. It is interesting that, in contrast, the calculated heat of fusion and heat capacity (as shown in Table 3.2) differ more significantly from the experiment. These observations are not contradictory. First, finite size effects could introduce a similar bias in the free energies of both the solid and the liquid phases, so that such bias would manifest itself in phase-specific quantities but would only have a second-order effect on the melting point. Second, although the argument of error cancellation between phases is not applicable to the heat of fusion, another possible error cancellation mechanism is between entropy and enthalpy, as

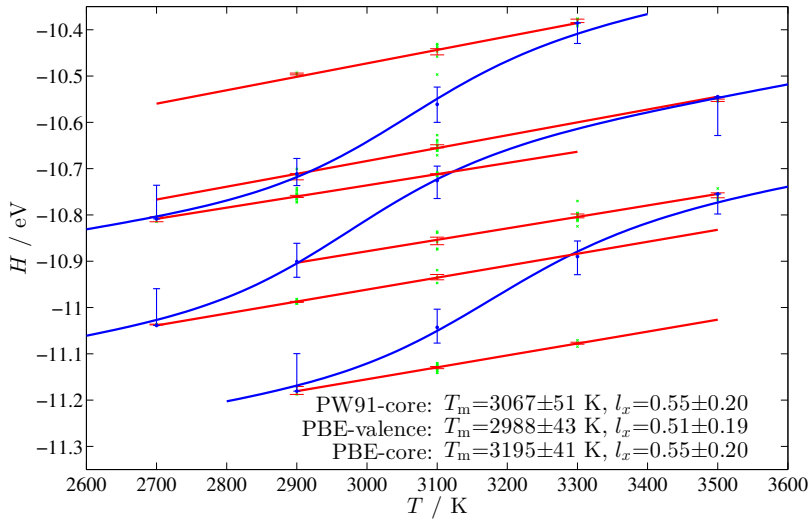

Figure 3.11: Comparison of PBE-core, PBE-valence, and PW91-core, from bottom to top. The latter two are shifted vertically for clarity.

these two quantities tend to change in concert but affect the free energy in opposite ways. Periodic boundary conditions cause the long-range pair-correlation of the liquid to exhibit some solid-like character. This could lead to a larger reduction in both the entropy and the enthalpy of the liquid phase relative to the solid phase. Further study on finite-size effects would be useful to confirm this and could suggest approaches to include finite-size corrections to the current method.

We evaluate the importance of the core $5p$ electrons by freezing them in electronic structure calculations (denoted as PBE-valence). As shown in Table 3.3 and Fig. 3.11, the new PBE valence-only pseudo-potential reduces the calculated melting temperature and worsens the results. This necessity of $5p$ core electrons is consistent with previous findings [55].

We also test the effect of exchange-correlation functionals by changing it to the Perdew-Wang 1991 (PW91) form [56] (denoted as PW91-core). As summarized in Table 3.3 and Fig. 3.11, it also reduces the calculated melting temperature and worsens the results. This small discrepancy is not strange, since there has been evidence showing the differences between PBE and PW91, although they are regarded as almost identical GGA functionals most of the time. Our results indicate that PBE is a better exchange-correlation functional than PW91 in the case of Tantalum

Table 3.3: Comparison of PBE-core, PW91-core and PBE-valence.

	PBE core	PBE valence	PW91 core	experiment
T_m / K	3200	2990	3070	3258
$\Delta\mu_\beta - \Delta\mu_\alpha$ ($\lambda = 0, 1$) / meV	-	$-2.5, -6.4$	$-6.8, -7.3$	-

melting.

The impact of PW91-core and PBE-valence can be quantified in the following way. At the melting temperature, the free energy difference is zero, i.e.,

$$\Delta\mu = \mu_{\text{liquid}} - \mu_{\text{solid}} = 0. \tag{3.14}$$

We employ the thermodynamic integration method to estimate the impact PW91-core and PBE-valence have on the free energy difference $\Delta\mu$:

$$\mu^\beta = \mu^\alpha + \frac{1}{N}\int_0^1 \left\langle H_\beta - H_\alpha \right\rangle_{H_\lambda} \mathrm{d}\lambda, \tag{3.15}$$

where β is PW91-core or PBE-valence, α is PBE-core and

$$H_\lambda = (1-\lambda)H_\alpha + \lambda H_\beta. \tag{3.16}$$

The integral is evaluated only at $\lambda = 0$ (PBE-core) and 1 (PW91-core or PBE-valence). Snapshots of pure solid and liquid are chosen randomly from MD trajectories of $\lambda = 0$ and 1, and the energy differences $H_\beta - H_\alpha$ are calculated on them. As summarized in Table 3.3, PW91-core and PBE-valence stabilize liquid phase by 7 and 4 meV, respectively. Over-stabilized liquid results in a lower melting temperature, and thus qualitatively explains the melting temperature trend predicted.

Similar to the procedure we have employed in Fig. 3.8, the traditional coexistence method could serve as a benchmark to judge the quality of our calculation. However, such large-scale first-principles MD is computationally prohibitive. Here we perform such a check only on the relatively "less expensive" PBE-valence pseudo-potential. A $6 \times 6 \times 12$ supercell (864 atoms) containing solid and liquid coexistence is employed

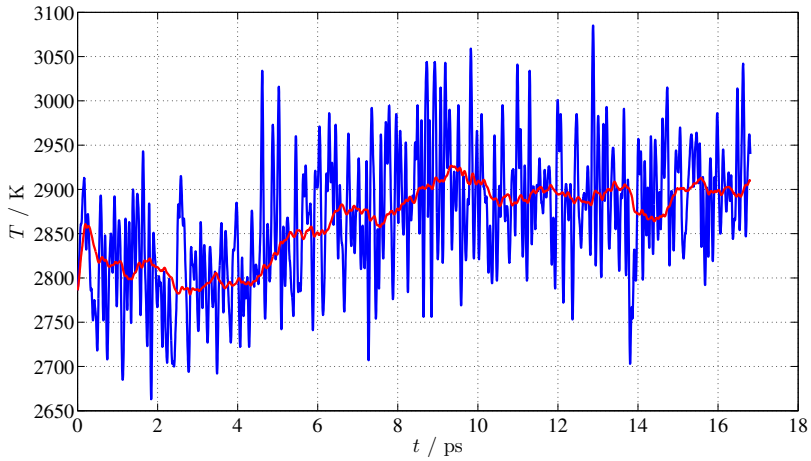

Figure 3.12: NVE MD simulation of solid-liquid coexistence with 864 Ta atoms.

in NVE MD. As shown in Fig. 3.12, the melting temperature is around 2900 K, in close agreement with the corresponding small-size coexistence calculation (2990 K), thus further confirming the reliability of our method.

3.3.2 Sodium phase diagram under high pressure

A prototypical simple metal at ambient conditions, sodium exhibits unexpected complexity under high pressure. One typical example is the so-called "reentrant" behavior, i.e., the melting curve of sodium reaches a maximum around 1000 K at ∼30 GPa followed by a pressure-induced drop, which extends to nearly room temperature at ∼120 GPa and over the stability regions of three solid phases [57]. There have been computational evidences supporting the experimental observation. Raty *et al.* [11] employed the fast-heating method and obtained a melting curve close to the experiments. Eshet *et al.* [58] used a neural-network method based on DFT and calculated a melting curve through the free energy method. Despite their successful capture of the reentrant behavior, the detailed melting points in these two articles are nevertheless quite different. The possible reason could be either the overheating problem in the former method, or the inaccuracy brought in by the neural-network method of the latter. Our small-size coexistence method provides an independent way to corroborate either one of these results.

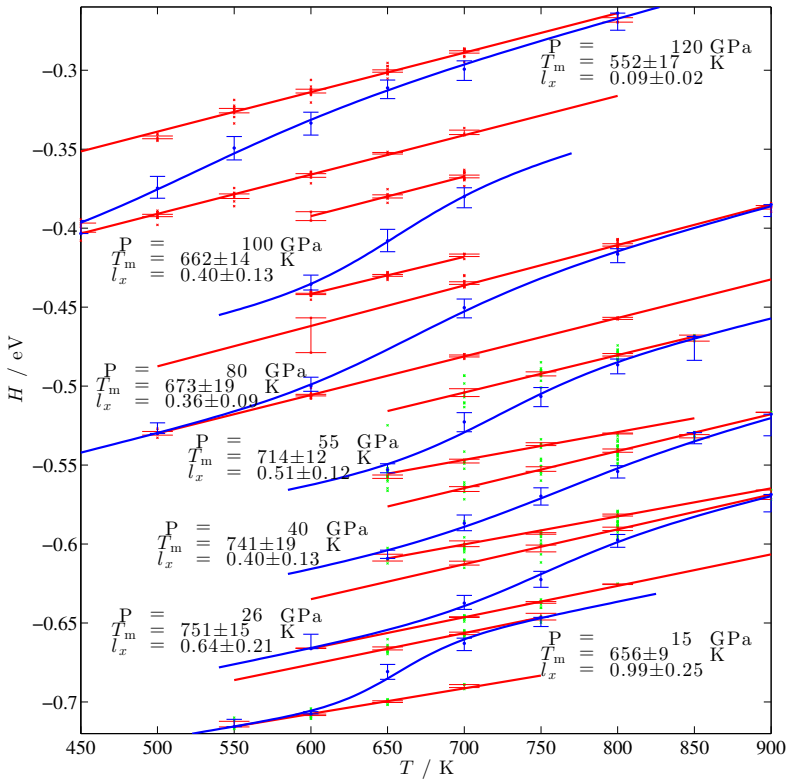

Figure 3.13: The melting temperatures of bcc and fcc Na up to 120 GPa fitted according to Eqs. (3.7) to (3.10).

Table 3.4: Melting temperature and volume change upon melting at different pressures.

P / GPa	15	26	40	55
T_m / K	657±8	750±16	742±17	716±12
ΔV^{l-s} / Å^3	0.048	0.029	-0.005	-0.023

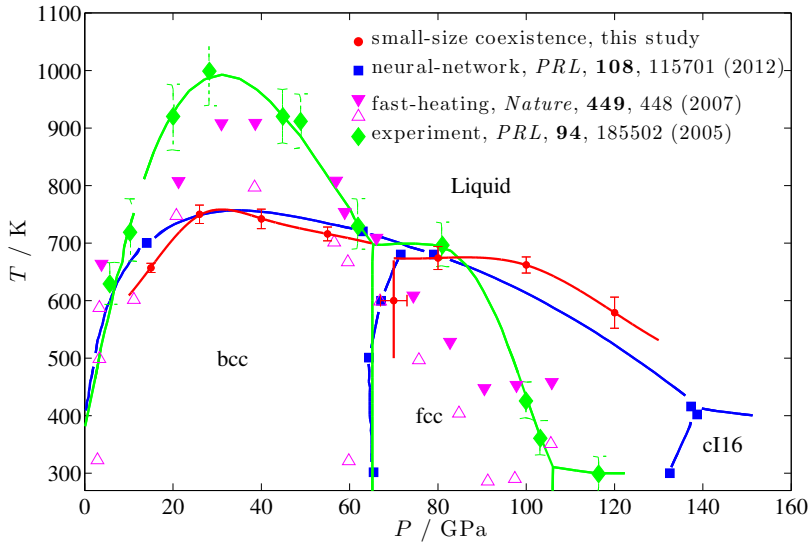

Figure 3.14: Comparison of our results with other theoretical and experimental studies. Our melting temperatures at 20-50 GPa are presented as red dots. Green diamonds are experimental results from Ref. [57]. Purple triangles are melting temperatures by fast-heating method in Ref. [11]. Blue squares are melting temperatures by empirical potential in Ref. [58].

The simulations are performed on $3 \times 3 \times 6$ bcc supercell containing 108 atoms and $3 \times 3 \times 5$ fcc supercell containing 180 atoms. All electronic structures are calculated by the Vienna *Ab-initio* Simulation Package (VASP) [35, 36, 54], with the projector-augmented-wave (PAW) [37] implementation and the generalized gradient approximation (GGA) for exchange-correlation energy, in the form known as Perdew-Burke-Ernzerhof (PBE) [39]. Both the valence $3s$ and inner core $2p$ electrons are included. The electronic temperature is accounted for by imposing Fermi distribution of the electrons on the energy level density of states so it is consistent with the ionic temperature. The plane wave energy cutoff is set to 260 eV and it is further increased to 500 eV for pressure correction. A special k-point (0.00 0.25 0.25) is used throughout the calculations. To estimate the error of using this single k-point, we compute its difference to fully converged value on randomly chosen configurations including both solid and liquid. The root mean square error is less than 1 meV/atom.

The calculated melting temperatures under various pressures are shown in Fig. 3.13 and Table 3.4. In the bcc region, we successfully capture the reentrant point

near (750 K, 40 GPa). Beyond this point, T_{m} starts to drop, and the specific volume change of melting, $\Delta V^{l-s} \propto \mathrm{d}T_{\mathrm{m}}/\,\mathrm{d}P$, turns from positive to negative, in agreement with the decrease of T_{m}. In the fcc region, the melting temperature keeps dropping as the pressure increases. The phase transition between the two solids, bcc and fcc, are calculated using the free energy method. We employ the quasi-harmonic approximation and thermodynamic integration methods to calculate the free energies of the two phases. The phase transition point is located as the intersection of the two free energy curves.

Our calculations agree very well with the result reported in Ref. [58], while the melting temperatures are still significantly lower than results from the fast heating method [11], as summarized in Fig. 3.14. Our results suggest that the neural network method in Ref. [58] successfully mimics the interactions as comparable to DFT accuracy, while the over-heating issue, though relatively small, is still limiting the accuracy of the fast heating method employed in Ref. [11]. To further verify our statement, we perform benchmarking through very expensive large-size coexistence simulation (with 864 Na atoms). As Fig. 3.15 demonstrates, the melting temperature is around 750 K at 26 GPa, thus corroborating the reliability of our calculations. Although the melting temperatures we compute, along with Ref. [58], are significantly lower than experiments, the good agreement with large-size coexistence calculations points to DFT errors, rather than a flaw of our method.

Our method's capability of obtaining melting temperature directly from DFT exhibits its potential to predict phase diagrams. Our melting curve in the bcc solid region, to the best of our knowledge, serves as the first directly first-principles and hysteresis-free computational evidence for the reentrant point of sodium.

3.3.3 NaCl at ambient pressure

After giving two examples on metals, we choose sodium chloride, an ionic material, as our last example. For a long time, melting temperature calculations of ionic crystals were limited to only empirical potentials, probably due to the high expense

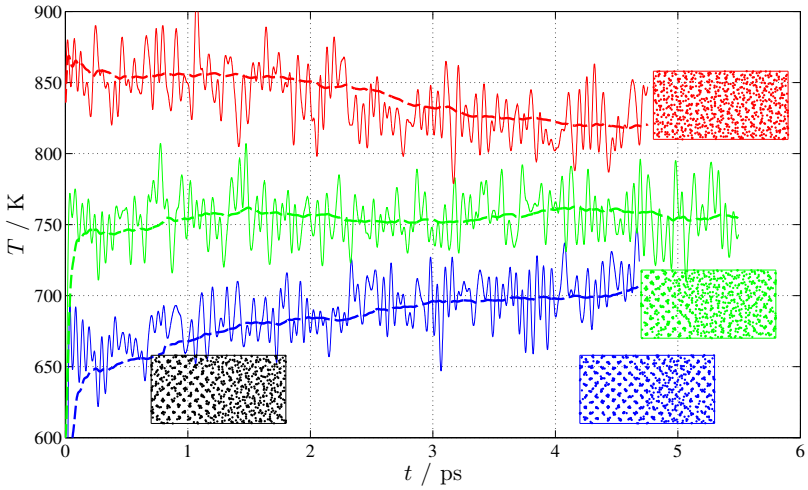

Figure 3.15: Traditional large scale coexistence method (NVE) at different E. Systems with different E are shown in different color. We plot in this figure the temperature evolution over time. Broken lines are time averages so they are more stable and clearer. Atomic configurations are included to help understand the results. The solid part has clear ordered patterns while the liquid part does not. All starting from solid-liquid coexisting configurations (black), only the system with proper E (green) remains in stabilized coexistence. A system with too high E will completely melt (red) and *vice versa* (blue). These tests suggest the melting temperature is around 750 K.

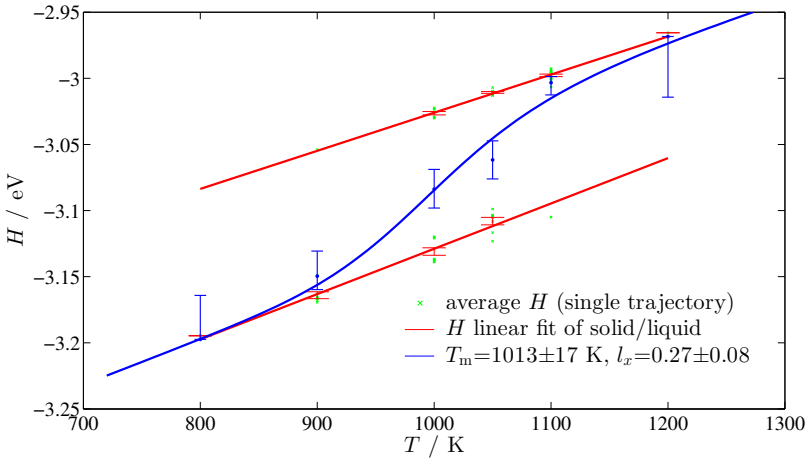

Figure 3.16: The melting properties of NaCl fitted according to Eqs. (3.7) to (3.10).

for DFT correction by thermodynamic integration, as the corresponding high-quality empirical potentials are difficult to find. Recent development of computer power has made possible progress on direct large-scale coexistence simulations of Magnesium Oxide [10] and Lithium Hydride. [9]. However, these calculations are "extremely computationally intensive". Employing the "Z-method", Belonoshko *et al.* have also successfully calculated melting temperature for Magnesium Oxide [13].

The simulation techniques are similar to those described in previous sections. We use a $2 \times 2 \times 4$ supercell containing 64 Na and 64 Cl atoms. Electronic structure calculations are performed by VASP PAW-PBE. Only valence electrons are included, i.e., the $3s$ electron for Sodium and $3s$, $3p$ electrons for Chlorine. Electronic temperature is accounted for by a Fermi distribution. The energy cutoff is 280 eV and only Γ-point is used throughout the calculation. The error caused by using only Γ-point is less than 0.6 meV/atom.

As shown in Fig. 3.16, the melting temperature is 1016 K, which agrees well with the experimental value, 1074 K.

3.4 Discussions

3.4.1 Advantages: robustness, accuracy, speed, etc.

- Robustness and accuracy

  The method we developed is based on formal theoretical grounds, derived in Sec. 3.1, and its reliability is further strengthened by the excellent agreement with benchmarks, shown in Fig. 3.8, especially when the system size is large. Various tests show that finite size effects are usually small and acceptable when the system size is larger than 10 Å and when it contains more than 100 atoms, a size manageable by DFT calculations. Our DFT examples demonstrate that our method is robust, efficient, and applicable to a wide class of materials.

- Speed

  To calculate a melting temperature, we usually need 30-60 MD simulations,

Table 3.5: Computational costs of our method and traditional coexistence approach. (Unit: $\times 10^3$ cpu hours on the Stampede cluster at TACC.)

	traditional coexistence		our method
	single trajectory	total	total
Ta, PBE-valence	150[a]	~ 500	30[b]
Na, P=26 GPa	42, 48 and 35[c]	125	26[d]

[a] shown in Fig. 3.12.
[b] shown in Fig. 3.11 and Table 3.3.
[c] shown in Fig. 3.15, colored in blue, green, and red, respectively.
[d] shown in Fig. 3.13 and Table 3.4.

each with an average length of 10-20 ps. Overall, our method saves significant computational costs compared to the traditional large-scale coexistence method. We list and compare in Table 3.5 the timings of several DFT examples we present in this article. In terms of total costs, our method is less expensive by approximately one order of magnitude. In addition, our method is inherently parallelizable, as we can run the whole set of MD simulations simultaneously. Therefore it takes us the time of running only one single MD trajectory to finish a melting temperature calculation, if we have plenty of computer resources. In contrast, one usually needs to perform, step by step, a long-time (usually more than 10 ps) MD simulation on a large-size system in traditional coexistence method, which usually takes several months.

- flexibility

  A distinguishing feature of this method is its ability to systematically improve melting point estimate if more calculations are performed. This is an inherent property of the statistical method. When more computational resources become available, the method can afford more statistical sampling, which helps reduce sampling error and increase accuracy. Meanwhile, the finite size error can also be systematically reduced if a larger cell size is employed.

It is interesting to compare our approach to the two-phase thermodynamics method, which calculates the entropies and free energies of liquids by partitioning the density of states (DOS) into two parts, i.e., the solid-like Debye-model DOS and the gas-

like hard-sphere DOS. This approach has been successfully applied to a wide variety of substances, including water [26] and many organic compounds [25]. Indeed, this method is surprisingly fast, since it only requires a MD simulation of ~ 20 ps. However, the methods should be compared, not only in terms of computational costs, but also in terms of accuracy and their ability to converge to the correct answer as computational effort is increased. The two-phase thermodynamics approach relies on the assumption that the partitioning of DOS into two phases is always valid, which is not necessarily true. In addition, the harmonic approximation used for entropy calculations would be problematic at high temperatures, when anharmonic effect becomes significant. Due to these approximations, the two-phase thermodynamics method tends to underestimate the excess entropy by 5% [26]. Although small, this error is detrimental to melting temperature calculations. For instance, we estimate the error to be 40-60 meV in free energy and $\sim$ 500 K in melting temperature if the two-phase thermodynamics method is applied to the case of liquid-state copper, which we have studied extensively and achieved an accuracy of 100 K in melting temperature by DFT and particle insertion method. Therefore, we conclude that our approach nicely fills the gap between the two phase thermodynamics method (at one extreme of the accuracy/cost trade-off) and methods based on large-scale coexistence (at the other extreme of the accuracy/cost trade-off). Our small-cell coexistence approach is immune to such problems. Its uncertainties only arise from finite size effects and statistical sampling, both of which can be systematically reduced by increasing computational resources. In contrast, the two-phase thermodynamic approach is not systematically improvable, because the partitioning and harmonic approximations are central to its convenient implementation.

3.4.2 Disadvantages: finite-size error, slow kinetics, and configurational entropy

- Finite-size error

  As discussed in Secs. 3.2.2 and 3.2.3, this method is subject to finite-size errors,

i.e., about 100 K in melting temperature for a system size of 100-200 atoms. Although this seems to be a major disadvantage of our method compared to others, we note that the finite-size effect is a universal problem persisting in almost all melting temperature prediction methods. (The large coexistence method is an exception, but it is nearly infeasible due to its high cost.) For example, the fast-heating method and Z-method usually use a comparable system size, so they suffer from similar size effect as well, in addition to the hysteresis problem. As another example, let us consider the free energy method based on empirical reference potentials followed by DFT corrections. One might argue that the finite-size error can be completely eliminated if convergence is achieved on empirical potentials with respect to system size. But this is not exactly true. As DFT corrections are usually performed on small-size systems, the final free energy calculated by this method is, strictly speaking, a DFT free energy on a small system plus a finite-size correction by the empirical potential. One can never guarantee that the finite size effect from an empirical potential will be the same (or even similar) to that of DFT. Therefore the free energy method is also subject to finite-size errors.

We can approximately correct the finite-size errors by extrapolating the convergence behavior of both phases. The quasi-harmonic approximation provides a quick approach to estimate the correction in the solid phase, while radial distribution function [61] gives insight into the entropy of the liquid phase. Preliminary study shows promising results and sheds light on the improvement of the current method, making it more accurate and efficient, as we can further reduce the system size.

Another problem of finite size effect is that the system could be stabilized in a wrong phase, for either solid or liquid. This problem occurs when there is a competing alternative near the desired phase in the phase diagram. In reality, this competing phase is relatively less stable, but the finite-size effect could revert the stability relation of them, so that the simulation ends in a wrong

structure. Therefore, we recommend that one should check the final structure of a MD trajectory to make sure that it is in the desired solid or liquid phase.

- Slow kinetics

  Although the method is robust in melting temperature prediction, it also inherits the disadvantage of MD simulations, unfortunately. For example, it suffers from the well-known rare event problem. This renders it problematic for the following circumstances:

  1. If the crystal structure of the solid is complex, the liquid half may fail to find the right crystal structure when solidifying, and it may form defected solid structures. Fortunately, this possibility is readily detectable in the simulations.
  2. If there is more than one solid configuration and the stability is based on certain distribution in phase space, e.g., for some alloys, MD will fail to explore all configurations in limited computer time and find kinetically-favored metastable structure.
  3. If the elemental concentrations of the solid and the liquid are different at the equilibrium, MD is not capable of redistributing different atoms in each phase sufficiently fast. In systems where this occurs, the method can still be used to find melting points at compositions where congruent melting occurs. Free energy integration (on fairly small simulation cells) can be used to find the solidus and liquidus at other compositions, using congruent melting points as free energy references.

  However, we note here that these problems are also common to other methods, e.g., in the traditional large scale coexistence method.

- Configurational entropy

  For a solid, a particular arrangement of atoms on lattice sites is called a *configuration*. Configurational entropy is common in materials. For example, in

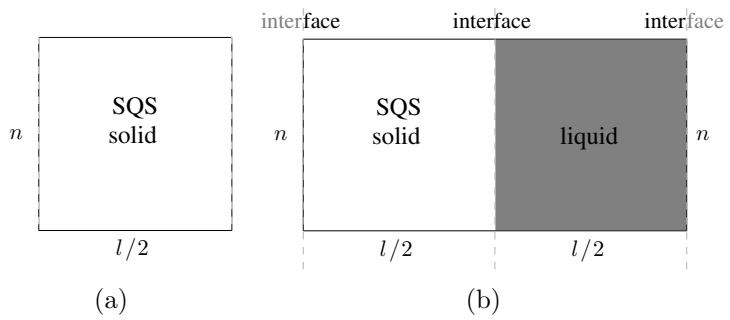

Figure 3.17: Difference between (a) pure-solid and (b) solid-liquid coexistence SQS's. A good SQS representation generated in a periodic solid is no longer valid in solid-liquid coexistence.

a multicomponent system (e.g., metal alloy), the number of accessible configurations can be enormous as different kinds of atoms sit on different types of lattice sites. The probability of visiting each configuration is proportional to the Boltzmann weight of its free energy.

The solid portion in a coexisting cell needs to represent this overall distribution on the accessible configurations. At high temperatures, the special quasirandom structure (SQS), which provides a efficient representation of a completely disordered state, is an effective approach. This strategy is heavily employed in the study presented in Chapter 5, and the melting temperatures calculated are in good agreement with experiments. Despite its success, we note another minor problem, as illustrated in Fig. 3.4.2: a SQS representation in a periodic solid (which is easy to generate) is not equivalent to a SQS in solid-liquid coexistence (which is difficult to generate), due to the broken symmetry and the presence of the interface. The latter SQS (low symmetry, too many types of lattice sites and clusters) requires a large system size, hence (1) the SQS is difficult to generate and (2) the system size is too large to apply in small-cell coexistence. In practice, we use the former SQS to represent the latter. We plan to further investigate into this problem.

3.4.3 Pulay stress

The Pulay stress is an error that occurs in the stress tensor when using density functional theory. It occurs when trying to relax the volume of a crystal using a constant basis set, or equivalently when trying to calculate the pressure. In VASP, the Pulay stress arises from the fact that the planewave basis set is not complete with respect to changes of the volume. The volume always tends to contract, in order to achieve a denser (close to complete) basis set. Thus, unless absolute convergence with respect to the basis set has been achieved, the diagonal components of the stress tensor are incorrect.

"Absolute convergence" is usually achieved by setting the precision tag to *high* (PREC=high, or using a large planewave energy cutoff), which will significantly increase the computer cost and is usually not affordable in MD. The *normal* precision usually has negligible impact on the description of atomic interactions. The missing bases mostly contribute to the spikes near the nuclei, and thus barely affect the interatomic bonding region, where wavefunctions are smooth enough to be described by the low-frequency planewaves. With precision set to normal, the Pulay stress is up to 30 kbar, especially for non-metal elements such as nitrogen, oxygen, and carbon.

Small-cell coexistence MD is usually carried out with the normal precision. The Pulay stress associated with this setting can result in the wrong pressure and hence wrong volume. This error may translate into a considerable amount of error in the calculation of melting temperature. According to the Clausius-Clapeyron relation,

$$\frac{\mathrm{d}T_m}{\mathrm{d}P} = \frac{T_m \Delta V}{\Delta H}, \tag{3.17}$$

where ΔV is volume change upon melting, and ΔH is heat of fusion. Assuming $T_m = 2000$ K, $\Delta V = 0.1 \times V_s = 1$ Å^3 [62], $\Delta H = 0.2$ eV, $\Delta P = 30$ kbar, we have

$$\Delta T_m = 190 \text{ K}.$$

We therefore emphasize the importance of including Pulay stress in pressure calcula-

tion. Furthermore, we note that the Pulay stress varies as the composition changes in multicomponent systems, and hence an updated Pulay stress is necessary when working on a new composition.

3.5 Code development

We are in the process of fully automating the process of small-cell coexistence melting point calculation and implementing it into a computer code which will be capable to predict melting point from input of (i) solid structure and (ii) estimated melting point (optional). The code consists of the following steps.

1. Find lattice parameter of solid near estimated melting point. Find density of liquid (and corresponding "lattice parameter"). Build a supercell with a properly chosen lattice parameter (usually the average of solid and liquid, to minimize mismatch).

2. Generate solid-liquid coexistence by melting half of the solid supercell.

3. Choose best approach to sample solid-liquid distributions at various T, based on current knowledge of melting temperature.

4. Starting from coexistence, run NPT molecular dynamics to determine the final phase. (This part is already automated.)

5. Fit a melting point. Determine whether or not more sampling is needed. If yes, go to step 3.

We plan to distribute the code "Solid and Liquid in Ultra Small Coexistence with Hovering Interfaces (SLUSCHI)" in December 2014.

3.6 Conclusions

To summarize, we have proposed an efficient and accurate method of calculating the melting temperature of materials. This method is based on the statistical anal-

ysis of small-size coexistence MD simulations, so it circumvents both the hysteresis overheating problem in small system size and the prohibitive computer cost in traditional coexistence method. Using empirical potentials, we present the validation of the method and systematically study the finite-size effect on the melting temperatures calculated. Through the DFT examples, we demonstrate the capability and flexibility of the method in its practical applications.

Chapter 4

Melting properties of lanthanum zirconate ($La_2Zr_2O_7$)

Lanthanum zirconate is being investigated for a wide range of applications, including solid oxide fuel cell electrodes [63, 64], fluorescence screens [65, 66], catalysts [67, 68], and high-temperature superconducting coated conductors [69, 70]. In particular, $La_2Zr_2O_7$ is proposed as a promising thermal-barrier coating (TBC) material [71, 72, 73, 74, 75, 76, 77, 78, 79, 80] to replace the most-commonly used yttria-stabilized zirconia (YSZ) for the following reasons: (i) $La_2Zr_2O_7$ coating has high phase stability against thermal treatment, and thus it is capable of functioning under higher temperatures, far beyond the limited operation temperature (1200 °C) of YSZ [81]; (ii) $La_2Zr_2O_7$ has a lower thermal conductivity, which provides better thermal insulation for the components from large and prolonged heat loads; (iii) $La_2Zr_2O_7$ has a lower oxygen ion diffusivity (less oxygen-transparent), so it protects the body coat from oxidation. The major drawback of $La_2Zr_2O_7$ as a TBC coating is its small thermal expansion coefficient, which does not match that of the superalloy in the body coat.

The assessment of novel refractory materials, such as lanthanum zirconate, demands the determination of a number of physical, chemical, and mechanical properties. We demonstrate how *ab initio* calculations can be used in conjunction with advanced experimental techniques (synchrotron X-ray diffraction on laser heated aerodynamically levitated samples and thermal analysis above 2000 °C) to provide a more

complete and accurate picture of thermal properties. Our combined computational and experimental investigation determines key material properties, ranging from enthalpy of fusion and melting temperature to thermal expansion and heat capacity. We also investigate the possibility of high-temperature sublattice disordering.

Some properties are more directly obtained via computational means. For instance, the heat of fusion, the heat capacity, and the thermal expansion are straightforward to calculate, but clearly benefit from an experimental verification to ascertain the validity of the modeling assumptions (e.g., stable structure, sources of entropy, and the reliance on density functional theory). These measurements, while simple at low temperature, become challenging above 1500 °C, as considered in this work, because they necessitate development of new experimental techniques and calibration standards. In contrast, other properties are more easily accessible experimentally. The most striking example is the melting point, where computational efforts via *ab initio* methods demand advanced techniques to reduce the computational burden [9, 10, 17, 19, 82, 83, 84, 85]. In this work, the recently proposed small-cell coexistence method makes it feasible to calculate the melting point of a compound with a substantially more complex crystal structure than considered in prior *ab initio* computational studies. Given the challenges associated with these calculations, experimental validation is particularly important. Another important example of computational-experimental complementarity is the determination of the presence of sublattice disordering. While it is difficult to assess the state of order of the oxygen sublattice via X-ray diffraction (due to its small scattering factor), our computations can rather clearly establish the possibility of such a disordering transition, since oxygen diffusion is visible in our simulations. Conversely, disordering on the cation sublattice is not as easily accessible in our simulations but would have been detected experimentally if it were present.

Overall, our results show very good agreement between experimental measurements and their computational counterparts, even in cases reaching the limit of today's computational or experimental methods. This situation supports the validity of our thermodynamic description.

4.1 Methodology

Pyrochlore $La_2Zr_2O_7$ structure has the space group of $Fd\bar{3}m$ that is derived from the fluorite-like arrangement of atoms. The cubic pyrochlore structure of $La_2Zr_2O_7$ has been discussed in detail. [86, 87, 88, 89]. As shown in Fig. 4.1, the La^{3+} ions occupy the special site $16d$ $(1/2, 1/2, 1/2)$ and the Zr^{4+} ions occupy the special site $16c$ $(0, 0, 0)$. The oxygen atoms are located at sites $48f$ $(x, 1/8, 1/8)$ and $8b$ $(3/8, 3/8, 3/8)$, and the oxygen vacancies at $8a$ $(1/8, 1/8, 1/8)$. Table 1 lists the lattice parameter and the value of x from both calculation and experiment. The primitive unit of $La_2Zr_2O_7$ consists of 4 La, 4 Zr, and 14 O atoms. There are 88 atoms in a face-centered cubic (fcc) conventional unit cell. $La_2Zr_2O_7$ is also reported in the defect fluorite ($Fm\bar{3}m$) structure as transitory during radiation damage and from low temperature synthesis. The defect fluorite structure can be derived from pyrochlore by disordering on both cation and anion sublattices.

4.1.1 Computation

We employ first-principles density functional theory [2, 3, 4] to model $La_2Zr_2O_7$. All electronic structures are calculated by the Vienna *Ab-initio* Simulation Package

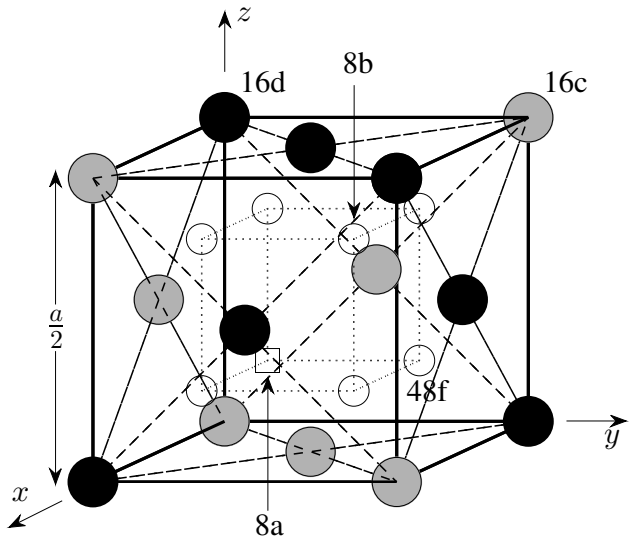

Figure 4.1: Pyrochlore structure of $La_2Zr_2O_7$.

(VASP) [35, 36, 54], with the projector-augmented-wave (PAW) [37] implementation and the generalized gradient approximation (GGA) for exchange-correlation energy, in the form known as Perdew-Burke-Ernzerhof (PBE) [39]. For Lanthanum, the inner core $5s$ and $5p$ electrons are relaxed for electronic structure optimization. The electronic temperature is accounted for by imposing a Fermi distribution of the electrons on the energy level density of states, so it is consistent with the ionic temperature.

First-principles molecular dynamics (MD) techniques are utilized to simulate atomic movements and trajectories of $La_2Zr_2O_7$ in order to compute various properties. Specifically, MD simulations are carried out under a constant number of atoms, pressure, and temperature condition (NPT, isothermal-isobaric ensemble). Here the thermostat is conducted under the Nose-Hoover chain formalism [40, 41, 42, 43]. The barostat is realized by adjusting volume every 200 steps according to average pressure. Although this does not formally generate an isobaric ensemble, this approach has been shown to provide an effective way to change volume smoothly and to avoid the unphysical large oscillation caused by commonly used barostats. The $La_2Zr_2O_7$ pyrochlore structure is taken as a starting point for all MD simulations of the solid phase.

4.1.2 Experiment

Laser melting of $La_2Zr_2O_7$ for diffraction and thermal analysis experiments causes some loss of La, resulting in $La_{1.96}Zr_{2.03}O_7$ stoichiometry, as determined by microprobe analysis. Thermal analysis is performed in sealed tungsten crucibles in Setaram Setsys 2400 instrument modified to enable sample temperature monitoring with spectropyrometer [90, 91]. High temperature X-ray diffraction experiments are performed on an aerodynamic levitator at beamline 11-ID-C at the Advanced Photon Source, Argonne

Table 4.1: Experimental and calculated structures of $La_2Zr_2O_7$.

method	Expt.	PBE	HSE	HF
a(Å)	10.805	10.880	10.833	10.728
x	0.4200	0.4172	0.4171	0.4170

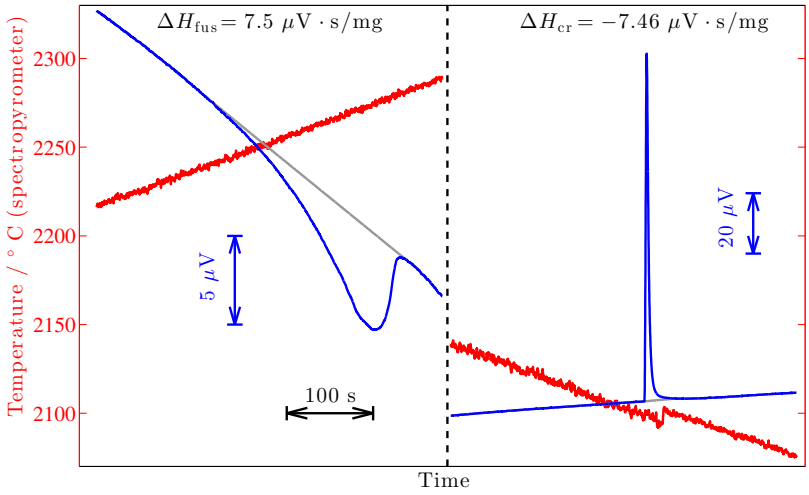

Figure 4.2: Melting and crystallization of $La_{1.96}Zr_{2.03}O_7$ in thermal analyzer at 10 °C/min heating/cooling rate. 150 °C undercooling is evident. Integration of peaks in heat flow (blue trace) on melting and crystallization gives similar values, indicating direct crystallization of pyrochlore phase.

National Laboratory. A detailed description of experimental setups is published elsewhere [92]. Processing of diffraction data is performed with GSAS-II software [93]. Splat quenching of lanthanum zirconate melt is performed at UC Davis using a custom built splittable nozzle aerodynamic levitator with CO_2 laser heating.

4.2 Melting and thermal properties

4.2.1 Fusion enthalpy

Fusion enthalpy is calculated as the enthalpy difference between the solid and the liquid at 2500 K. We perform NPT MD simulation to generate a trajectory for each phase. The enthalpy is evaluated as an average over time during the MD trajectory.

We use a supercell containing 88 atoms (8 $La_2Zr_2O_7$) for the pyrochlore phase. Modeling liquid phase on a periodic cell is subject to a relatively stronger finite-size effect, since the liquid is imposed by the unrealistic periodic boundary condition. So we choose a larger cell with 176 atoms to describe the liquid phase more accurately.

We perform further correction on the data from PBE to a more accurate hybrid functional of Heyd-Scuseria-Ernzerhof (HSE) [94]. For both the pyrochlore and liquid

phases, we compute energy differences between PBE and HSE on randomly chosen snapshots from MD trajectories, and then combine them as a correction on the fusion enthalpy.

The fusion enthalpy is calculated to be 0.26 eV/atom (270 kJ/mol). After HSE correction, it is 0.28 eV/atom (300 kJ/mol). The major error is considered to be the finite-size effect from the liquid phase. Based on a study on different system size (88 atoms versus 176 atoms), the error is estimated to be 0.02 eV/atom (20 kJ/mol).

The first experimental measurement of fusion enthalpy for $La_2Zr_2O_7$ pyrochlore was reported by Radha [79]. The new set of measurements (Fig. 4.2) is performed on laser melted $La_{1.96}Zr_{2.03}O_7$ in sealed tungsten crucibles to prevent carbon contamination from furnace. Uncertainty in experimental measurements of fusion enthalpy by thermal analysis is difficult to evaluate due to the absence of enthalpy calibration standard above Al_2O_3 melting temperature (2054 °C). The value 300 ± 50 kJ/mol can be taken as a conservative evaluation of both sets of experimental measurements.

The close agreement between computation and experiment strongly supports the validity of the results. We find the computational approach relatively easier than its experimental counterpart in determining heat of fusion, when temperature reaches far beyond the Al_2O_3 melting temperature (2054 °C). The enthalpy calibration standard for higher temperature, e.g., Y_2O_3 (2430 °C), would increase the accuracy of fusion enthalpy measurements by commercially available thermal analyzers. We plan to work on it in the next step, using a combined experimental and computational approach.

4.2.2 Melting temperature

We employ our small-size coexistence method to calculate the melting temperatures. The result is shown in Fig. 4.3. The details of this method have been described previously in Section 3.1. The simulations on $La_2Zr_2O_7$ are performed on a $1 \times 1 \times 2$ fcc supercell, which contains 176 atoms and measures approximately $11 \times 11 \times 22$ Å^3. The plane wave energy cutoff is set to 400 eV and is further increased to 500 eV for pressure correction. NPT MD simulations are carried out to trace the evolution of

Table 4.2: HSE correction on melting temperature.

T_m^{PBE}	2420 K
$\Delta\mu^s$	-2.634 eV
$\Delta\mu^l$	-2.610 eV
ΔH^{l-s}	0.28 eV
ΔT_m	210 K
T_m^{HSE}	2630 K

coexisting systems. Only Γ-point is used throughout the calculations. To estimate the error of using this single k-point, we compare it with the fully converged k-point grid and compute the energy difference on randomly chosen configurations from both solid and liquid. The root mean square error is less than 1 meV/atom.

The melting temperature T_m is calculated to be 2420 ± 28 K, as shown in Fig. 4.3. We apply a correction based on the more accurate hybrid functional of HSE. First, free energy correction is made on each phase following the thermodynamic integration method:

$$\mu_\beta = \mu_\alpha + \frac{1}{N}\int_0^1 \left\langle H_\beta - H_\alpha \right\rangle_{H_\lambda} \mathrm{d}\lambda, \tag{4.1}$$

where β is HSE and α is PBE. Due to the high computational cost of HSE, only

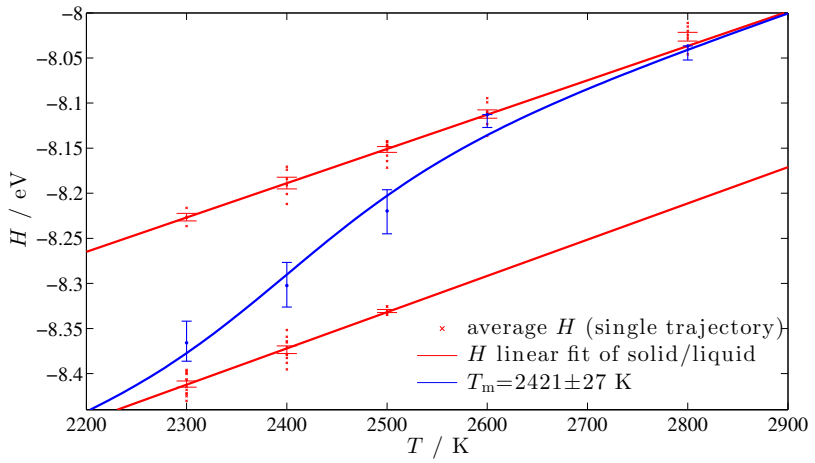

Figure 4.3: The melting temperature of $La_2Zr_2O_7$ fitted according to Eqs. (3.7) to (3.10).

Table 4.3: Comparison with experimental melting temperature.

T (°C)	Reference
2150	this work, PBE
2360	this work, HSE
2260	this work, expt.
2295	Radha (2009) [79]
2340	Lakiza (2005) [95]
2230	Zoz (1978) [96]
2160	Portnoi (1972) [97]
2280	Rouanet (1971) [98]
2250	Lin (1964) [99]

$\lambda = 0$ is used for integration. Then melting temperature correction is evaluated as

$$\Delta T_m = (\Delta\mu^l - \Delta\mu^s) \cdot \frac{T_m}{\Delta H^{l-s}}, \tag{4.2}$$

where $\Delta\mu^{l/s}$ are the corrections in free energies for the liquid and the solid, ΔH^{l-s} is heat of fusion, and ΔT_m is melting temperature correction. Detailed data of the HSE correction on melting temperature are listed in Table 4.2. The melting temperature after HSE correction is 2630 K.

The experiment measures the melting temperature as 2260 °C (2530 K), which lies in the middle of the two theoretical predictions. Our results are in close agreement with others in the literature, as shown in Table 4.3.

Our calculations enable us to identify the factors that contribute to a high melting point in $La_2Zr_2O_7$. It has a large fusion enthalpy of 0.28 eV/atom, which is a major contributor to the high melting point. Pyrochlore phase $La_2Zr_2O_7$ is further stabilized by its high entropy in the following two respects. An interesting behavior of the pyrochlore structure is the formation of soft vibrational modes upon thermal expansion. As shown in Fig. 4.4, thermal expansion not only softens certain zone-center phonon modes, but also creates a new wide double-well feature, which significantly increases the accessible phase space. The high entropy of the solid phase also comes from diffusion of oxygen atoms. As discussed in Section 4.2.3.1, the corresponding barrier is relatively low, so oxygen atoms visit their neighboring vacancies frequently.

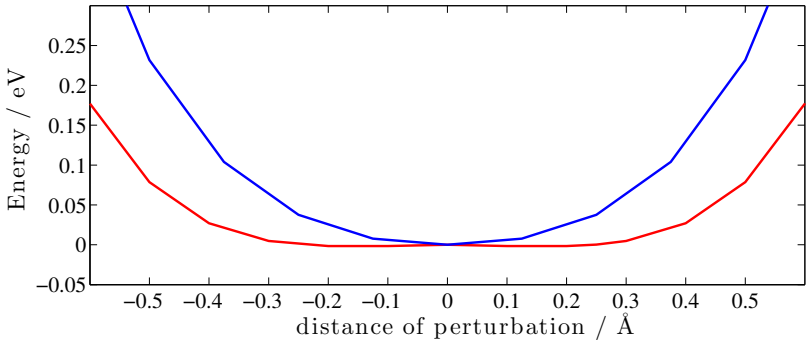

Figure 4.4: Potential energy upon perturbation along a zone-center soft phonon mode predominantly involving La motion along ⟨123⟩ and ⟨110⟩ directions (blue: 0 K; red: 2% thermal expansion). The potential well not only softens, but also forms double-wells (the curvature at the center turns negative after the thermal expansion). This feature significantly increases the accessible phase space, which increases entropy as a result.

The likelihood of forming an oxygen-disordered sublattice greatly increases the configurational entropy, which further stabilizes the solid phase.

4.2.3 Disordering

The susceptibility of the pyrochlore structure to disordering is related to the resistance of these materials to radiation damage. Irradiation effects in zirconate pyrochlores have been studied by both experimental [100, 101, 102, 103] and theoretical [104, 105] studies. These studies explored the possibility of these materials as radionuclide hosts in ceramic waste forms and the likelihood of their formation caused by the reaction between the zircalloy cladding and the fission products of severe nuclear reactor accident scenarios [100]. $Gd_2Zr_2O_7$ undergoes an order-disorder structural transformation at 1550 °C. This disordered defect fluorite structure shows strong resistence to radiation damage, even at extremely high doses. Upon irradiation, $La_2Zr_2O_7$ first undergoes initial disordering of the oxygen sublattice with random occupation of the oxygen vacancies and then random distributions of cations and anions, leading to formation of the disordered fluorite phase [101, 106]. However, this ion-irradiation-induced disordered state is transient and amorphization takes place on further irradiation [107, 101]. Fluorite is also observed to form on crystallization

of amorphous lanthanum zirconate in a wide range of compositions [108]. However, the fluorite phase has never been quenched from high temperature, and it is not clear whether it is stable in bulk at any temperature.

Disordering has a strong impact on thermal performance of TBC materials. The disordering of TBC leads to volume change and hence mismatch between body coat and topcoat, which results in cracking in TBC, a common mode of materials failure. Also, oxygen sublattice disorder determines whether a material is oxygen-transparent. If oxygen atoms can diffuse readily in TBC, the underlying body coat is exposed to the oxygen environment in the heat flux, which rapidly oxidizes the body coat and forms thermally grown oxide (TGO). Irregularly grown TGO exaggerates the strain in the coating, which is a major mechanism of thermal failure.

In our simulations, we find strong evidence that the system undergoes a sublattice disordering transition (on the oxygen sublattice) just before melting. Our results also indicate that disordering of the cation sublattice is unlikely. Synchrotron X-ray diffraction confirms cation ordering in pyrochlore up to complete melting.

The energy scale of the oxygen-sublattice disordering transition is found to be very small, hence the precise nature of the ordering in the solid phase turns out to have little impact on the calculated melting point. We find that disordering on the oxygen sublattice fortunately occurs only close to the melting point, so it will not affect the prospective use of $La_2Zr_2O_7$ as a thermal barrier coating since service temperatures normally do not exceed 2/3 of melting temperature of the material.

4.2.3.1 Oxygen sublattice

We observe oxygen diffusion in MD simulation of pyrochlore lanthanum zirconate, as shown in Fig. 4.5(a), which implies disordering on the oxygen sublattice. Transition state analysis also supports this finding. For oxygen moving to a nearby vacancy, the transition barrier is 0.5 eV (48 kJ), and the energy penalty for the final state after diffusion is only 0.4 eV (39 kJ), as shown in Fig. 4.5(b). At 2500 K, this corresponds to a Boltzmann distribution factor of 0.16, which is further increased to $\sim$1, since each vacancy has six degenerate neighboring oxygen atoms. These two observations

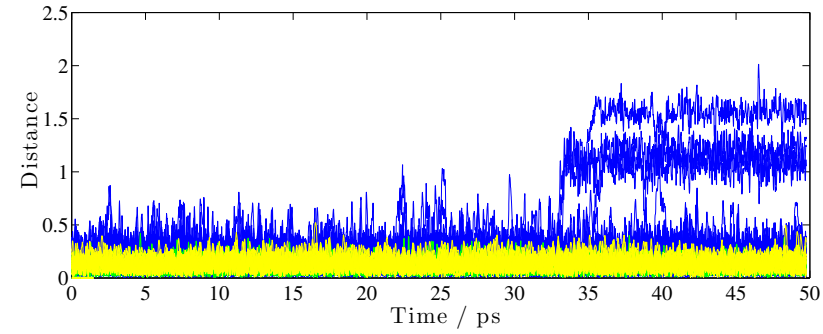

(a)

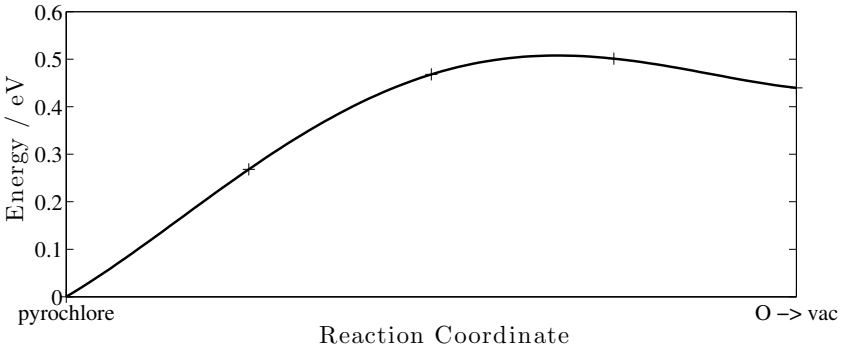

(b)

Figure 4.5: (a) Distance to ideal pyrochlore position during MD simulation of the solid phase at 2500 K. (blue: O; green: Zr; yellow: La.) Distance is normalized so that the nearest neighbor distance between two oxygen atoms is 1. Diffusion is observed on two oxygen atoms near 35 ps. (b) Potential energy diagram based on nudged elastic band (NEB) method [109, 110]. For an oxygen atom moving to its neighboring vacancy, the activation energy is 0.5 eV (48 kJ). The energy of the final state is 0.4 eV (39 kJ) higher than pyrochlore.

strongly suggest disordering on the oxygen sublattice.

A rigorous evaluation of the phase stability requires a cluster expansion [111, 112] in order to capture all important configurational states that contribute to the disordered phase. This would be very difficult to carry out for a complex ionic substance such as $La_2Zr_2O_7$, especially given that the anharmonic effects are likely to be large. Instead, we employ the special quasirandom structure (SQS) approach [113] implemented in the "mcsqs" [114] code in ATAT [115] to estimate the phase stability. At first, a completely random oxygen-vacancy sublattice is studied. But we find most SQS's are unstable. Upon structural optimization, some oxygen atoms move to other lattice sites, which changes the original configuration. In particular, the tetrahedron

center of 4 Zr atoms (called 8a-site) is highly unfavored for the oxygen atom, and the high oxygen concentration at these 8a-sites is the major reason for the instability. Indeed, these sites are vacant in the pyrochlore structure. In response to this phenomenon, we limit the oxygen concentration on these 8a-sites and study a disordered phase as described below.

1. The cations are ordered as in pyrochlore.

2. Oxygen is randomly distributed on 8a-sites, with a concentration of 1/4.

3. Oxygen is randomly distributed on the rest sublattice, with a concentration of 27/28 (so that the chemical composition is $La_2Zr_2O_7$).

We generate a SQS representation of this disordered phase. The SQS is stable. With respect to pyrochlore, its energy is 33 meV/atom (35 kJ/mol $La_2Zr_2O_7$). The entropic free energy at 2500 K is

$$-TS_{\text{fluorite}} = kT \sum n_i \ln x_i / \sum n_i = -32 \text{ meV/atom}.$$

Combining energy and entropy, this disordered phase is of comparable stability as the pyrochlore phase.

The actual disordered phase in reality will populate configurational states according to a Boltzmann distribution, rather than the uniform distribution we assume in the random structure. A Boltzmann distribution will result in the lowest free energy compared to any other distribution, and therefore the free energy we calculate above is the upper limit for the disordered phase. The actual disordered phase in reality will be more stable than the randomly disordered one, which makes it very likely to replace the pyrochlore phase at high temperatures. The fact that energetic and entropic effects are so close suggests that the transition temperature will be close to 2500 K, very near the melting point.

Experimental X-ray diffraction cannot capture signals from oxygen atoms clearly, as they are overwhelmed by signals from heavy La and Zr atoms. However, neutron

Table 4.4: Pair correlation as an order parameter to quantify the randomness of newly formed solid from MD. The values for ordered pyrochlore and completely disordered random fluorite are listed for comparison.

	Zr-Zr	La-La	Zr-La
2300 K	0.36 ± 0.01	0.36 ± 0.01	0.27 ± 0.02
2400 K	0.31 ± 0.02	0.32 ± 0.02	0.37 ± 0.02
2500 K	0.32 ± 0.02	0.32 ± 0.02	0.35 ± 0.04
pyrochlore	0.5	0.5	0
random fluorite	0.25	0.25	0.5

diffraction will clearly capture oxygen atoms, and we plan to work on this aspect in the near future.

4.2.3.2 Cation sublattice

During MD simulation of solid-liquid coexistence, we observe a cation-disordered solid phase when the liquid portion of the supercell solidifies. Although this may serve as evidence for cation disordering, we cannot rule out the possibility that this disordered solid is metastable. When solidifying, the random chaotic liquid portion may not fully optimize and arrange itself to the thermodynamically most favored solid structure, due to the limited length of time (only on the order of 10 picoseconds). It requires a thermodynamic study on this disordered phase to assess its relative phase stability.

The energy of this phase is first extracted from coexistence MD simulations. When solid-liquid coexistence evolves to pure solid phase, we find that, in most cases, half of the supercell is in the cation-disordered phase, while the other half is in the original pyrochlore phase. The energy of this disordered phase is calculated to be 114 meV/atom (121 kJ/mol $La_2Zr_2O_7$), compared to fully ordered pyrochlore. This energy is much higher than the oxygen-sublattice disordered phase (33 meV/atom, 35 kJ/mol $La_2Zr_2O_7$). Indeed, this penalty is so large that we find only the maximal configuration entropy could counteract it. At 2500 K, the maximal configurational entropy is achieved if both cation and anion sublattices are completely random. Its

contribution to free energy is

$$-TS_{\text{fluorite}} = kT \sum n_i \ln x_i / \sum n_i = -113 \text{ meV/atom.}$$

Therefore, unless this cation-disordered phase is highly random (i.e., with virtually no short-range order) in reality, it would be thermodynamically unfavored with respect to the pyrochlore phase.

We use two approaches to determine the randomness of this disordered phase. Our analysis shows this phase is only partially disordered, so it is thermodynamically unstable. In order to quantify the extent of disordering, we introduce a specific pair correlation as an order parameter. We select a pair cluster twice the distance between nearest neighbor La-La, and we calculate the pair correlation of cations, as shown in Table 4.4. Two benchmarks, ordered pyrochlore and completely disordered random fluorite, are listed for comparison. These data suggest the newly formed solid is partially disordered. SQS analysis also shows that the disordering is limited. We generate SQS, assuming complete disordering on both sublattices, i.e., the (La, Zr) and the (O, vacancy) sublattices. After structural optimization, we find some oxygen atoms moving to neighboring lattice sites, suggesting the SQS is unstable before configurational change. Such behavior means this disordered phase is constrained in a limited portion of configuration space, i.e., it is partially disordered.

Our theoretical result is confirmed by both X-ray diffraction and quenching experiments. Synchrotron X-ray diffraction experiments were performed on laser heated sample levitated in oxygen flow. Pyrochlore (111) reflections were observed up to complete melting (Fig. 4.6). The ratio of (111)/(222) reflections was previously used for evaluation of radiation induced antisite disorder in pyrochlores [116]. Our diffraction data indicate no significant variation (from 0.020 to 0.018) in (111)/(222) ratio with temperature. Experiments on containerless quenching and splat quenching of $La_2Zr_2O_7$ melt were performed using a splittable nozzle aerodynamic levitator. The pyrochlore phase was observed in all experiments with $La_2Zr_2O_7$, even though the fluorite phase has been obtained by this method for $Eu_2Zr_2O_7$ [118].

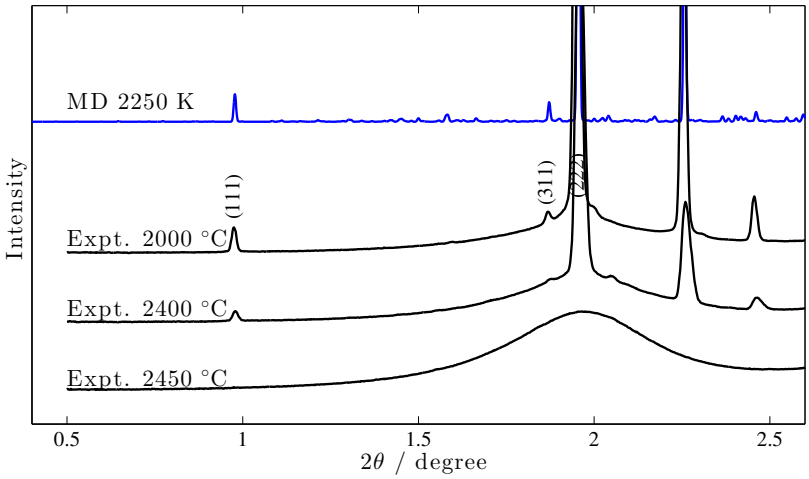

Figure 4.6: Synchrotron ($\lambda = 0.10798$ Å) X-ray diffraction of $La_2Zr_2O_7$ at $\sim 2000 - 2450$ °C. Pyrochlore (111) reflection is evident until complete melting. Theoretical X-ray diffraction from MD snapshots (generated by AFLOW/ACONVASP[117]) is plotted for comparision.

Differential thermal analysis also clearly indicates the absence of a metastable phase. Heat effects on melting and solidifying are quantified by differential thermal analysis. As shown in Fig. 4.2, the values from integration of peaks in heat flow on melting and crystallization are consistent within experimental uncertainty, indicating no formation of a metastable phase of significantly different energy upon crystallization.

Although we have strong evidence from both computation and experiment, we note that we still cannot completely rule out the possibility of a cation-disordered phase. The fact that this phase is present in MD simulation indicates that either the transition to pyrochlore phase is kinetically hindered or that this phase is slightly unstable relative to the pyrochlore phase so MD simulation does not reflect the stability difference. X-ray diffraction results do not completely exclude the possibility of disordering either. As a thermal gradient is present in the diffracted volume [92], the disordered phase could occur ∼100 °C below melting. Even if this is the case, the possibility of transient defect fluorite phase occurrence in $La_2Zr_2O_7$ right before melting can be treated more as a peculiarity of solid to liquid transition rather than solid state phase transition and of little significance for $La_2Zr_2O_7$ application as a thermal

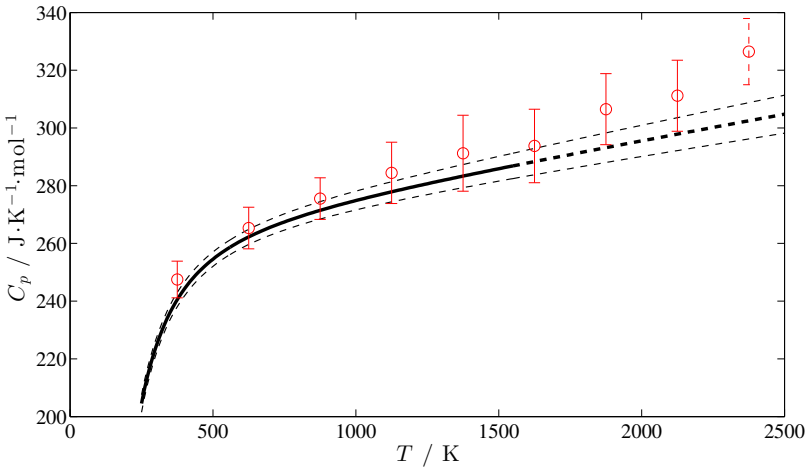

Figure 4.7: Heat capacity of pyrochlore $La_2Zr_2O_7$ up to melting temperature. Computational results are shown in red. The last data point at 2375 K may be invalid due to the possible transition to oxygen-sublattice disordered phase near 2500 K. No oxygen diffusion is observed below 2250 K. The black curve is from experiment up to 1550 K. [119]

barrier coating. Reported occurrences of lanthanum zirconate in disordered fluorite phase at low temperature in precipitates and in small particles from vapor deposition are likely to be induced by a surface energy term. This may play an important role in design of thermal barrier coating microstructures and choice of the method of their manufacturing and warrant separate investigation. However, analysis of these effects is beyond the scope of this paper.

4.2.4 Heat capacity

We calculate heat capacity in a temperature region up to the melting point. At each temperature, heat capacity is calculated as a derivative of enthalpy with respect to temperature. We run first-principles MD under the NPT ensemble to obtain the enthalpies at various temperatures. We include quantum corrections to vibrational energies, since they are significant at low temperatures.

$$\Delta H = \frac{1}{N}\sum_{i=1}^{3N}\left(0.5 + \frac{1}{\exp\left(h\nu_i/k_BT\right)-1}\right)\cdot h\nu_i - 3k_BT, \tag{4.3}$$

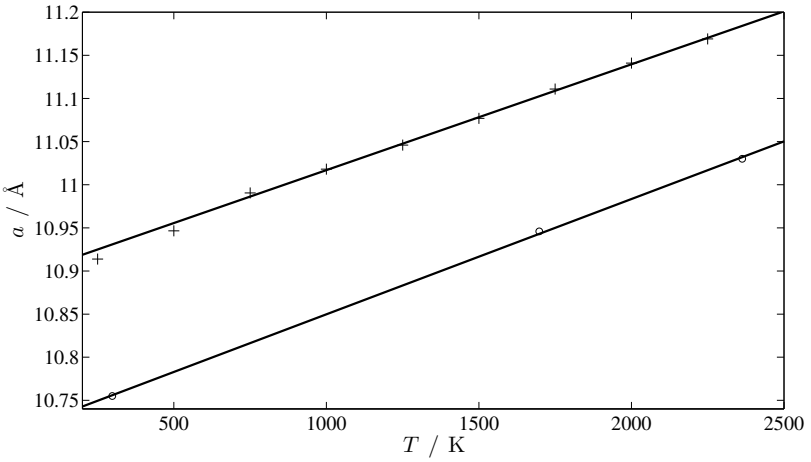

Figure 4.8: Lattice parameter at various temperatures in MD simulation ($_+$) and X-ray diffraction experiment ($\circ$). For theoretical thermal expansion, the coefficient is linearly fitted in temperature region $[1000, 2250]$ K. Lattice parameter is subject to quantum effect at low temperature, and thus the first two data points are underestimated.

where h is Planck constant, N is number of atoms, and ν is vibrational frequency. The ATAT package [115] is employed to calculate the phonon frequencies. The calculated heat capacities are shown in red in Fig. 4.7 and are found in good agreement with available experimental data at lower temperature.

4.2.5 Thermal expansion

Using the same procedure, thermal expansion coefficients are calculated, as shown in Fig. 4.8. The calculated thermal expansion coefficient is 11.1×10^{-6} K^{-1}.

Experimental thermal expansion coefficient (Fig. 4.8) is refined for the range 1400-2100 °C, from X-ray diffraction on a laser heated levitated sample. The difference in experimental and calculated cell parameters is due to both possible deviation in stoichiometry in laser melted lanthanum zirconate, and known overestimation from calculations (Table 1). However, the experimental value for thermal expansion coefficient, 11.5×10^{-6} K^{-1}, is in remarkable agreement with MD simulations.

4.3 Conclusions

In summary, we demonstrate how the combination of computations and experiments can accurately determine key material properties in a complementary manner, as illustrated by the example of $La_2Zr_2O_7$. These properties include fusion enthalpy, melting point, heat capacity, thermal expansion coefficients, and sublattice disordering phase transition. We identify the key factors that contribute to the high melting temperature, namely large fusion enthalpy, the presence of soft phonon modes, and sublattice disordering, which provide guidance in the design of novel refractories. The close agreement with experiment in the known but structurally complex compound $La_2Zr_2O_7$ provides good indication that the computation methods described herein can be used within a computational screening framework to identify novel refractory materials. Conversely, the calculation of thermal properties such as heat of fusion and heat capacity provides useful input for the calibration of an experimental apparatus aimed at calorimetry measurements at high temperatures, where calibration standards are currently lacking. This collaborative work also allowed us to identify high impact areas for computational and experimental efforts towards high temperature properties. Novel experimental techniques, such as structural studies at high temperature, provide validation between closely related phases often not unambiguously resolved computationally. Measurements of fusion enthalpies and heat capacities above 2000 °C are very challenging experimentally and can be greatly leveraged by computational methods.

Chapter 5

Design and search of novel refractory materials

High-performance refractory materials [71, 120, 121, 122] play an important role in applications ranging from gas turbines to heat shields for hypersonic vehicles. With melting points above 4000 K, hafnium carbide (HfC) [123, 124, 125, 126, 127, 129, 128] and tantalum carbide (TaC) [123, 130] are among the most refractory binary compounds known to date [131]. Their mixture, with a general formula $Ta_xHf_{1-x}C_y$, is known to have a melting point of 4215 K at the composition Ta_4HfC_5 [132] and has long been considered as the highest melting temperature for any solid [133] . Very few measurements of melting point in tantalum and hafnium carbides have been documented, because of the obvious experimental difficulties at extreme temperatures. Here we report an extensive investigation of the melting temperatures of these refractories using *ab initio* calculations, which let us identify three major chemical factors that contribute to the high melting temperatures. Based on these three factors, we propose and explore a new class of materials, which, according to our *ab initio* calculations, may possess even higher melting temperatures than Ta-Hf-C. This study also demonstrates the feasibility of materials screening and discovery via *ab initio* calculations for the optimization of "higher-level" properties whose determination requires extensive sampling of atomic configuration space.

Table 5.1: HSE correction on melting temperature. ΔH is heat of fusion. The bracket $\langle \cdots \rangle_{H^{PBE}}$ means that we randomly choose snapshots from MD trajectories of PBE, and calculate the energy differences between the two functionals.

material	T_m / K	ΔH / eV	$\langle H^{HSE} - H^{PBE} \rangle_{H^{PBE}}$ / eV		T_m correction / K
			solid	liquid	
HfC	3842	0.798	-1.566	-1.482	401
$HfC_{0.94}$	3861	0.808	-1.558	-1.452	502
$HfC_{0.88}$	3905	0.811	-1.531	-1.438	449
$HfC_{0.81}$	3962	0.786	-1.510	-1.416	470
$HfC_{0.75}$	3937	0.720	-1.489	-1.399	494

5.1 Hf-C system

To help identify the factors leading to high melting points and validate our computational methodology, we first explore trends among known classes of refractories. Employing the small-cell coexistence method, we calculate the melting temperatures of HfC_x ($x \in [0.75, 1]$), as shown in Fig. 5.1. Our calculations successfully capture the volcano-shape melting curve, which is widely observed in experiment [124, 126, 127, 129], as well as the location of the apex (within 3% (at.) of carbon content). Starting from stoichiometric HfC, the melting temperature increases along with carbon deficiency, until it reaches a maximum at the congruent melting point, near 45 atomic % C ($HfC_{0.82}$). This feature explains why HfC undergoes carbon loss when it is heated and melted [135]. Further decrease in carbon composition leads to a drop of melting temperature. The vertical shift of the melting curve, relative to experiment, does not appear to affect trends and amounts to about 5% of the melting temperature itself, which is typical for DFT calculations. We have cross-checked a subset of data points with more accurate, but considerably more expensive, HSE-based calculations and found an average shift upward by +460 K, which is consistent with the observed shift (see Table 5.1).

The high melting temperature of hafnium carbide is primarily (through the well-known relation $T_m = \Delta H / \Delta S$) due to its exceptionally large fusion enthalpy of 0.81 eV·atom^{-1}, a value usually unparalleled among refractories. (For reference, Al_2O_3 (m.p. 2345 K): 0.22; W (m.p. 3695 K): 0.37; Hf (m.p. 2506 K): 0.26 eV·atom^{-1}.)

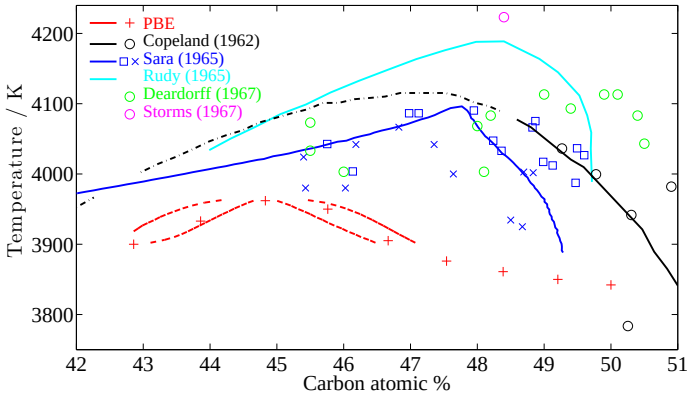

Figure 5.1: Hf-C phase diagram. Prior experimental measurements of the melting points are compared with the present computational results (labelled "PBE" as they rely on the Perdew-Burke-Ernzerhof functional [39]). The temperatures where free energies of the liquid and of the solid intersect are marked by "+". Also shown are the solidus and liquidus obtained via a CALPHAD model [134]. The vertical shift of theoretical phase diagram is mostly due to density functional theory (DFT) error. We estimate the melting point correction to be +460 K, based on the more accurate (but much more expensive) hybrid Heyd-Scuseria-Ernzerhof (HSE) functional [94].

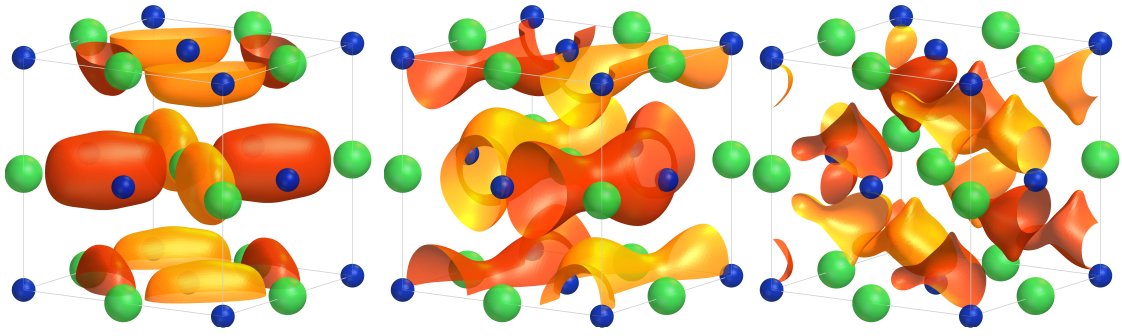

Figure 5.2: Wavefunctions illustrating the diversity of bond types in HfC with clear covalent character. From left to right, these figures represent Hf $5d$ σ bond, C $2p$ σ bond, and Hf $5d$−C $2p$ π bond. Surfaces of constant value in the real part of the wavefunction are represented. Hf and C atoms are colored yellow and gray respectively.

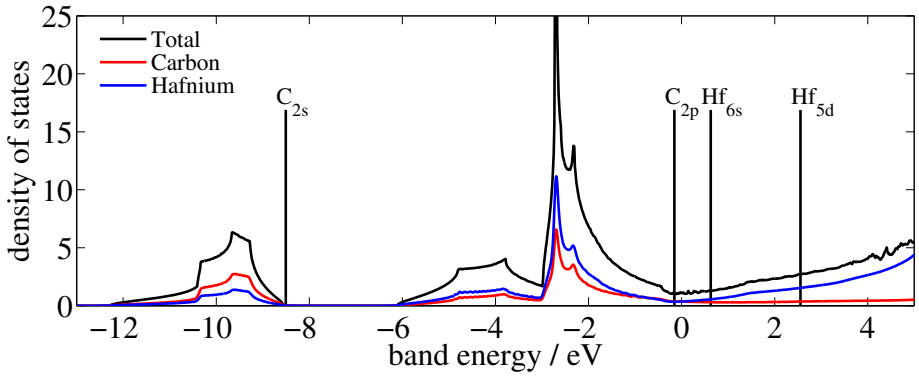

Figure 5.3: Electronic density of states in HfC showing clear participation of both Hf and C in forming covalent bonds. Total density of states is shown in black. Projections on C and Hf are colored red and blue, respectively. The Fermi level is at 0. Vertical lines are energy levels of atomic orbitals.

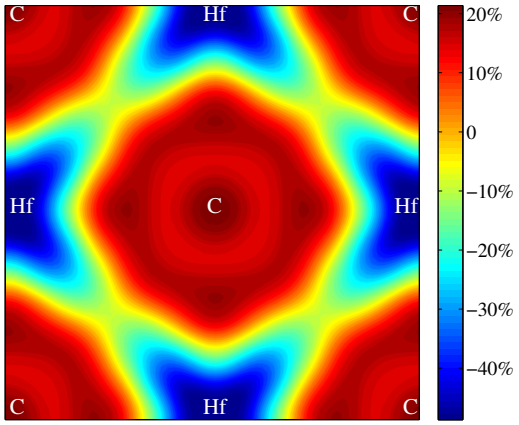

Figure 5.4: Electron transfer in HfC. The figure reports $\rho/\rho_0 - 1$, where ρ is electronic charge density from DFT wavefunction and ρ_0 is initial overlapping atomic charge density. The sharp contrast clearly shows a charge transfer from Hf to C indicative of ionic interactions, although covalent character is still visible in the anisotropy of the charge density.

Indeed, a large heat of fusion is the first and most prominent factor we find that contributes to a high melting point. The chemical origin of the remarkably large heat of fusion can be studied via a wavefunction analysis. The system's wavefunctions, illustrated in Fig. 5.3, reveal numerous types of chemical interactions, including Hf−Hf $5d$ σ bond, C−C $2p$ σ bond and Hf $5d$−C $2p$ π bond. This diversity enables each atom to bind with all its first *and* second nearest neighbors, thus forming an unsually large number of bonds and promoting the formation of a deep valence band (see Fig. 5.3). These bonds also carry both covalent and ionic characters: on one hand, the decomposed density of states (Fig. 5.3) shows contribution from both carbon and hafnium, hence demonstrating a typical covalent bond pattern. On the other hand, charge density analysis (Fig. 5.4) clearly shows partial charge transfer from hafnium to carbon, which is strong evidence of ionic bonding, and is confirmed by a Bader charge analysis [136] indicating a $0.62e$ charge transfer.

The second contributor we recognize is the presence of point defects, which affect melting temperature via entropy. More generally, we find that, at high temperatures, entropic effects favor and stabilize a considerable amount of lattice defects. When solid HfC becomes off-stoichiometric HfC_{1-x}, the presence of carbon vacancies increases the configurational entropy (e.g., for an ideal lattice solution, $S = -k\sum_i x_i \ln x_i$), and this benefit is further magnified by the high temperature ($G = H - TS$). If this entropic effect more than offsets the defect formation energy penalty, these vacancies stabilize the solid phase. Since, by definition, vacancies can only exist in the solid phase, this effect is absent in the liquid and the net effect would be an increase in melting temperature.

Indeed, this fact explains why melting point climbs when HfC becomes off-stoichiometic and carbon-deficient, a phenomenon widely observed in experiments (Fig. 5.1). Furthermore, this entropic effect becomes so large at high temperatures that it not only stabilizes defects, but facilitates their formation as well. For instance, we observe the formation of C_2 (two carbon atoms near one anion lattice site) and vacancy in MD simulations, especially for compositions close to stoichiometric HfC. These unstable C_2 complexes tend to leave the solid, which results in carbon loss of stoichiometric

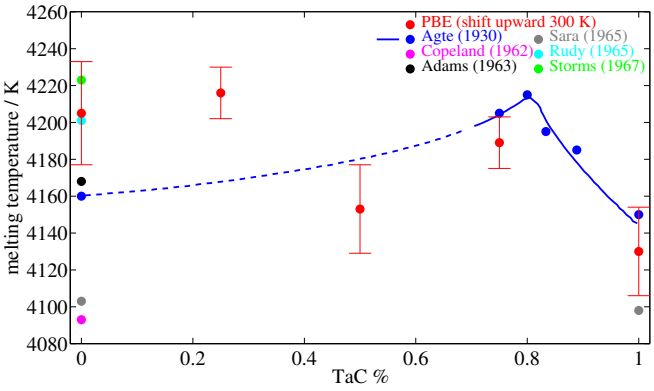

Figure 5.5: Melting temperature of $Ta_xHf_{1-x}C_{0.875}$ as a function of x. This illustrates the effect of tuning, via alloying, the Fermi level so that it lies precisely between the bonding and antibonding bands. The inset shows the effect on the Fermi level of the solid phase by tuning composition in $Ta_xHf_{1-x}C$. Vertical lines are Fermi levels.

HfC.

5.2 Hf-Ta-C sytem

The third chemical factor we identify is well exemplified in the Hf-Ta-C system. While binary carbides, such as HfC and TaC, are constrained by the given electronic properties of these metals, mixing two carbides provides an avenue to tune chemical properties. Hf and Ta share a similar electronic structure but a slightly different number of valance electrons, which allows tuning of the location of the Fermi level so that it lies precisely between the bonding and anti-bonding bands without distorting the density state.

To investigate this effect, we calculate melting points of $Hf_xTa_{1-x}C_{0.875}$ at various compositions ($x = 0, 0.25, 0.5, 0.75, 1$). The Hf-Ta-C system contains Ta_4HfC_5, which has long been considered as the most refractory substance known to date. Our computational results, in general, agree with Agte's experimental measurements [132], as shown in Fig. 5.5. Our calculation indeed captures a cusp in the composition-dependence of the melting point. While Agte found HfC has a melting temperature only 10 K higher than TaC [132], later publications tended to show HfC melting at least 100 K above TaC [131]. Our calculations corroborate the later measurements,

with a calculated melting temperature of HfC ∼70 K higher than that of TaC.

5.3 Hf-C-N system

Guided by the three contributing factors discussed above, we explore a new class of refractory materials, which may have higher melting temperatures than Hf-Ta-C. (1) We focus on isostructural alternatives to Hf-Ta-C, because the strong binding with both first and second-nearest neighbors is a very favorable feature we wish to maintain. For the same reason, we look for alternate composition with similar cation/anion atomic radius ratios and similar electronegativity differences. (2) To preserve the ability to tune the Fermi level, we consider more than one element on both the cation and the anion sublattices and start with a composition space including Ta, Hf, B, C, and N. Including more transition metals did not appear beneficial since the valance electron density of Ta and Hf already brackets the optimal Fermi level for the rocksalt crystal structure considered here. For the anions, atom size and electronegativity considerations (to preserve the rocksalt crystal structure) lead us to limit ourselves to 2p elements. (3) According to known melting temperatures of binary compounds (HfB: 2280 (decompose); HfN: 3660; TaB: 3360; TaN: 3370 K), we identified the Hf-C-N ternary subsystem as a promising candidate. HfN, a solid in rocksalt structure like HfC, has the highest melting temperature of all known metal nitrides. The high stability of both HfN and HfC suggests a thermally stable ternary system. Indeed, we find that the Hf-C-N system generally has a larger heat of fusion than HfC does. (4) To exploit possible entropic effects, we allow for vacancies on the anion sublattice.

Our calculations indicate that the Hf-C-N system includes materials that have higher melting points than any other substances known to date. As shown in Fig. 5.6, we find a large number of Hf-C-N mixtures, whose melting temperatures are significantly higher than the Hf-C and Hf-Ta-C systems (see Table 5.2). These new refractory materials increase the melting temperature record by up to 200 K. A regression analysis of our melting point data indicates that the highest melting point

Table 5.2: Melting temperatures from small-cell coexistence calculations.

chemical formula	melting temperature / K
HfC	3842 ± 25
$HfC_{0.97}$	3850 ± 34
$HfC_{0.94}$	3861 ± 21
$HfC_{0.91}$	3876 ± 24
$HfC_{0.88}$	3905 ± 27
$HfC_{0.84}$	3950 ± 17
$HfC_{0.81}$	3962 ± 27
$HfC_{0.78}$	3936 ± 12
$HfC_{0.75}$	3937 ± 17
$Hf_{0.75}Ta_{0.25}C_{0.88}$	3916 ± 19
$Hf_{0.5}Ta_{0.5}C_{0.88}$	3869 ± 16
$Hf_{0.25}Ta_{0.75}C_{0.88}$	3989 ± 14
$TaC_{0.88}$	3830 ± 24
$HfC_{0.75}N_{0.22}$	4039 ± 26
$HfC_{0.62}N_{0.19}$	4081 ± 12
$HfC_{0.56}N_{0.38}$	4141 ± 21
$HfC_{0.56}N_{0.25}$	4082 ± 28
$HfC_{0.5}N_{0.25}$	4055 ± 24
$HfC_{0.44}N_{0.5}$	4106 ± 14
$HfC_{0.44}N_{0.19}$	3847 ± 24
$HfC_{0.38}N_{0.38}$	4008 ± 19
$Hf_{0.75}Ta_{0.25}C_{0.56}N_{0.25}$	3980 ± 13

Table 5.3: A regression analysis on melting temperatures in the Hf-Ta-C-N system. The quadratic function is fitted to the expression $T_m = k_1(x\cos\theta + y\sin\theta - a_1)^2 + k_2(-x\sin\theta + y\cos\theta - a_2)^2 + T_0$, where x and y are compositions in HfC_xN_y.

T_0	k_1	k_2	a_1	a_2	θ
4135 K	−947 K	−7302 K	0.654	0.0456	-0.285π

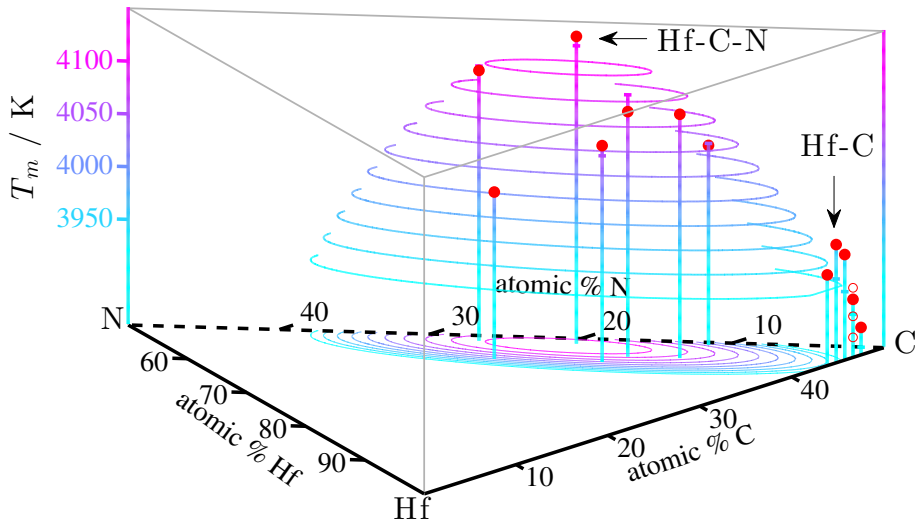

Figure 5.6: Melting temperatures of Ta-Hf-C-N alloys. Filled circles mark the calculated melting temperatures in the Hf-C and Hf-C-N systems while open circles show data from the Ta-Hf-C system for comparison. The melting temperature surface $T_m(x_N, x_C)$ (shown as contour lines) was obtained via a regression analysis of the calculated melting temperatures based on a quadratic function of composition.

is located in the vicinity of $x_N = 0.20$ and $x_C = 0.27$ (see Table 5.3). We find that Ta does not help increase the melting temperature further. As the calculations are performed under constant pressure conditions, they can determine whether the solid melts or sublimates and only melting is observed. However, the calculations do not include the possible effects of an oxygen-rich environment (carbon loss and oxidation) and are thus representative of heating under an inert atmosphere (e.g., nitrogen).

In investigating this broader class of systems, we have observed another, independent, melting point-enhancing mechanism. We find that the addition of nitrogen remarkably changes the liquid structure and renders the phase less stable, which hinders melting. We explain this effect as follows. A liquid is more stable at a high temperature because it can access a much larger phase space, which contributes to a larger entropy that offsets its higher energy. In particular, the liquid allows for a richer variety of pairwise correlations. For instance, while there are only Hf−X (X=C, N) nearest neighbors in solid-state Hf-C-N, additional pairs such as Hf−Hf and X1−X2 (X1, X2=C, N) are allowed in the liquid. This is an important entropic benefit in favor of the liquid phase, provided these new pairs do not entail too much energy

penalty. We find that the main impact of the additional nitrogen is via the unstable C−N and N−N pairs, which is made clear in the following two analyses. First, we calculate defect formation energy of X−X (X=C,N) in the matrix of solid-state HfC as

$$\Delta E \;=\; E(\text{a X-X pair on one anion lattice site}) + E(\text{vacancy}) - 2E(\text{X}).$$

This quantity measures the energy cost to move a X atom from an anion sublattice site (leaving a vacancy at the site) to another anion (creating a X−X pair at the site). We find N−N has a much higher defect formation energy than C−C (5.8 vs. 3.6 eV), which suggests a larger energy penalty when breaking Hf−N bonds to form N−N, a necessary step to melt the solid. As this process becomes less favorable with nitrogen added, the Hf-C-N system is harder to melt. Indeed, the heat of fusion is larger in the Hf-C-N system (see Fig. 5.7). Second, the pair-correlation function in Hf-C-N liquid (Fig. 5.8) shows dramatically lower occurrence of C−N and N−N, compared to a considerable amount of C−C pairs. This is also due to the higher formation energy of these two pairs. Indeed, a nitrogen atom has significantly less tendency than carbon (Fig. 5.8) to couple with the anions (C and N). The addition of nitrogen atoms largely reduces the number of anion-anion pairs in the liquid, forcing them to bind with Hf. This constraint limits the accessible phase space of the liquid and thus reduces its entropy. Fig. 5.9 formally quantifies this effect in the Hf-C-N system. The relative instability of the N−N bond may appear strange at first, as the nitrogen molecule (N_2) is usually considered very stable. However, when a N−N complex is also bound to other atoms, its stability can significantly decrease, as commonly observed in other compounds. For example, azide, a common compound with an anion N_3^-, is usually explosive, hydrazine (N_2H_4) is used as high-energy rocket fuels, and dinitrogen tetroxide (N_2O_4) easily undergoes decomposition to its monomer (NO_2) under room temperature.

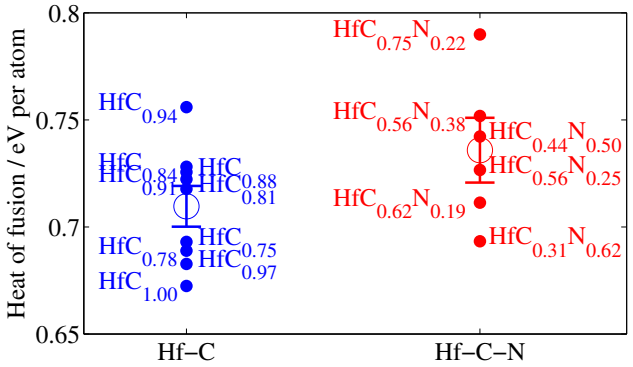

Figure 5.7: Heat of fusion in Hf-C (blue) and Hf-C-N (red) systems. Each solid dot corresponds to one compound, while an open circle with error bar is the average and standard error. The addition of nitrogen increases the heat of fusion by 4%, which is comparable to the increment of melting temperature. Here heat of fusion is derived as a byproduct of melting temperature calculations, according to Ref. 16 in main text.

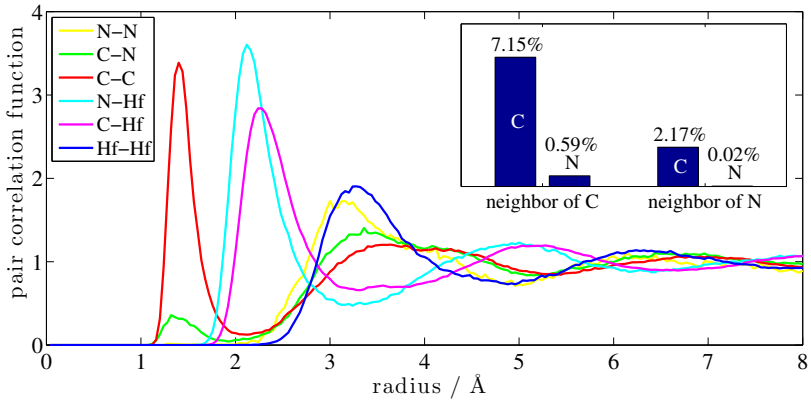

Figure 5.8: Pair correlation function (normalized as $r \to \infty$) in liquid-state $Hf_{32}C_{24}N_7$. We find a remarkable difference between carbon and nitrogen: there is nearly no N−N (yellow) "near neighbors" (first pair correlation peak), compared to a considerable amount of C−C (red). The inset shows compositions of near neighbors for C and N atoms in liquid-state $Hf_{32}C_{24}N_7$ (the compositions of Hf−C and Hf−N count for the rest and are omitted). N atom has significantly less tendency to couple with C (2.17% vs. 7.15%) and N (0.02% vs. 0.59%).

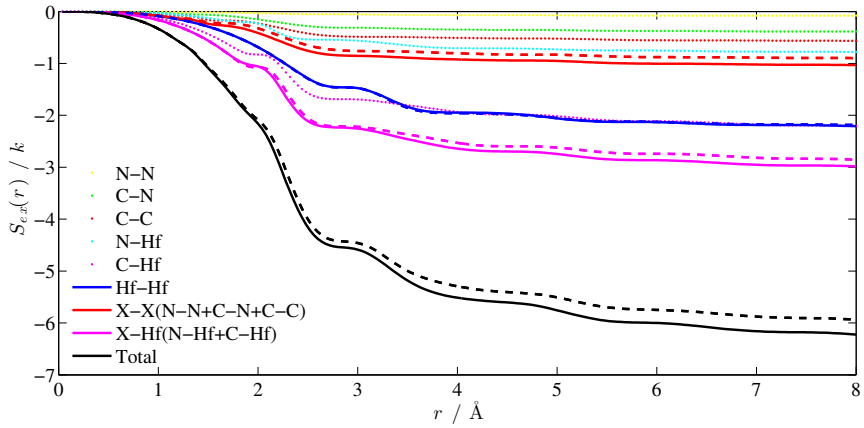

Figure 5.9: Comparison of the entropies of liquid-state $Hf_{32}C_{31}$ (dash lines) and $Hf_{32}C_{24}N_7$ (dot and solid lines). Shown are excess entropies (with respect to ideal gas) calculated from pair-correlation functions, according to the relation $S_{ex}/k_B = -2\pi\rho \sum_{i,j} x_i x_j \int_0^\infty \Big(g_{ij}(r) \ln g_{ij}(r) - \big[g_{ij}(r) - 1 \big] \Big) r^2 \, \mathrm{d}r$, where ρ is density, x_i is fractional composition, and g_{ij} is pair correlation function between species i and j. It is evident that nitrogen brings down the total entropy (black), through anion-anion (X−X, red) and anion-cation (X−Hf, purple) pairs, while leaving the cation-cation (Hf−Hf, blue) contribution nearly untouched.

5.4 Conclusions

In summary, we have identified and investigated, via electronic structure calculations, three factors responsible for the exceptionally high melting points in a class of transition metal carbides: (i) the presence of a large number of strong bonds between both nearest and second nearest neighbors that exhibit a mixture of strong covalent and strong ionic characters; (ii) the entropy contribution of point defects that can exists in the solid but in the liquid (such as vacancies); (iii) the ability to tune, via alloying, the position of the Fermi level so that it lies just between the bonding and anti-bonding bands. These observations suggest the exploration of the Ta-Hf-C-N system in order to further increase the melting point. Our calculations suggest that a Hf-C-N alloy with 20 at. % of N and 27 at. % of C increases the current melting point record by up to 200 K and identify a melting point increase mechanism mediated by changes in pair correlation functions.

Chapter 6

Conclusions

In this thesis, we present two new methods, i.e., the improved Widom particle insertion method and the small-cell coexistence method, which we developed in order to capture melting temperatures both accurately and quickly.

Using a modification of Widom's particle insertion method, we demonstrate that it is computationally practical to calculate the chemical potential of a liquid directly from first principles, i.e., without the help of any high-quality empirical potentials, which are available only for a limited number and type of materials. This distinct advantage is crucial when such empirical potentials are difficult to obtain, e.g., for multi-component materials. An algorithm is proposed to efficiently find and study cavities. It reduces the computational cost drastically, e.g., by more than three orders of magnitude for the example we study, relative to Widom's original method. We present an application to the chemical potential and melting temperature calculation of copper.

We develop the small-cell coexistence method based on the statistical analysis of small-size coexistence MD simulations, so it circumvents both the hysteresis overheating problem in small system size and the prohibitive computer cost in traditional coexistence method. Using empirical potentials, we present the validation of the method and systematically study the finite-size effect on the melting temperature's calculated. Through the DFT examples, we demonstrate the capability and flexibility of the method in its practical applications.

The small-cell coexistence method is extensively utilized in two studies of refrac-

tory materials. (1) In a combined computational and experimental study of $La_2Zr_2O_7$, we demonstrate how the combination can accurately determine key material properties in a complementary manner. These properties include fusion enthalpy, melting point, heat capacity, thermal expansion coefficients, and sublattice disordering phase transition. The close agreement with experiment in the known but structurally complex compound $La_2Zr_2O_7$ provides a good indication that the computation methods described herein can be used within a computational screening framework to identify novel refractory materials. Conversely, the calculation of thermal properties such as heat of fusion and heat capacity provides useful input for the calibration of an experimental apparatus aimed at calorimetry measurements at high temperatures, where calibration standards are currently lacking. (2) Based on melting temperature calculations of the Hf-Ta-C system, we have identified and investigated, via electronic structure calculations, key factors responsible for the exceptionally high melting points in a class of transition metal carbides. These investigations suggest the exploration of the Hf-Ta-C-N system in order to further increase the melting point. Our calculations suggest that a Hf-C-N alloy with 20 at. % of N and 27 at. % of C increases the current melting point record by up to 200 K and identify a melting point increase mechanism mediated by changes in pair correlation functions.

Bibliography

[1] D. Frenkel and B. Smit, *Understanding Molecular Simulation* (Academic, San Diego, 1996).

[2] P. Hohenberg and W. Kohn, Phys. Rev. B **136**, B864 (1964).

[3] W. Kohn and L. J. Sham, Phys. Rev. B **140**, 1133 (1965).

[4] R. Jones and O. Gunnarsson, Rev. Mod. Phys. **61**, 689 (1989).

[5] M. I. Mendelev, M. J. Kramer, C. A. Becker, and M. Asta, Phil. Mag. **88**, 1723 (2008).

[6] J. Mei and J. W. Davenport, Phys. Rev. B **46**, 21 (1992).

[7] J. Morris, C. Wang, K. Ho, and C. Chan, Phys. Rev. B **49**, 3109 (1994).

[8] A. B. Belonoshko, Geochim. Cosmochim. Acta **58**, 4039 (1994).

[9] T. Ogitsu, E. Schwegler, F. Gygi, and G. Galli, Phys. Rev. Lett. **91**, 175502 (2003).

[10] D. Alfe, Phys. Rev. Lett. **94**, 235701 (2005).

[11] J.-Y. Raty, E. Schwegler, and S. A. Bonev, Nature **449**, 448 (2007).

[12] A. B. Belonoshko, N. V. Skorodumova, A. Rosengren, and B. Johansson, Phys. Rev. B **73**, 012201 (2006).

[13] A. B. Belonoshko, S. Arapan, R. Martonak, and A. Rosengren, Phys. Rev. B **81**, 054110 (2010).

[14] A. B. Belonoshko and A. Rosengren, Phys. Rev. B **85**, 174104 (2012).

[15] D. Alfe, C. Cazorla, and M. J. Gillan, J. Chem. Phys. **135**, 024102 (2011).

[16] A. B. Belonoshko, T. Lukinov, L. Burakovsky, D. L. Preston, and A. Rosengren, European Physical Journal-Special Topics **216**, 199 (2013).

[17] O. Sugino and R. Car, Phys. Rev. Lett. **74**, 1823 (1995).

[18] G. de Wijs, G. Kresse, and M. Gillan, Phys. Rev. B **57**, 8223 (1998).

[19] D. Alfè, M. Gillan, and G. Price, Nature **401**, 462 (1999).

[20] D. Alfè, G. Price, and M. Gillan, Phys. Rev. B **65**, 165118 (2002).

[21] V. Weber and D. Asthagiri, J. Chem. Phys. **133**, 141101 (2010).

[22] D. Kofke and P. Cummings, Mol. Phys. **92**, 973 (1997).

[23] D. Alfè, G. De Wijs, G. Kresse, and M. Gillan, Int. J. Quantum Chem. **77**, 871 (2000).

[24] S. T. Lin, M. Blanco, and W. A. Goddard, J. Chem. Phys. **119**, 11792 (2003).

[25] T. A. Pascal, S. T. Lin, and W. A. Goddard, Phys. Chem. Chem. Phys. **13**, 169 (2011).

[26] C. Zhang, L. Spanu, and G. Galli, J. Phys. Chem. B **115**, 14190 (2011).

[27] B. Widom, J. Chem. Phys. **39**, 2808 (1963).

[28] S. Romano and K. Singer, Mol. Phys. **37**, 1765 (1979).

[29] K. S. Shing and K. E. Gubbins, Mol. Phys. **46**, 1109 (1982).

[30] D. Moller and J. Fischer, Mol. Phys. **69**, 463 (1990).

[31] A. Lotfi, J. Vrabec, and J. Fischer, Mol. Phys. **76**, 1319 (1992).

[32] J. Anwar, D. Frenkel, and M. Noro, J. Chem. Phys. **118**, 728 (2003).

[33] J. Forsman and B. Jonsson, J. Chem. Phys. **101**, 5116 (1994).

[34] J. Kim, R. L. Martin, O. Rubel, M. Haranczyk, and B. Smit, J. Chem. Theory Comput. **8**, 1684 (2012).

[35] G. Kresse and J. Furthmüller, Comput. Mater. Sci. **6**, 15 (1996).

[36] G. Kresse and J. Furthmüller, Phys. Rev. B **54**, 11169 (1996).

[37] P. Blöchl, Phys. Rev. B **50**, 17953 (1994).

[38] G. Kresse and D. Joubert, Phys. Rev. B **59**, 1758 (1999).

[39] J. Perdew, K. Burke, and M. Ernzerhof, Phys. Rev. Lett. **77**, 3865 (1996).

[40] S. Nosé, Mol. Phys. **52**, 255 (1984).

[41] S. Nosé, J. Chem. Phys. **81**, 511 (1984).

[42] W. G. Hoover, Phys. Rev. A **31**, 1695 (1985).

[43] G. J. Martyna, M. L. Klein, and M. Tuckerman, J. Chem. Phys. **97**, 2635 (1992).

[44] B. Smit and D. Frenkel, J. Phys. Condens. Matter **1**, 8659 (1989).

[45] J. Siepmann, I. McDonald, and D. Frenkel, J. Phys. Condens. Matter **4**, 679 (1992).

[46] A. van de Walle and G. Ceder, Rev. Mod. Phys. **74**, 11 (2002).

[47] A. van de Walle, M. Asta, and G. Ceder, CALPHAD J. **26**, 539 (2002).

[48] A. van de Walle, CALPHAD J. **33**, 266 (2009).

[49] S. J. Plimpton, J. Comp. Phys. **117**, 1 (1995).

[50] Y. H. Li, D. J. Siegel, J. B. Adams, and X. Y. Liu, Phys. Rev. B **67**, 125101 (2003).

[51] P. J. Steinhardt, D. R. Nelson, and M. Ronchetti, Phys. Rev. B **28**, 784 (1983).

[52] Y. T. Wang, S. Teitel, and C. Dellago, J. Chem. Phys. **122**, 214722 (2005).

[53] M. R. Fellinger, H. Park, and J. W. Wilkins, Phys. Rev. B **81**, 144119 (2010).

[54] G. Kresse and D. Joubert, Phys. Rev. B **59**, 1758 (1999).

[55] S. Taioli, C. Cazorla, M. J. Gillan, and D. Alfe, Phys. Rev. B **75**, 214103 (2007).

[56] Y. Wang and J. P. Perdew, Phys. Rev. B **44**, 13298 (1991).

[57] E. Gregoryanz, O. Degtyareva, M. Somayazulu, R. J. Hemley, and H. K. Mao, Phys. Rev. Lett. **94**, 185502 (2005).

[58] H. Eshet, R. Z. Khaliullin, T. D. Kuhne, J. Behler, and M. Parrinello, Phys. Rev. Lett. **108**, 115701 (2012).

[59] E. R. Hernandez and J. Iniguez, Phys. Rev. Lett. **98**, 055501 (2007).

[60] A. Yamane, F. Shimojo, and K. Hoshino, J. Phys. Soc. Jpn. **77**, 064603 (2008).

[61] B. B. Laird and A. D. J. Haymet, Phys. Rev. A **45**, 5680 (1992).

[62] Cleaver B. Nature **207**, 1291 (1965).

[63] J. A. Labrincha, J. R. Frade and F. M. B. Marques, J. Mater. Sci. **28**, 3809 (1993).

[64] A. Mitterdorfer and L. J. Gauckler, Solid State Ionics **111**, 185 (1998).

[65] R. A. McCauley and F. A. Hummel, J. Lumin. **6**, 105 (1973).

[66] H. Otaki, H. Kido, T. Hoshikawa, M. Shimada and M. Koizumi, J. Ceram. Soc. Jpn. **96**, 124 (1988).

[67] D. Andriamasinoro, R. Kieffer, A. Kiennemann and P. Poix, Appl. Catal. A-General **106**, 201 (1993).

[68] J. Bussi, S. Parodi, B. Irigaray and R. Kieffer, Appl. Catal. A-General **172**, 117 (1998).

[69] T. G. Chirayil, M. Paranthaman, D. B. Beach, D. F. Lee, A. Goyal, R. K. Williams, X. Cui, D. M. Kroeger, R. Feenstra, D. T. Verebelyi and D. K. Christen, Physica C **336**, 63 (2000).

[70] K. Knoth, R. Huhne, S. Oswald, L. Schultz and B. Holzapfel, Acta Mater. **55**, 517 (2007).

[71] N. P. Padture, M. Gell and E. H. Jordan, Science **296**, 280 (2002).

[72] R. A. Miller, Surf. Coat. Tech. **30**, 1 (1987).

[73] G. W. Goward, Surf. Coat. Tech. **108**, 73 (1998).

[74] A. G. Evans, D. R. Mumm, J. W. Hutchinson, G. H. Meier and F. S. Pettit, Prog. Mater. Sci. **46**, 505 (2001).

[75] D. R. Clarke and C. G. Levi, Annu. Rev. Mater. Res. **33**, 383 (2003).

[76] X. Q. Cao, R. Vassen and D. Stoever. J. Eur. Ceram. Soc. **24**, 1 (2004).

[77] M. J. Maloney, European Patent No. EP 0848077 A1 (1998).

[78] R. Vassen, X. Q. Cao, F. Tietz, D. Basu and D. Stover, J. Am. Ceram. Soc. **83**, 2023 (2000).

[79] A. V. Radha, S. V. Ushakov and A. Navrotsky, J. Mater. Res. **24**, 3350 (2009).

[80] X. Q. Cao, R. Vassen, W. Jungen, S. Schwartz, F. Tietz and D. Stover, J. Am. Ceram. Soc. **84**, 2086 (2001).

[81] R. A. Miller, J. L. Smialek, R. G. Garlick, Phase Stability in Plasma-Sprayed Partially Stabilized ZirconiaYttria, pp. 24151, in: Heuer AH, Hobbs LW (Eds.) Advances in Ceramics, Vol. 3, Science and Technology of Zirconia. Columbus, OH: American Ceramic Society (1981).

[82] Belonoshko AB, Skorodumova NV, Rosengren A, Johansson B. Phys Rev B 2006;73:012201.

[83] Lin ST, Blanco M, Goddard WA. J Chem Phys 2003;119:11792.

[84] Wang LG, van de Walle A. Phys Chem Chem Phys 2012;14:1529.

[85] Wang LG, van de Walle A, Alfe D. Phys Rev B 2011;84:092102.

[86] M. A. Subramanian, G. Aravamudan, G. V. S. Rao, Prog. Solid State Chem. **15**, 55 (1983).

[87] P. J. Wilde and C. R. A. Catlow, Solid State Ionics **112**, 173 (1998).

[88] R. E. Williford and W. J. Weber, J. Am. Ceram. Soc. **82**, 3266 (1999).

[89] R. E. Williford, W. J. Weber, R. Devanathan and J. D. Gale, J. Electroceram. **3**, 409 (1999).

[90] R. A. Felice, AIP Conf. Proc. **684**, [Pt. 2], 7116 (2003).

[91] S. V. Ushakov and A. Navrotsky, J. Mater. Res. **26**, 845 (2011).

[92] S. V. Ushakov and A. Navrotsky, J. Am. Ceram. Soc. **95**, 1463 (2012).

[93] B. H. Toby and R. B. Von Dreele, J. Appl. Cryst. **46**, 544 (2013).

[94] J. Heyd, G. E. Scuseria and M. Ernzerhof, J. Chem. Phys. **124**, 219906 (2006).

[95] S. M. Lakiza and L. M. Lopato, J. Eur. Ceram. Soc. **25**, 1373 (2005).

[96] E. I. Zoz, A. M. Gavrish and N. V. Gulko, Izv. Akad. Nauk. SSSR Neorg. Mater. **14**, 109 (1978).

[97] K. I. Portnoi, N. I. Timofeeva, S. E. Salibekov and I. V. Romanovich, Izv. Akad. Nauk. SSSR Neorg. Mater. **8**, 406 (1972).

[98] A. Rouanet, Rev. Int. Hautes. Temp. **8**, 161 (1971).

[99] T. H. Lin and H. C. Yu, Guisuanyan Xuebao **3**, 159 (1964).

[100] R. C. Ewing, W. J. Weber and J. Lian, J. Appl. Phys. **95**, 5949 (2004).

[101] J. Lian, X. T. Zu, K. V. G. Kutty, J. Chen, L. M. Wang and R. C. Ewing, Phys. Rev. B **66**, 054108 (2002).

[102] B. D. Begg, N. J. Hess, W. J. Weber, R. Devanathan, J. P. Icenhower, S. Thevuthasan and B. P. McGrail, J. Nucl. Mater. **288**, 208 (2001).

[103] K. E. Sickafus, L. Minervini, R. W. Grimes, J. A. Valdez, M. Ishimaru, F. Li, K. J. McClellan and T. Hartmann, Science **289**, 748 (2000).

[104] L. Minervini, R. W. Grimes and K. E. Sickafus, J. Am. Ceram. Soc. **83**, 1873 (2000).

[105] A. Chartier, C. Meis, W. J. Weber and L. R. Corrales, Phys. Rev. B **65**, 134116 (2002).

[106] J. Lian, L. Wang, J. Chen, K. Sun, R. C. Ewing, J. M. Farmer, L. A. Boatner, Acta Mater. **51**, 1493 (2003).

[107] N. J. Hess, B. D. Begg, S. D. Conradson, D. E. McCready, P. L. Gassman and W. J. Weber, J. Phys. Chem. B **106**, 4663 (2002).

[108] S. V. Ushakov, C. E. Brown and A. Navrotsky, J. Mater. Res. **19**, 693 (2004).

[109] G. Mills, H. Jonsson and G. K. Schenter Surf. Sci. **324**, 305 (1995).

[110] G. Henkelman and H. Jonsson, J. Chem. Phys. **113**, 9978 (2000).

[111] J. M. Sanchez, F. Ducastelle and D. Gratias, Physica A **128**, 334 (1984).

[112] A. van de Walle and G. Ceder J. Phase Equilib. **23**, 348 (2002).

[113] A. Zunger, S. H. Wei, L. G. Ferreira and J. E. Bernard, Phys. Rev. Lett. **65**, 353 (1990).

[114] A. van de Walle, P. Tiwary, M. de Jong, D. L. Olmsted, M. Asta, A. Dick, D. Shin, Y. Wang, L. Q. Chen and Z. K. Liu, Calphad **42**, 13 (2013).

[115] A. van de Walle, M. Asta and G. Ceder, Calphad **26**, 539 (2002).

[116] Y. H. Li, B. P. Uberuaga, C. Jiang, S. Choudhury, J. A. Valdez, M. K. Patel, J. Won, Y. Q. Wang, M. Tang, D. J. Safarik, D. D. Byler, K. J. McClellan, I. O. Usov, T. Hartmann, G. Baldinozzi and K. E. Sickafus, Phys. Rev. Lett. **108**, 195504 (2012).

[117] S. Curtarolo, W. Setyawan, G. L. W. Hart, M. Jahnatek, R. V. Chepulskii, R. H. Taylor, S. D. Wanga, J. K. Xue, K. S. Yang, O. Levy, M. J. Mehl, H. T. Stokes, D. O. Demchenko and D. Morgan, Comp. Mater. Sci. **58**, 218 (2012).

[118] M. P. Saradhi, S. V. Ushakov and A. Navrotsky, RSC Advances **2**, 3328 (2012).

[119] D. Sedmidubsky, O. Benes, R. J. M. Konings, J. Chem. Thermodyn. **37**, 1098 (2005).

[120] Perepezko, J. H. The hotter the engine, the better. *Science* **326**, 1068 (2009).

[121] Lu, K. The future of metals. *Science* **328**, 319 (2010).

[122] Liu, G., Zhang, G. J., Jiang, F., Ding, X. D., Sun, Y. J., Sun, J. and Ma, E. Nanostructured high-strength molybdenum alloys with unprecedented tensile ductility. *Nat. Mater.* **12**, 344 (2013).

[123] Lide, D. R. *CRC Handbook of Chemistry and Physics (86th ed.)* CRC Press, Boca Raton (FL), (2005).

[124] Kato H. and Copeland M. I. *Report of Investigations, U. S. Bureau of Mines* Report U-952 (1962).

[125] Adams R. P. and Beall R. A. Preparation and evaluation of fused hafnium carbide. *Report of Investigations, U. S. Bureau of Mines* Report 6304 (1963).

[126] Sara R. V. The hafnium-carbon system. *Transactions of the metallurgical society of AIME* **233**, 1638 (1965).

[127] Rudy E. *AFML-TR-65-2* Part 1 Vol IV (1965).

[128] Storms E. K. *The Refractory Carbides*, Academic, New York, (1967).

[129] Deardorff D. K., Copeland M. I. and Adams R. P. The hafnium-carbon phase diagram. *Report of Investigations, U. S. Bureau of Mines* Report 6983 (1967).

[130] Sara, R. B. and Lowell, C. E. *Wright Air Development Division of Materials and Processes, Progress Report WADD-TDR-60-143* Part V (1964).

[131] Emeleus, H. J. and Sharpe, A. G. *Advances in Inorganic Chemistry and Radiochemistry, Volume 11* (Academic, New York, 1968).

[132] Agte, V. C. and Altertum, H. Untersuchungen über systeme hochschmelzender carbide nebst beiträgen zum problem der kohlenstoffschmelzen. *Zeitschriftfür technische Physik* **11**, 182 (1930).

[133] *Encyclopedia Britannica* Encyclopedia Britannica, Chicago, (1993).

[134] Kaufman, L. and Bernstein, H. *Computer Calculation of Phase Diagrams.* Academic Press, New York, (1970).

[135] Andrievskii R. A., Strel'nikova N. S., Poltoratskii N. I., Kharkhardin E. D. and Smirnov V. S. Melting point in systems ZrC-HfC, TaC-ZrC, TaC-HfC. *Soviet Powder Metallurgy and Metal Ceramics* **6**, 65 (1967).

[136] Henkelman G., Arnaldsson A. and Jonsson H. A fast and robust algorithm for Bader decomposition of charge density. *Comp. Mater. Sci.* **36**, 354 (2006).